UNIVERSITY OF SOUTHAMPTON

FACULTY OF PHYSICAL SCIENCES AND ENGINEERING

Optoelectronics Research Centre

Mid-infrared Integrated Photonic Devices for Biosensing

By

Vinita Mittal

Thesis for the degree of Doctor of Philosophy

April 2017

UNIVERSITY OF SOUTHAMPTON

ABSTRACT

FACULTY OF PHYSICAL SCIENCES AND ENGINEERING

Doctor of Philosophy

Thesis for the degree of Doctor of Philosophy

Mid-infrared Integrated Photonic Devices for Biosensing

By Vinita Mittal

This thesis describes the realisation of devices and techniques based on evanescent field sensing using planar optical waveguides for mid-infrared (MIR) absorption spectroscopy, to provide bio-chemical sensing capabilities for medical diagnostics. The fundamental vibrations of bio-chemical molecules occur in the MIR region, where their absorption is orders of magnitude stronger than their overtone bands in the near-infrared making it suitable for highly sensitive and specific absorption spectroscopy. Realisation of waveguides is an essential step towards mass-producible and low-cost integrated lab-on-chip devices. Two chalcogenide compositions were used to make waveguides, germanium telluride ($GeTe_4$) as waveguide core and zinc selenide (ZnSe) as waveguide lower cladding. Two approaches were followed for waveguide fabrication: $GeTe_4$ waveguides on bulk ZnSe and $GeTe_4$ waveguides on thin films ZnSe deposited on Si. High contrast ($\Delta n \sim 0.9$) $GeTe_4$ channel waveguides on ZnSe were fabricated using photolithography and lift-off. Waveguiding was demonstrated for the wavelength range between 2.5 and 9.5 μm for $GeTe_4$ channel waveguides on bulk ZnSe substrates. $GeTe_4$ waveguides fabricated on Si with ZnSe isolation layers were characterised for waveguiding and propagation losses in the wavelength range between 2.5 and 3.7 μm. ZnSe rib waveguides were also fabricated on oxidised Si by photolithography and dry etching and were characterised for propagation losses in the wavelength region of 2.5-3.7 μm. Absorption spectroscopy of liquid mixtures absorbing in the MIR was performed on the surface of the waveguide and the results were compared with a theoretical model.

List of Publications

Journals

- '*Optical quality ZnSe films and low loss waveguides on Si substrates for mid-infrared applications',* V. Mittal, N. P. Sessions, J. S. Wilkinson, and G. S.Murugan, Opt. Mater. Express Vol. 7, pp.712-725 (2017)
- '*Germanium Mid-Infrared Photonic Devices',* G. Z. Mashanovich, C. J. Mitchell, A. Z. Khokhar, C. G. Littlejohns, J. S. Penades, W. Cao, Z. Qu, S. Stankovic, F. Y. Gardes, L. Shen, N. Healy, T. B. Masaud, H. M. H. Chong, V. Mittal, G. S.Murugan, J. S. Wilkinson, A. C. Peacock, and M. Nedeljkovic, J. Lightw. Technol. Vol. 35(4), pp.624-630 (2017)
- *'Fabrication and characterization of high-contrast mid-infrared $GeTe_4$ channel waveguides',* V. Mittal, A. Aghajani, L. G. Carpenter, J. C. Gates, J. Butement, P. G. Smith, J. S. Wilkinson and G. S. Murugan, Opt. Lett. Vol.40(9) pp.2016-2019 (2015)

International Conferences

- '*Chalcogenide waveguides for mid-infrared applications*', V.Mittal, J.S.Wilkinson, G.S.Murugan, EMN Meeting on Photonics, Barcelona, Spain 19-23 Sep 2016 (Invited)
- '*Mid IR Applications of Si Photonics*', G. Z. Mashanovich, J. Soler Penades, V. Mittal, G. S. Murugan, A. Z. Khokhar, C. J. Littlejohns, S. Stankovic, A. Ortega-Monux, G. Wanguemert-Perez2, R. Halir, I. Molina-Fernandez, C. Alonso- Ramos, D. Benedikovic, A. Villafranca, P. Cheben, J. J. Ackert, A. P. Knights, J. S. Wilkinson, M. Nedeljkovic, OECC/PS Niigata, Japan 3-7 Jul 2016 (Invited)
- '*Chalcogenide waveguides on silicon for mid-infrared sensing applications*', G.S.Murugan, V.Mittal, J.S.Wilkinson, 7th International Conference on Optical, Optoelectronic and Photonic Materials and Applications , Montreal, Canada 13-17 Jun 2016 (Invited)
- '*Optical quality ZnSe films on Si for mid-IR waveguides*', V. Mittal, J. S. Wilkinson and G. S. Murugan, CLEO, San Jose, California, USA 5-10 Jun 2016
- '*Mid-infrared chalcogenide waveguides on silicon'*, G.S.Murugan, V.Mittal, J.S.Wilkinson, Energy Materials and Nanotechnology Quantum Meeting Phuket 8-11 Apr 2016 (Invited)
- '*High contrast mid-infrared chalcogenide waveguides for biosensing applications'* , V. Mittal, J. S. Wilkinson, G. S. Murugan , Glass Reflections Cambridge 7-9 Sep 2015
- '*Mid infrared $GeTe_4$ waveguides on silicon with a ZnSe isolation layer*', V. Mittal, C. Craig, N. P. Sessions, D. W. Hewak, J. S. Wilkinson and G. S. Murugan, SPIE Optics + Photonics '15 San Diego, California 9-13 Aug 2015
- *'Chalcogenide waveguides for mid-infrared biomedical sensing applications',* G. S. Murugan, V. Mittal, C. Craig, D. Hewak, and J. S. Wilkinson, Photonics North '15 Ottawa, Canada 9-11 Jun 2015 (Invited)
- *'$GeTe_4$ channel waveguides for the mid-wave infrared spectral band',* V. Mittal, L. G. Carpenter, J. C. Gates, J. S. Wilkinson and G. S. Murugan, International Conference on Fibre Optics and Photonics Kharagpur, India 13-16 Dec 2014 T4B.4
- *'High contrast $GeTe_4$ waveguides for mid-infrared biomedical sensing applications'*, V. Mittal, J. S. Wilkinson and G. S. Murugan, SPIE Photonics West Conference, San Francisco, California, USA 1-6 Feb 2014

Contents

List of Figures ... x

List of Tables ... xvii

Declaration of Authorship ... xix

Acknowledgements ... xx

Nomenclature ... xxii

CHAPTER 1 Introduction ... 1

1.1 Motivation ... 1

1.2 MIR materials and waveguides ... 7

Halides: ... 7

Group IV materials: ... 8

III-V semiconductors: ... 9

Chalcogenides: ... 10

Materials used for this work: ... 12

Loss mechanisms in infrared materials [164] ... 16

1.3 MIR absorption spectroscopy ... 17

1.4 MIR Evanescent sensing ... 18

1.5 MIR absorption biosensing ... 21

1.6 Main directions of the project ... 23

1.7 Structure of the thesis ... 24

CHAPTER 2 Theory and modelling of waveguides for sensitive surface absorption spectroscopy 27

2.1 Planar slab waveguides ... 28

2.1.1 The ray model for a slab waveguide 28

2.1.2 The wave model for a slab waveguide 31

2.2 Simulation and design of 2D waveguides 35

2.2.1 Channel and rib waveguides 36

2.2.2 Bends 39

2.3 Calculation of isolation layer thickness for chalcogenide waveguides on Si 41

2.4 Waveguide sensitivity model 47

Bulk analyte: 49

2.4.1 Waveguide design optimisation for an arbitrary small $\Delta k = 10^{-6}$ in the cover region 53

2.4.2 Waveguide design optimisation for k_{IPA} in the cover region 55

2.5 Conclusion 58

CHAPTER 3 MIR Waveguide Fabrication and Characterisation Procedures 59

3.1 Tools used for deposition of thin films 60

3.1.1 RF Sputtering 60

3.1.2 Thermal evaporation 62

3.2 Tools used for film characterisation 63

3.2.1 Film Thickness 63

3.2.2 Surface morphology by microscope and SEM 64

3.2.3 Crystallinity by XRD 64

3.2.4 Surface roughness by AFM 65

3.2.5 Composition by EDX and XPS 65

3.2.6 Optical transmission by FTIR 67

3.2.7 Optical constants by IR-VASE Ellipsometry and Prism coupler 67

3.2.8 Surface wettability by contact angle measurement 68

3.3 2D waveguide fabrication procedures and tools used 68

3.3.1 Photolithography and dry etching 70

3.3.2 Photolithography and Lift-off 71

3.4 Waveguide end-facet preparation 74

3.5 Waveguide characterization in the MIR 74

3.5.1 MWIR experimental apparatus 75

3.5.2 LWIR experimental apparatus: 77

3.6 Conclusion 79

CHAPTER 4 $GeTe_4$ thin films and waveguides on ZnSe 81

4.1 Deposition of $GeTe_4$ films 81

4.2 Characterisation of $GeTe_4$ films 83

4.2.1 Crystallinity, surface morphology and roughness 83

4.2.2 Optical transmission 85

4.2.3 Optical constants 88

4.2.4 Composition: 89

4.3 $GeTe_4$ waveguide fabrication 91

4.4 $GeTe_4$ waveguide characterisation in the MIR 93

4.5 Conclusions 98

CHAPTER 5 ZnSe thin films and waveguides on Si 101

5.1 Deposition by RF sputtering and thermal evaporation 102

5.2 Characterisation of ZnSe films.. 105

5.2.1 Crystallinity 105

5.2.2 Contact angle.. 107

5.2.3 Structure, morphology and roughness 108

5.2.4 Composition 109

5.2.5 Optical Transmission 113

5.2.6 Optical constants.. 114

5.3 Fabrication and characterisation of ZnSe waveguides.. 115

5.4 Conclusion 117

CHAPTER 6 $GeTe_4$ waveguides on Si.. 118

6.1 Fabrication of $GeTe_4$/ZnSe/Si waveguides 118

6.1.1 Design of curved structures 120

6.2 Characterisation of $GeTe_4$/ZnSe/Si waveguides... 121

6.2.1 Straight waveguides.. 122

6.2.2 Splitter 123

6.2.3 L-shaped 90 ° bent waveguides 124

6.3 Conclusion 125

CHAPTER 7 MIR waveguide spectroscopy... 127

7.1 Spectroscopy in MWIR with water and IPA.. 128

7.2 Comparison of experimental and theoretical transmission.................................. 132

7.3 Conclusion 135

CHAPTER 8 Conclusions and future directions 137
8.1 Overview 137
8.2 Conclusions 138
8.2.1 $GeTe_4$ films and waveguides on bulk ZnSe substrates 138
8.2.2 ZnSe films and waveguides on oxidised Si 139
8.2.3 $GeTe_4$ waveguides on Si with ZnSe isolation layer 139
8.2.4 Waveguide sensitivity model 140
8.2.5 Waveguide spectroscopy of IPA and water 140
8.3 Future directions 140
8.3.1 Materials 140
8.3.2 Investigation of $GeTe_4$ target and fabricated films 141
8.3.3 Capping layer 142
8.3.4 ZnSe waveguides in LWIR 142
8.3.5 Gratings 142
8.3.6 Reliable spectroscopic measurements 143
8.3.7 Integration of waveguides with microfluidics 143
8.3.8 Spectroscopy of clinically relevant species 143
Appendix A 145
Dry etching of $GeTe_4$ 145
Appendix B 149
Waveguide higher mode stripping 149
List of references and weblinks 155

List of Figures

Fig. 1.1 Electromagnetic spectrum showing the wavelength and frequency range of each region 4

Fig. 1.2 Schematic of a mid-infrared lab-on-a-chip sensor system 5

Fig. 1.3 (a) Energy diagram showing inter band transition and (b) Multistage cascaded geometry of a QCL 6

Fig. 1.4 Evanescent field based sensing of biomolecules in the mid-infrared region: light is coupled into the single mode waveguide and the transmission spectrum of the guided light is detected in the waveguide, with a biological analyte on its surface 19

Fig. 1.5 Wave-model describing single mode guidance 21

Fig. 2.1 (a) Side view of a slab waveguide showing ray and wavefront picture (b) TE and (c) TM polarisations (adapted from [130]) 29

Fig. 2.2 Modal field distribution of an asymmetric slab waveguide (adapted from [135]). 35

Fig. 2.3 Mode field distribution of the electric field components for (a) TE and (b) TM polarisations at λ = 7.5 μm for a channel waveguide 38

Fig. 2.4 neff of channel and rib $GeTe_4$ waveguides on ZnSe substrate simulated using Comsol 38

Fig. 2.5 Schematic of the (a) channel and (b) rib $GeTe_4$ waveguides on ZnSe substrate showing effective indices of the vertical and lateral regions 40

Fig. 2.6 Bend losses calculated for (a) channel and (b) rib $GeTe_4$ waveguides at bend angles of 30°, 60° and 90° 41

Fig. 2.7 Schematic of fabrication of chalcogenide waveguide on silicon 42

Fig. 2.8 Optical constants of (a) Si and (b) Silica 43

Fig. 2.9 Dispersion profile of $GeTe_4$ and ZnSe and effective indices of $GeTe_4$ waveguide on ZnSe substrate in both the polarisations waveguide on ZnSe substrate.............................. 44

Fig. 2.10 (a) and (b) Schematic of the $GeTe_4$ waveguide with ZnSe isolation layer on Si and oxidised Si respectively, (c) Thickness of ZnSe isolation layer needed to achieve a loss of less than 0.1 dB/cm for both Si and oxidised Si substrates.. 45

Fig. 2.11 (a) Schematic of the ZnSe waveguide with SiO_2 isolation layer on Si and (b) Propagation losses and n_{eff} of ZnSe waveguide with different SiO_2 thickness on Si........... 46

Fig. 2.12 Propagation losses in ZnSe waveguides for ZnSe core thickness of 1 and 2 µm vs. wavelength, when SiO_2 thickness was fixed as 2.5 µm 47

Fig. 2.13 (a) Optical constants of water, (b) IPA and (c) comparison of k for water and IPA (the red circles indicate points on water spectrum showing the corresponding wavelengths at which the calculations are carried out and the arrows indicate the IPA absorption) 50

Fig. Fig. 2.14 (a) Schematic of the waveguide simulated for the sensitivity model and (b) ratio of modal power in the cover of the waveguide to the total power in the waveguide for TE and TM polarisations at different wavelengths in the MIR and (c) Electric field profile of the waveguide at λ = 3.36µm for both TE and TM polarisations in vertical direction. 52

Fig. 2.15 Optimised $GeTe_4$ thickness for maximum sensitivity vs. wavelength 53

Fig. 2.16 The sensitivity of the waveguide to a small change in absorption in the waveguide cover region, plotted against the length of the waveguide 54

Fig. 2.17 k_m calculated for mixture of water and IPA... 56

Fig. 3.1 Schematic of the OIPT RF sputtering system 61

Fig. 3.2 Schematic of the AJA RF sputtering system 62

Fig. 3.3 (a) Schematic of a thermal evaporator system, (b) a photograph of the chamber while depositing ZnSe films and (c) a Ta boat used for evaporation ………………………63

Fig.3.4 Schematic of principle of photoelectron emission in an XPS………………………..66

Fig. 3.5 Schematic of the standard photolithography and dry etching process steps …….70

Fig. 3.6 Schematic of the Lift-off process using photolithography and LOR photoresist ..72

Fig. 3.7 Schematic of the Lift-off process using photolithography and AZ2070 photoresist ………………………………………………………………………………………………...74

Fig. 3.8 Schematic of the experimental set-up used for characterisation of waveguides in the MIR ………………………………………………………………………………………75

Fig. 3.9 Output power recorded from the OPO laser operating at wavelengths between 2.5 μm and 3.7 μm ……………………………………………………………………………...76

Fig. 3.10 TE cooled MCT detector's responsivity and detectivity spectrum [from manufacturer's test data] ………………………………………………………………….77

Fig. 3.11 Output power spectrum of QCL operating at wavelengths between 6 μm and 12 μm ……………………………………………………………………………………78

Fig. 4.1 Deposition rate of $GeTe_4$ films as a function of sputtering pressure and sputtering power. (*indicates the plasma did not strike at that pressure) 82

Fig. 4.2 (a) XRD pattern of (i) a polycrystalline ZnSe substrate, (ii), (iii) a $GeTe_4$ film deposited at a temperature 20°C and 250°C, respectively, and (iv) $GeTe_4$ target, SEM images of (b) top surface and (c) the cleaved cross-section of an as-deposited $GeTe_4$ film on ZnSe substrate 83

Fig. 4.3 AFM image of 1x1 μm2 scan area of (a) ZnSe substrate and $GeTe_4$ film deposited at temperature (b) 20°C and (c) 250°C respectively 84

Fig. 4.4 FTIR spectra of 1.76 μm and 7.0 μm thick $GeTe_4$ film, and 2 mm thick ZnSe substrate 85

Fig. 4.5 Schematic of an absorbing film on a transparent substrate 86

Fig. 4.6 Experimental and theoretical transmission of ~7.0 μm $GeTe_4$ film deposited on ZnSe substrate 87

Fig. 4.7 Ellipsometry graphs showing the optical constants n and k for (a) the $GeTe_4$ film and (b) ZnSe substrate 88

Fig. 4.8 $GeTe_4$ material loss in dB/cm calculated using extinction coefficient, k, from ellipsometry data. Inset: A small region is zoomed in around 10 μm wavelength, where losses start to appear 89

Fig. 4.9 Depth profile of $GeTe_4$ film by XPS showing composition of the film (a) after every minute etching until the substrate was reached (b) shows the initial 3 minutes with every 1 minute etching data and (c) shows the initial 120 sec etched every 20 sec 91

Fig. 4.10 (a) Undercut created by LOR and photoresist and (b) Cleaved cross-section of $GeTe_4$ channels on bulk ZnSe substrate after stripping off the LOR and photoresist (inset: top view of the channels) 92

Fig. 4.11(a) A microscope image of the polished $GeTe_4$ channel waveguides on ZnSe substrates, (b) an SEM image of $GeTe_4$ channel waveguides cut by ductile dicing, (c) a schematic of the end facet of the waveguides cut by ductile dicing and (d) an SEM image showing the cross-section of the diced end facet of the waveguides 93

Fig. 4.12 Experimental apparatus for optical characterisation of the waveguides.............. 94

Fig. 4.13 Infra-red camera images (taken with the inbuilt camera lens) of the output facet of the guiding channel waveguide seen from (a) top and (b) cross-section view (inset: magnified image of the guiding channel) 94

Fig. 4.14(a) Magnified background corrected infrared image of the mode at 3.5μm wavelength, (b) measured horizontal and vertical fundamental mode profiles with theoretical comparison and (c) Infrared image showing streak of light in the guiding channel at λ=3.5μm 96

Fig. 4.15(a) Top view and (b) cross-section of the infra-red camera image of the output facet of the guiding channel waveguide at 6.8 μm wavelength (c) magnified image of the guiding channel 97

Fig. 4.16 Infrared image showing waveguiding at 8.5μm wavelength (inset: magnified image of the guiding channel) 97

Fig. 5.1 Calibration of source current applied to Ta boat with temperature 103

Fig. 5.2 Photographic images of bulk ZnSe substrate and ZnSe films deposited on glass substrates 104

Fig. 5.3 XRD patterns of (a) sputtered, (c) evaporated and (d) bulk ZnSe along with the ICDD crystal plane data for (b) hexagonal and (e) cubic ZnSe 106

Fig. 5.4 Water contact angle for sputtered, evaporated and bulk ZnSe 107

Fig. 5.5 FESEM images of (a), (b) surface and (c) cross-section of sputtered ZnSe film on Si and (d), (e) surface and (f) cross-section of the annealed evaporated film on Si 108

Fig. 5.6(a) and (b) FESEM images of sputtered ZnSe films after annealing 109

Fig. 5.7AFM images of a 2x2 μm2 scan area of (a) sputtered and (b) evaporated ZnSe on Si 109

Fig. 5.8 XPS Spectra of sputtered and evaporated ZnSe films showing fitted peaks for the elements Zn, Se and O 111

Fig. 5.9 Infrared transmission spectra of bulk ZnSe substrate, Ge substrate, sputtered and evaporated ZnSe films on Ge substrates 113

Fig. 5.10 FESEM image of cross-section of ZnSe rib waveguide on oxidised Si, (b) and (c) IR image of the guided spot emerging from the waveguide for sputtered and evaporated ZnSe waveguides, (d) and (e) IR images of the scattered light measured along the propagation length for waveguide with sputtered and evaporated ZnSe respectively at λ = 3.7 μm and (f) propagation losses in sputtered and evaporated ZnSe waveguides for 2.5 μm < λ < 3.7 μm respectively 116

Fig. 6.1 SEM images of (a) undercut profile created by photoresist on developing, (b) $GeTe_4$ film deposited on the pattered sample, (c) and (d) top and cross-section of $GeTe_4$ channel after lifting off the photoresist 119

Fig. 6.2 A portion of the designed mask from L-Edit software showing the curved structures 120

Fig. 6.3 Microscope images of (a) L-shaped bent structures, (b) a section of a splitter, (c) four output arms of a splitter with gratings at the output ends and (d) magnified image of gratings after lifting-off the photoresist 121

Fig. 6.4 Experimental apparatus used for waveguide characterisation in the MIR region 122

Fig. 6.5 Top view of the infrared images of the output facet of a channel waveguide and scattered light measured along the propagation length of the guided mode with (a), (b) Sputtered and (c), (d) Evaporated ZnSe isolation layer on Si, at a wavelength of 3.7 μm, and (e) Propagation loss of $GeTe_4$ waveguide for sputtered and evaporated ZnSe isolation layer 122

Fig. 6.6 IR image of the guiding splitter arms at λ = 3.7 μm, with the numbers marked according to ascending order of their lengths with 1 being the shortest 124

Fig. 6.7(a) Graph and (b) table showing propagation loss calculated for $GeTe_4$ channel waveguide using cut-back method 125

Fig. 7.1 Molecular structure of (a) Water and (b) IPA 128

Fig. 7.2 An SEM image of the cleaved cross-section of a ZnSe rib waveguide on oxidised Si 129

Fig. 7.3 Experimental setup for MIR waveguide spectroscopy 130

Fig. 7.4(a) Illustration of the waveguide assembly used for aqueous analyte measurement and (b) Transmission spectra of water on the surface of the waveguide with and without filter paper (FP) 131

Fig. 7.5 Experimental and theoretical MIR spectra of 100% water and 100% IPA on the surface of a ZnSe waveguide 132

Fig. 7.6MIR transmission spectra of six different concentrations of water and IPA measured on the surface of a ZnSe waveguide (* the data for 100% IPA is processed differently than other concentrations due to the nature of experiment) 133

Fig. 7.7 Comparison between theory and experiment for the transmission of ZnSe rib waveguide at a wavelength of 3.36 μm vs. concentration of IPA in water 134

Fig. A.1 (a) CHF_3 and O_2 etched and (b) SF_6 and O_2 etched $GeTe_4$ waveguides showing the rough etched surfaces 146

Fig. A.2 ICP etched $GeTe_4$ ribs with (a) Ar/HBr at 100W RF power, (b) and (c) Ar/CHF_3/SF_6 at 100W and 25W RF power respectively 147

Fig. A.3 (a) An ICP etched and (b) an Ar ion-beam etched $GeTe_4$ rib waveguide 148

Fig. A.4 ICP etched $GeTe_4$ gratings on Si substrate 148

Fig. B.1 propagation loss due to Si, in $GeTe_4$ single mode (SM) and multimode (MM) waveguides vs. the thickness of ZnSe isolation layer 150

List of Tables

Table 1.1 MIR transparent materials 14

Table 0.2 Properties of ZnSe and $GeTe_4$ 15

Table 1.3 Comparison of various MIR waveguide/analyte systems for sensing 22

Table 2.1 $GeTe_4$ channel and rib waveguide dimensions at λ = 7.5 μm for single mode operation........ 37

Table 2.2 Optimised lengths (L_{opt}) and sensitivity (S) for a small absorption change of 10^{-6} in the cover of the $GeTe_4$ waveguide at different wavelengths........ 55

Table 2.3 Change in transmittance of IPA in water at various wavelengths........ 56

Table 5.1 Composition analysis using XPS depth profiling of sputtered and evaporated ZnSe films........ 112

Table 5.2 Prism coupling measurements for ZnSe films in TE polarisation at 1550 nm... 115

Table 7.1 IR vibrational bands of water and IPA in the MIR region........ 128

Table A.1 ICP etch recipes for $GeTe_4$ films........ 146

Declaration of Authorship

I, Vinita Mittal declare that this thesis entitled "Mid-infrared integrated photonic devices for biosensing" and the work presented in it are my own and has been generated by me as the result of my own original research.

I confirm that:

1. This work was done wholly or mainly while in candidature for a research degree at this University;
2. Where any part of this thesis has previously been submitted for a degree or any other qualification at this University or any other institution, this has been clearly stated;
3. Where I have consulted the published work of others, this is always clearly attributed;
4. Where I have quoted from the work of others, the source is always given. With the exception of such quotations, this thesis is entirely my own work;
5. I have acknowledged all main sources of help;
6. Where the thesis is based on work done by myself jointly with others, I have made clear exactly what was done by others and what I have contributed myself;
7. Either none of this work has been published before submission, parts of this work have been published as [please see List of Publications]:

Signed: ....

Date: ....

Acknowledgements

Foremost, I would like to express my sincere gratitude to my supervisor James Wilkinson for the immeasurable amount of guidance he provided throughout the course of this thesis. Being my research guide, he always welcomed to listen to my ideas, provided insightful discussions and stimulus for critical thinking, reviewed my work and provided valuable feedback and encouragement to the efforts.

I would like to extend my sincere gratitude towards my co-supervisor Senthil Ganapathy. His contribution to this research is the foremost. I appreciate all his contributions, from day first he has provided constant help and support and helped me learn experimental techniques. I am grateful to him for providing an opportunity to expand my knowledge and skills while carrying out this research.

My research group members and friends have contributed immensely to my professional and personal time at Southampton. I would like to thank Jon Butement, Armen Aghajani, Dave Rowe, Amy Tong, Shahab Bakhtiari, Zilong Wang, Ping Hua, Alina Karabchevsky, Mohd. Narizee, Colin Mitchell, Neil Sessions, Nick Klokkou, for their support in the present work.

Many thanks to Dan Hewak for sharing his immense knowledge and experience on chalcogenide materials with me from time to time. I want to thank Neil Sessions, Mike Perry, Owain Clark, Chris Craig and Corin Gawith for providing training and advice in carrying out the cleanroom work, and Mark Light for providing training in X-ray diffraction. I am grateful to James Gates for providing training in prism coupling measurements and making it a fun learning experience. My sincere thanks to Lewis Carpenter for dicing the waveguide samples. I am grateful to Milos Nedeljkovic for

spending time and providing useful advice on designing the mask and discussing MIR concepts. My sincere thanks to Dave Rowe for discussing concepts on microfluidics and biosensing and helping in carrying out the sensing experiments. Thanks to Jordi Penades for helping me with the design of gratings.

Special thanks to my friends, Jonny, Armen, Magda, Graham, Amy, Dave, Reza, Khouler, Naresh and Saurabh for making PhD years wonderful and enjoyable.

I would like to thank the European Research Council for funding this research under the EU 7th Framework Programme (FP7/2007-2013) / ERC grant agreement no. 291216.

Above all, I would like to thank my family for their constant support and encouragement. I would like to specially thank my brother Nitesh Mittal, for his endless and selfless help throughout my PhD journey.

Nomenclature

AFM	Atomic force microscopy
ATR	Attenuated total reflection
CMOS	Complementary metal oxide silicon
CVD	Chemical vapour deposition
DI	De-ionised
EM	Electromagnetic
FEWS	Fiber evanescent wave spectrsocopy
FESEM	Field effect scanning electron microscope
FWHM	Full width half maxima
FTIR	Fourier transform infrared
GIXRD	Grazing incidence X-ray diffraction
GOS	Germanium on Si
ICP	Inductively coupled plasma
IPA	Isopropanaol
LOD	Limit of detection
LOR	Lift off resist
LWIR	Long wavelength infrared
MIR	Mid infrared
MM	Multimode
MMI	Multimode interferometer
MCT	Mercury cadmium telluride
MMI	Multimode interference (device)
MOVPE	Metal oxide vapour phase epitaxy
MWIR	Mid-wave infrared
MZI	Mach-Zehnder interferometer
NA	Numerical aperture
NIR	Near infrared

OPO	Optical parametric oscillator
QCL	Quantum cascade laser
RF	Radio frequency
RI	Refractive index
RIE	Reactive ion etching
RTA	Rapid thermal annealing
SM	Single mode
SOI	Silicon on insulator
SOS	Silicon on sapphire
S/N	Signal/Noise
TE	Transverse electric
TIR	Total internal reflection
TM	Transverse magnetic
UV	Ultra-violet
XPS	X-ray photoelectron spectrsoscopy

CHAPTER 1
Introduction

1.1 Motivation

There are multitudes of biosensors available around the world and are being used as point of care diagnostic tools, but apart from few well known examples (the glucose sensor, home pregnancy test, waste water quality control sensor, personal calorie management sensor), they are often bulky, expensive, time consuming and require an expert operator. These techniques are out of reach to many people living in remote areas or are too slow for critically ill patients who need urgent care. The standard process flow for disease diagnostics includes collection of biological samples (blood, urine, tissue swabs etc.) from the point of care and transported to the centralised laboratories for sample preparation and tests by experts. After the results become available (usually few days), the laboratory notifies the clinicians or patients and the treatment is modified accordingly. This creates a delay in evidence based treatment. It is imperative that maximum number of people can have access to early warning diagnostics and hence there is a need for mass-producible and handheld prolific biosensors which can provide accurate and reliable information rapidly and at low cost. A biosensor is characterised by many features such as its selectivity, sensitivity, precision, signal stability, noise (working range of a biosensor), regeneration time and lifetime, affordability, compactness and portability. Depending on the clinically significant biochemical analyte, there are a variety of direct and indirect laboratory based tests available. Based on a specific application area, a technique or a combination of techniques can be selected or engineered that offers the customised characteristics of a biosensor. There are a number of widely used *in vitro* diagnostics techniques such as microscopy, chromatography, culture, immunoassays, nucleic acid amplification, piezoelectric, electrochemical and optical. Each of these have

their well-recognised advantages and shortcomings. Microscopy lacks sensitivity and quantification in many clinical scenarios, conventional immunoassays are highly sensitive but are labour intensive and challenging for multiplex detection, nucleic acid amplification offers high molecular specificity but demands a complex sample preparation, piezoelectric sensors are limited by temperature, voltage and stress, electrochemical sensors being highly successful for their fast response time and sensitivity but often require highly stable and accurate reference electrode and some enzyme based transducers require extraction, isolation and purification of biomolecules from the unwanted background constituents or contaminants to increase selectivity. These purification techniques are not only time consuming and expensive but also sometimes leads to loss of bio-chemical activities in the process [1, 2]. Optical biosensors offer rapid, low-cost analysis and detection tools with the versatility for integration of highly multidisciplinary approaches such as microelectronics, biology, biotechnology and chemistry. Optical approaches are widely used for chemical analysis in microsystems as they have an excellent track-record in chemical analysis, usually show the lowest limits of detection (LOD) and provide the greatest chemical or morphological information of the analyte. There are a number of advantages in using optical measurements such as 1) it is a non-destructive technique, 2) more information can be collected with the same sample, 3) high sensitivity (ppb-ppm) and performance. The two most common detection protocols used in optical biosensing are fluorescence based detection and label-free detection. In fluorescence based detection the target molecules are labelled with fluorescence tags, and the intensity of fluorescence indicates the presence of target molecules. While this technique is extremely sensitive, it requires laborious labelling process and its quantitative analysis is challenging. Label free detection on the other hand is direct and relatively easy to perform. Label-free optical detection includes refractive index (RI), absorption and Raman spectroscopic detection. RI and absorption are real and imaginary parts of complex RI constant. Raman detection involves unlabelled target molecules like RI and absorption detection, while the emitted Raman light is used for detection similar to fluorescence based detection [3]. Devices based on real part of refractive indices lack specificity because lots of different things can change refractive index. Both Raman and absorption infrared spectroscopies involves molecular vibrational transitions based on scattering or absorption of molecules respectively. This work is

focussed on fabrication of waveguide devices based on optical absorption detection of aqueous analytes in the mid-infrared (MIR) region. The MIR region is extremely suitable for absorption spectroscopy because the fundamental vibrations of biochemical molecules occur in this region, where their absorption is orders of magnitude stronger than their overtone bands in the near-infrared (NIR) making it useful for highly sensitive absorption spectroscopy. A molecule can vibrate in many ways (symmetric and anti-symmetric stretching, rocking, wagging, bending, twisting, scissoring) depending on the number of atoms and its linearity. Each of these vibrations corresponds to a vibrational mode. A diatomic molecule has one bond corresponding to one vibrational mode. The symmetry of the molecule and a set of selection rules define the allowed and forbidden vibrational transitions. For example, water (H_2O) is a non-linear molecule and has three vibrational modes and all of these are allowed transitions or IR-active.

MIR is a part of the infrared region that has a wavelength range from 2.5-20 μm that corresponds to wavenumber range 4000-500 cm^{-1} and frequency range 120-15 THz as shown in Fig. 1.1. It is broadly categorized into four regions according the type of vibrations, X-H stretching region (4000-2500 cm^{-1} or 2.5–4 μm) where X is any atom, the triple bond region (2500–2000 cm^{-1} or 4–5 μm), the double bond region (2000 -1500 cm^{-1} or 5–6.66 μm) and the fingerprint region due to bending vibrations (1500-600 cm^{-1} or 6.66–16.66 μm) [4]. In this work it is divided into two wavelength bands according to the measurement setups used in this work: the mid wavelength infrared region (MWIR) corresponding to 2.5–4 μm wavelength region and the long wavelength infrared region (LWIR) corresponds to 6–12 μm wavelength region.

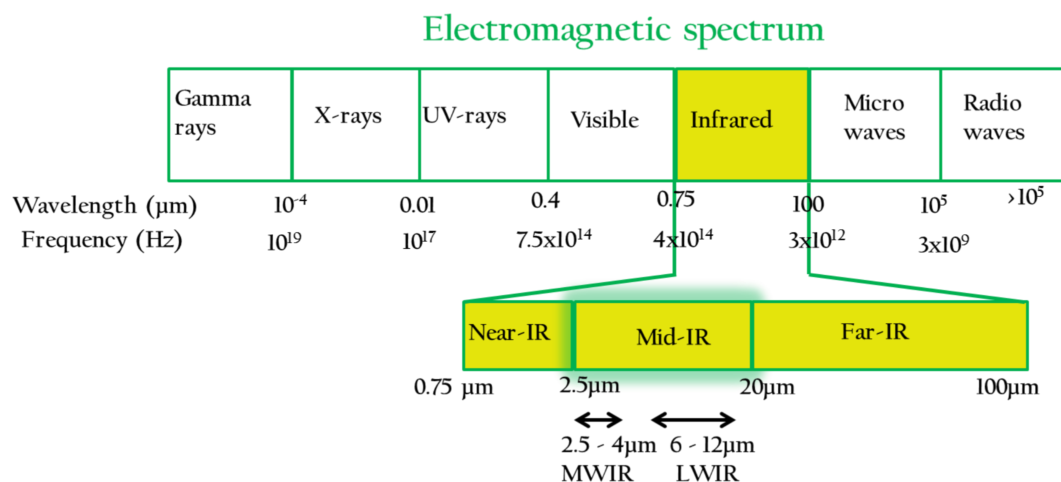

Fig. 1.1 Electromagnetic spectrum showing the wavelength and frequency range of each region

MIR is an important region for a broad range of applications in various fields such as spectroscopy, pharmaceuticals, forensic, security and safeguard, astronomy, climate and pollution monitoring, sensing and detection of some prominent gases such as CO_2, O_2, CO, NO, CH_4, HCl; liquids such as oil, biological tissues and solids such as plastics, food etc [5]. These applications are not only technologically significant but also contribute to a safe and secure society. The main driving force behind this work is MIR aqueous biosensing. MIR technologies are promising for identification and detection of analytes of very low concentration using their fingerprint absorption in this region, offering high selectivity over a wide range of compounds without labelling. The presence of biological markers of disease or of molecular changes in clinical samples can be distinguished by studying their MIR spectra, leading to the rapid high sensitivity, real time measurement of complex mixtures to identify and quantify species for point of care diagnosis. However, realisation of optical biosensors by integrating a variety of active and passive optical components into a monolithic planar structure will enable improved efficiency and a compact device. Integrated optics allows different optoelectronic and microfluidic components to be fabricated on a single chip to help in realizing sensing of liquid analytes. This feasibility of monolithic integration makes the device robust and mass producible thus making it a potentially low cost device. Fig. 1.2 shows a vision of an integrated lab on a chip sensor system comprised of a MIR light source, waveguides, a detector, a microfluidic channel and an integrated Fourier transform infrared (FTIR) assembly monolithically fabricated on a single substrate. The most common detectors

used for detecting MIR signal are mercury cadmium telluride (MCT) detectors because of their broad emission spectrum covering the wavelengths region from 2 to 16 μm, better sensitivity as compared to other common detectors used in FTIR such as DLaTGS detector and better signal to noise ratio [6]. There is a great potential for integrating MCT detectors on the same chip along with the source and waveguide as MCT planar waveguides have been demonstrated on CdTe substrates [7]. Researchers have shown monolithic integration of QCL and detectors on the same chip with a peak responsivity of 3.6mA/W [8]. The responsivity of the MCT detector used in this work is between 0.02 - 0.1 A/W, depending on the wavelength (Refer section 3.5.1E). The idea of making optical waveguide transducers for MIR biosensors is the key motivation behind this work. The focus of this project is to develop optical waveguides and measurement techniques based on evanescent field MIR spectroscopy.

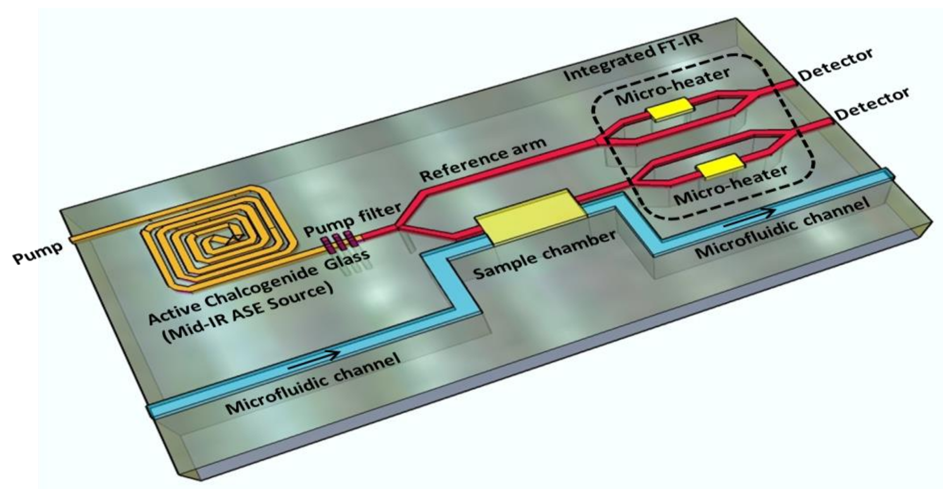

Fig. 1.2 Schematic of a mid-infrared lab-on-a-chip sensor system

In recent years active research has been taking place in developing optics in the MIR spectral regime. Many important breakthroughs have been achieved in the last few decades, and in particular the advent of the quantum cascade laser (QCLs) in 1994 [9] has revitalised MIR light sources because of their broad emission bands, high tunability, high power (in 100s of mW), user-friendly room temperature operation and compact design [10-11]. QCL is a semiconductor laser involving only one type of charge carriers (unipolarily) unlike the diode lasers which involves electron hole recombination (bipolarily). In a QCL, dozens of alternating layers of semiconductor material forms the quantum wells, which confine the electrons to a particular energy state and these

electrons tunnels through one quantum well to another, emitting photons, when a voltage is applied across the device. The emitted photons does not depend on the lasing material, rather it is determined by the structure of the layers. It requires extreme precision of material growth as the individual layers are few nanometer thick. Fig. 1.3 (a) shows the concept of unipolarity where the energy diagrams shows the inter sub-band transition with the initial and final transition states having the same curvature. Fig. 1.3 (b) shows the cascaded structure of multiple layers forming quantum wells [9].

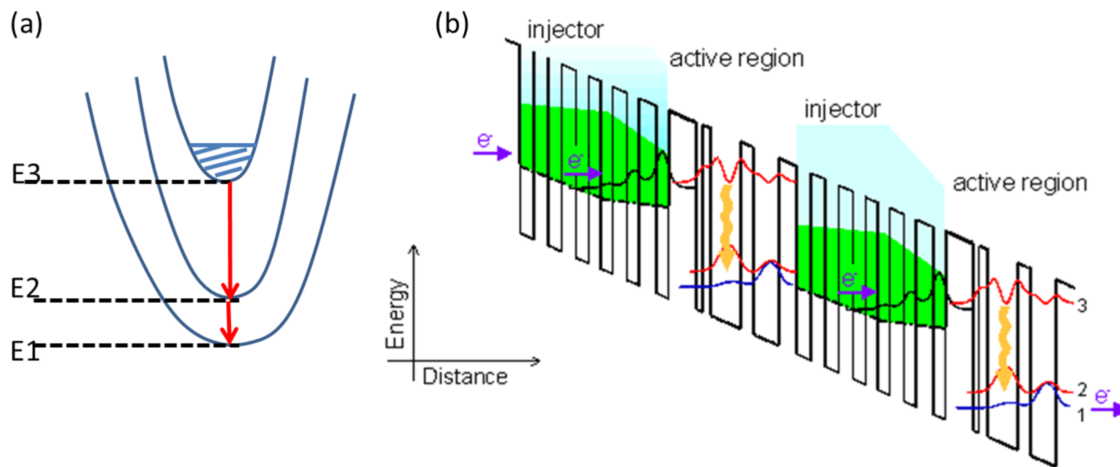

Fig. 1.3 (a) Energy diagram showing inter band transition and (b) Multistage cascaded geometry of a QCL [9].

The period from 1960-2000 witnessed the development of IR detectors from first generation linear arrays of MCT detectors to second generation large 2D arrays in square or rectangular formats. Recently, third generation IR detectors with enhanced capabilities such as better thermal resolution, higher frame rates and larger number of pixels are being developed [13]. At present, MIR technology is not fully developed to provide off the shelf MIR compatible optical components such as low loss fibers, beam splitters and high numerical aperture (NA) lenses, but there has been active research into inventing cost-effective MIR materials and optical components for specific applications. Despite these technological limitations, fabrication of devices at MIR wavelengths has the advantage that the fabrication tolerances for defects, roughness and feature dimensions are higher at the longer wavelengths.

1.2 MIR materials and waveguides

Integrated devices for MIR biosensing need waveguides for efficient and reproducible interaction of analyte with photons. Materials are the heart of any device and are so for waveguides. The two most important properties that need to be considered while selecting the MIR waveguide materials are MIR transparency and high RI. Both the waveguide core and the substrate should be MIR transparent to allow low-loss propagation of MIR light. There should be a high RI contrast between the core and the substrate which allows confinement of light into smaller geometries thereby leading to a compact device and also improves the surface optical intensity which increases the sensitivity of the device. Conventional materials like silicate or soda lime glasses transmit light up to ~ 3.7 μm wavelengths in the MIR (above λ = 3.7 μm, the transmission drops to 50% for a 6 mm bulk silica glass [14]), hence, novel materials need to be explored and engineered to cover the longer MIR wavelengths. There are several optical materials that transmit in the MIR region which include some oxides, halides, single crystalline semiconductors and chalcogenides. Only a handful of oxides are useful in the MIR region including zinc oxide (transmits up to 4 μm), magnesium oxide (transmits up to 5.5 μm) [15], tantalum pentaoxide (Ta_2O_5) (transmits up to 8 μm) [16] and yttrium oxide (Y_2O_3) (transmits up to 15μm) [17]. Ta_2O_5 and Y_2O_3 appear to be promising MIR materials but there is no literature demonstrating their MIR waveguiding capabilities. The waveguides fabricated on planar substrates from a variety of MIR transparent materials from literature are discussed below along with their propagation losses. The waveguide materials used for this thesis work belong to the chalcogenides and are also discussed in detail in this section.

Halides: Halides include chlorides, iodides and fluorides and they have excellent transmission in the MIR region (up to 25-30 μm) with RI ~ 2 depending on the concentration of halide in the compound. Silver halide planar waveguide have been demonstrated produced by a press tapering method by heating silver halide fiber segments to create waveguides with a range of thicknesses (190-300 μm) and 3 mm wide. These waveguides were used for demonstrating evanescent field sensing of urea crystals and acetic anhydride [18]. Silver halide waveguides have also been fabricated by an inter-diffusion method that yielded a waveguide loss of 4-16 dB/cm at λ=10.6 μm depending on

its thickness [19, 20]. The fabrication techniques used here are not compatible with thin film processing technology for mass production. Silver halide strip waveguides using thermal evaporation and photolithography were also reported with the propagation losses of 20 dB/cm at λ = 10.6 μm [21]. Despite having excellent MIR transparency and high refractive index, halides degrade (dissolve) in water, which makes them unstable and incompatible with detection of aqueous analytes.

Group IV materials: Single crystals such as silicon (Si) and germanium (Ge) are transparent in MIR region and have high refractive indices. Si transmits up to ~ 7-8 μm wavelengths, and has a refractive index of ~3.42 at λ = 7.5 μm. Silicon on insulator (SOI) has been used for NIR technμology platforms to demonstrate various devices in MIR regime. A library of passive SOI devices were fabricated in 3-4 μm wavelength region; such as rib waveguides with propagation losses of 0.6-1.5 dB/cm for λ = 3.39-3.77 μm, strip waveguides with losses 3-5 dB/cm at λ = 3.8 μm and slot waveguides with propagation losses of 9-10 dB/cm [22-24]. An on-chip spectrometer, low loss multimode interferometers (MMIs) (0.37 dB/MMI insertion loss at λ = 3.8 μm), Mach-Zehnder interferometers (MZIs) and ring resonators were designed and fabricated for applications at λ = 3.8 μm [25-27]. Since losses in Silica (SiO_2) start to increase beyond a wavelength of 3.7 μm (~5dB/cm at λ = 3.7 μm for bulk silica), an alternative material system, silicon on sapphire (SOS) was employed to increase the transmission range up to ~ 5.5 μm. SOS waveguides were demonstrated in the 4-5.5 μm wavelength range with propagation losses 2-4 dB/cm [28-30]. Other alternatives to increase the transmission of Si-based waveguides such as air cladded broadband on chip straight and bent waveguides and beam splitters have shown optical losses of ~ 2.7 dB/cm at λ = 3.7 μm [31]. However, novel designs are being explored to access the transmission in silica beyond 4.0 μm wavelength and to minimize water absorption dominant losses between 2.7-3.3 μm wavelength region, where losses in silica are high. For example, silica hollow core fibers were designed to obtain minimum attenuation of 34 dB/km at 3.05 μm and transmission beyond 4 μm wavelength was also achieved [32]. These designs may not be directly applicable to the integrated photonic devices used in this work; however, the idea of design and engineering of the device may be modified and transferred to integrated approach. Another CMOS compatible material, silicon nitride (Si_3N_4), which is

transparent up to 8.5 μm in MIR was used to make waveguides on oxidised silicon with the losses of 2.1 dB/cm at λ = 3.7 μm [33]. Ge, which is transparent up to ~ 15 μm and has a RI of 4 for wavelengths between 2 μm and 15 μm , is also compatible with silicon and has been used to fabricate Ge on silicon (GOS) waveguides at λ = 3.8 μm reporting record low losses of 0.58 dB/cm [34]. GOS losses at λ = 5.8 μm were reported to be 2.5-3.0 dB/cm [35, 36] and 3.0 dB/cm at λ = 7.5 μm [37]. GOS multiplexers, MZIs and thermo optic modulators were also explored. SiGe graded index waveguides were also fabricated and tested at 4.5 μm and 7.4 μm wavelengths showing losses of 1- 2 dB/cm [38]. Although GOS waveguides are promising, suitable MIR transparent substrates should be used to exploit the full MIR transparency of Ge as Si starts to absorb beyond λ = 7 μm and therefore limits GOS waveguides in MIR. Another group IV element carbon (polycrystalline freestanding diamond waveguide) was grown using CVD on Si_3N_4 coated Si and oxidised silicon substrates and were made into strip waveguides by inductively coupled plasma (ICP) etching. They were used to demonstrate detection of acetone in the wavelength range 5.78-6.35 μm using evanescent field absorption spectroscopy [39]. Waveguide transmission beyond a wavelength of 7.5 μm has not been yet demonstrated in these materials.

III-V semiconductors: Epitaxial films of gallium arsenide (GaAs) based materials are suitable for a MIR spectral window up to 13 μm and have high RI > 3. A~ 6 μm thick core layer of GaAs on a 6 μm thick buffer layer of aluminium gallium arsenide (AlGaAs) grown on Si-doped GaAs substrate by molecular beam epitaxy (MBE) and metal organic vapour phase epitaxy (MOVPE) were fabricated into ridge waveguides and on chip MZIs by reactive ion etching (RIE). Droplets of acetic anhydride were deposited on a 200 μm wide waveguide surface covering a length of 400 μm and a detection volume of 19.4 ng of acetic anhydride was demonstrated at λ = 10.2 μm. The waveguide losses were not reported [40-43]. An integrated 15-channel multiplexer on the indium phosphide (InP) platform has been demonstrated, covering 7.1-8.5 μm wavelength range with a propagation loss of 0.5-2.9 dB/cm in the wavelength range of 7.3-7.4 μm. InP is transparent up to 14 μm and has RI ~ 3 at λ = 10 μm [44]. These materials are promising for MIR applications but depositing thick layers of epitaxial films is time consuming and expensive.

Chalcogenides: Materials containing one or more of the group VI elements: sulphur, selenium or tellurium are called chalcogenides. They are considered to be the most advanced potential materials for MIR applications because of their 1) optical transparency in the visible-infrared region; up to ~8 μm for sulphur, ~14 μm for selenium and beyond 20 μm for tellurium 2) capacity of composition alloying 3) easy processability in different compositions and geometries, 4) photosensitivity, and 5) high RI for good optical confinement and enhanced optical intensities [45, 46]. These materials are generally combined with other group elements in the periodic table to form stable compounds which are used for fabrication of devices. There are various ways to deposit chalcogenide films such as RF sputtering [47-48], thermal evaporation [50-53], pulsed laser deposition [54, 55], hot embossing [56-57] and chemical deposition [49, 62], these methods can be combined with dry/wet etching or lift-off techniques to fabricate channel or rib waveguides. Within the scope of this thesis, the state-of-the-art on chalcogenide waveguides for MIR is discussed in detail according to research groups.

The first chalcogenide waveguides were reported by researchers in Japan [59, 60] and Russia [61, 62] in the 1970's where arsenic sulphide (As_2S_3) slab waveguides on lithium niobate ($LiNbO_3$) crystals were used to demonstrate diffraction of guided light by the acousto-optic effect. From then until the early 2000s, many researchers reported work on the photosensitivity, where a change in the refractive index of the waveguide core was achieved by irradiating with light at a variety of wavelengths or by in-diffusion where a material such as silver was diffused by doping by thermal diffusion to create a refractive index change [63, 64]. Losses as low as 0.3 dB/cm at λ = 1.566 μm were reported for rapid thermal annealed (RTA) films of a chalcogenide composition (GeAsSSe) on Si formed into channel waveguides by irradiating with light at 488 nm through a mask, by S. Ramachandran et al. in 1999 [65]. Direct UV (λ = 244 nm) written channel waveguides of gallium lanthanum sulphide (GaLaS) glass were reported to have losses as low as 0.2 dB/cm at λ = 1.3 μm by D. Hewak et al. in 2002 [66]. The same group also reported femtosecond laser written waveguides of GaLaS with a propagation loss of 1.47 dB/cm using optimised writing pulse parameters in 2002 [67]. Slab waveguides made by RF sputtering using chalcogenide alloys of arsenic sulphide (AsS), germanium antimonide selenide (GeSbSe) and germanium arsenic selenide (GeAsSe) were characterised at λ =

1.064 μm by Texas instruments in 1974 and propagation losses were reported to be 2–22 dB/cm depending on the composition [68]. As dry etching and lift-off became available with evolving technology, fabrication of channel and rib waveguides became popular for better confinement of light. An As_2S_3 etched waveguide was reported by B. Eggleton et al. in 2007 to have record low losses of 0.05 dB/cm at λ = 1.550 μm [69]. Chalcogenide glasses has seen enormous interest in telecommunication because of the high nonlinearities (Kerr, Raman and Brillioun), which are 2-3 orders higher than those of silica, making them stand out for optical signal processing functions such as switching [70], amplification [71, 72], lasing [73], wavelength conversion [74] and pulse compression [75]. Until recently chalcogenide waveguides were normally tested at visible or NIR wavelengths despite their capabilities in the MIR region, most likely due to limited availability of MIR sources, detectors and components.

The first experimental result in the MIR in a chalcogenide, for an As_2Se_3 channel waveguide on As_2S_3 fabricated on oxidized Si by photo darkening effect which created a local change in refractive index of As_2Se_3 was demonstrated by Ho et al. in 2006, with propagation losses of 0.5 dB/cm and 1.1 dB/cm at λ = 8.4 μm in the TE and TM polarization respectively. The RIs of As_2Se_3 and As_2S_3 are taken to be 2.78 and 2.39 at λ = 8.4 μm [76]. The results were encouraging but photo darkening leads to a small refractive index contrast (~ 0.04), which is not good for compact devices. An As_2S_3 waveguides on sodium chloride (NaCl) made by solution processing reported by C. Arnold et al. in 2010 showed propagation losses of 4.5 dB/cm at λ = 4.8 μm [77]. In the same year, the same group then published results on As_2S_3 waveguides fabricated on a $LiNbO_3$ substrate by RF sputtering and dry etching, demonstrating single-mode operation and propagation losses of 0.33 dB/cm at λ = 4.8 μm [78]. Another arsenic based composition, GeAsSe rib waveguides were fabricated by thermal evaporation and dry etching by B. L. Davies et al. in 2013, showing losses below 1 dB/cm at wavelengths between 2.5-6.6 μm when the waveguides were protected from environmental degradation by coating with a 10 nm thick fluoropolymer film [79]. The group of A. Pradel has also worked on an arsenic based composition, TeAsSe, where rib waveguides were fabricated by thermal evaporation and dry etching on As_2S_3 substrates, and propagation losses of 10 dB/cm at λ = 10.6 μm were reported [80]. Arsenic based waveguides have potential for MIR low loss waveguides;

however, arsenic is a hazardous material to deal with while processing and fabrication of the samples.

The first chalcogenide waveguide monolithically integrated with a microfluidic device was formed from germanium-antimony-sulphide (Ge-Sb-S) alloy by J. Hu et al. in 2007 [53]. Here $Ge_{23}Sb_7S_{70}$ films were deposited onto oxide coated silicon wafers using thermal evaporation and channel waveguides were defined using lift method and losses between 0.5-2.5 dB/cm were reported depending on the rib or channel width at λ = 1.55 µm. Recently in 2014, the same group published a review of their work in MIR materials and devices including Si_3N_4 directional couplers between λ = 2.45-2.65 µm, $Ge_{23}Sb_7S_{70}$-As_2Se_3-$Ge_{23}Sb_7S_{70}$ as substrate-core-uppercladding microdisk resonators fabricated on Si wafer and waveguide photonic crystal cavity fabricated on $Ge_{23}Sb_7S_{70}$-CaF_2 as core/substrate combination by focused ion beam milling working at a wavelength of 5.2 µm for MIR sensing applications. To enhance the specificity of the sensor, its surface functionalization was studied, and monolithic PbTe detectors on Si were designed and fabricated for MIR [81]. Recently, in 2016, J. Charrier et al. reported a fully etched GeSbSe waveguide with a RI contrast of 0.33, showing propagation losses of 2.5 dB/cm at λ = 7.7 µm and also demonstrated detection of methane and nitrous oxide [82].

Materials used for this work: The state-of-the-art discussed above shows that there is a large number of potential materials available for various MIR applications. Each material systems have their pros and cons. Since the present work is based on the fabrication and characterization of waveguides for MIR sensing by utilizing the molecular fingerprint region that lies at longer MIR wavelengths (6-16 µm), the material system required both the core and the substrate should be transparent up to atleast 16 µm. Materials used in this work are two chalcogenide compositions, germanium telluride ($GeTe_4$) as the waveguide core material with a high RI of 3.3 at λ = 10.0 µm and broad MIR transparency at wavelengths from 2-20 µm. Zinc selenide (ZnSe) as a substrate with a RI of 2.4 at λ = 10.0 µm and broad transparency from visible to 16 µm in the MIR. The RI contrast between $GeTe_4$ core and ZnSe substrate is high ~0.9, which allows realization of single mode waveguides with small cross-sections, hence compact designs. It is also

advantageous for strong optical confinement and aids in enhanced surface optical intensities required for evanescent field based sensing. Moreover, chalcogenide materials are easily deposited by commonly used physical or chemical vapor deposition techniques and are compatible with current CMOS technology for lithography and etching. In this work $GeTe_4$ waveguides are fabricated on both bulk ZnSe substrate (discussed in Chapter 4) as well as on Si substrate with a thick ZnSe isolation layer in between (discussed in Chapter 6) and are characterized for waveguiding in the MIR.

In 2011, A. Pradel group have shown a similar composition of $GeTe_4$ rib waveguides fabricated on $Te_{75}Ge_{15}Ga_{10}$ bulk glass substrate for spatial interferometry in the search for earth-like planets in the MIR range of 6-20 μm. Here the refractive index contrast between the core and the substrate was about quite low (4×10^{-2}) and so 24-32 μm thick $GeTe_4$ layers were deposited and fabricated into rib structures to demonstrate waveguiding at 10.6 μm and over the 2-5 μm spectral range, however, no further characterization on mode profile or propagation losses were reported [83-85]. Later in 2015, they reported a buried channel waveguide with a similar composition, this time adding a ~15 μm thick superstrate layer of $Ge_{24}Te_{76}$ on the waveguide and reported propagation losses of 6.6 dB/cm at $\lambda = 10.6$ μm [86].

Since ZnSe has a high refractive index (n~2.4) and has MIR transparency up to 16 μm, so thin film ZnSe waveguides were also fabricated on oxidised Si to exploit the MWIR band (2.5-4.0 μm wavelengths) explained in detail in Chapter 5. ZnSe is an important group II-VI optoelectronic material which has been used in many electronic properties such as wide and direct bandgap, low electrical resistivity, n-type conductivity. The deposition and characterization of thin films of ZnSe has been widely studied and used in various optoelectronic devices and applications such as LEDs, laser diodes, MIR sources, solar cells [87-91], optical windows, lenses and prisms. Low-loss waveguides have been realized in ZnSe substrates by methods such as diamond dicing [92], laser writing [93], proton implantation [94] and a macroscopic Fourier transform infrared – attenuated total reflection (FTIR-ATR) waveguide element has been used for the detection of DNA hybridization [95]. Epitaxial ZnSe thin films are usually grown on GaAs substrates to achieve lattice matching (0.27% mismatch) for applications in laser diodes [88], solar cells [89], second-harmonic generation [96] and non-linear switching [97]. However, the

deposition of non-epitaxial several microns thick films of ZnSe on silicon (Si) is challenging mainly because of dissimilar thermal expansion and distinct chemical properties [98].

The important MIR materials along with their refractive indices and MIR transparency are tabulated in Table 1.1 below. The materials used in this work are highlighted in the Table 1.1.

Table 1.1 MIR transparent materials

Material	Composition	Ref index	MIR Transmission	Reference
Silver halide	$AgCl_xBr_{1-x}$	1.98 – 2.16 (proportional to 1-x)	3 – 20 μm	[19, 20]
Group IV	Si	3.42 (at λ= 5 μm)	1.2 – 8 μm	[31, 40]
	SiO_2	1.46 (at λ= 5 μm)	0.2 – 3.7 μm	[23, 27, 40]
	Si_3N_4	2.33 (at λ= 5 μm)	0.5 – 6.5 μm	[33, 40]
	Ge	4 (at λ= 6 μm)	2 – 15 μm	[34, 40]
	C (Diamond)	2.38 (at λ= 5 μm)	0.3 – 2.5 μm, 7 – 100 μm	[39, 40]
Group III-V	GaAs	3.3 (at λ= 6 μm)	1 – 15 μm	[40, 41]
	AlGaAs	3.2 (at λ=6 μm)	1 – 15 μm	[40, 41]
	InP	3.0 (at λ=10.0 μm)	1 – 14 μm	[44]
Chalcogenides	As_2S_3	2.39 – 2.38 (at λ ~1 μm)	2 – 6 μm	[40, 69, 76]
	GaLaS	2.4	0.5 – 8 μm	[67]
	Ge-Sb-S	2.24 (at λ=1.55 μm)	2.5– 7.7 μm	[53, 80]
	As_2Se_3	2.78	2 – 9 μm	[41,76]
	GeAsSe	2.5-2.6 (at λ=1 μm)	2.5 – 6.6 μm	[68]
	TeAsSe	2.82	2 – 12 μm	[40]
	ZnSe	**2.4 (at 10 μm)**	**0.6 – 16 μm**	**[48]**
	$GeTe_4$	**3.3 (at 10 μm)**	**2 – 20 μm**	**[48]**

Tellurium and selenium based chalcogenide waveguide materials were selected to realise waveguides in this work due to their broadband transparency in the MIR as well as high refractive indices. The chalcogenide materials are different in their physical and chemical properties than the conventionally used Si and silica materials. Chalcogenides are physically soft and need to be handled very gently. Chemically these materials are

attacked by atmospheric oxygen so need to be stored in a desiccator. While depositing thin films, one needs to take care about the thermal expansion coefficient of the film as well as the substrate because thermal expansion mismatch causes delamination of the deposited films. Table 1.2 summarises different properties of ZnSe, $GeTe_4$, Si and silica.

Table 1.2 Properties of ZnSe and $GeTe_4$

Property	ZnSe	$GeTe_4$	Si	Silica
Density (g/cc)	5.27	6.14	2.32	2.2
Melting point (°C)	1525 [12]	~380 [99]	1414 [102]	1600 [103]
Thermal expansion (/°C) at 273 K	7.1×10^{-6} [12]	-	2.6×10^{-6} [102]	0.55×10^{-6} [103]
Hardness (Kg/mm^2)	120 [12]	< 100 [101]	1150 [102]	500 [103]
Band gap (eV)	2.7-2.8 [12]	0.1-0.8 [100]	1.12 [102]	-
Crystal structure	Polycrystalline wurtzite (hexagonal) or zinc blende (cubic)	Tetrahedral [99] *$GeTe_4$ used in this work is amorphous	Cubic [102]	Glass
Solubility	Insoluble in water but reacts with strong acids and bases [12]	Reacts with water and strong acids and bases	-	-

Loss mechanisms in infrared materials [164]:

Loss mechanism in materials involves two phenomena, one is the absorption of radiation where light is converted into heat and the other is scattering, where the radiation is diverted from its primary propagation path. In real circumstances, the above mentioned loss mechanisms are accompanied by extrinsic contributions from impurities and various structural imperfections.

Absorption: The optical window which is referred as the frequency regime where the material is intrinsically transparent is bounded by two intrinsic absorption edges. The long-wavelength side carries absorption from lattice vibrations, which is called the multiphonon edge. Here a photon is absorbed by the lattice via interactions between one or more phonons. These effects are induced due to non-linearity between the polarization and electric field or anharmonicity of the phonon modes. The short wavelength region is dominated by absorption from electronic excitations between the filled valence band and the empty conduction band, which is called as the electronic bandgap edge. It represents the cut-off of a material corresponding to the energy gap between the valence and conduction band. In addition to the electron-hole interaction, the perturbations are also induced by non-periodicity of the lattice or thermally excited lattice vibrations (Urbach tail). Apart from the above absorptions, the extrinsic absorptions are caused by presence of impurities during deposition or fabrication.

Scattering: When atoms in a solid are subjected to a propagating EM field, an electric dipole is created that radiates in all the directions. In a perfectly homogeneous medium, the scattered wavelets cancel each other in all directions except forward. The scattered light in the forward direction combines with the incident radiation to define wave velocity. At room temperature, in a practical solid material, many diffusive and propagating excitations occur leading to scattering. This effect is dependent on the variation of dielectric constant with the size of inhomogeneous medium. Rayleigh scattering is a fundamental scattering mechanism caused by inhomogeneity smaller than then the size of wavelength. The loss due to Rayleigh scattering is proportional to λ^{-4} and hence decreases rapidly with increase in wavelength. When the scattering region approaches or exceeds λ, it is referred as Mie scattering. In crystals, when the volume

fluctuations are induced by acoustic phonons (Brillouin scattering), the inelastic scattering is induced by a shift in the scattered frequency from the incident frequency. When the inelastic scattering is induced by optic phonons, it is called Raman scattering.

1.3 MIR absorption spectroscopy

Absorption spectroscopy refers to the spectroscopic techniques that measure absorption of radiation due to its interaction with the analyte (gas, liquid or solid) as a function of wavelength or frequency. Different materials absorb different wavelengths according to their chemical or molecular make-up. Absorption spectroscopy involves molecular transitions from electronic, vibrational and rotational energy states each corresponding to absorption at different wavelength bands. MIR absorption spectroscopy involves vibrational transitions of molecules because infrared photons have energies similar to the vibrational energies of molecular bonds. Molecules in any state of matter are in a constant vibrational motion that contributes to a part of their internal energy and molecules manifest this energy by stretching, twisting, bending, scissoring and wagging. Each of these intermolecular vibrations have a specific frequency, which depends on the molecular mass, shape, the relative position and type of neighbouring bonds, bond angles, bond length, bond strengths and symmetry. Only those vibrations that undergo a net dipole change during the vibration absorb IR radiation and are IR-active [104]. If there is no polarity in the molecule, then it will remain infrared inactive. When incoming MIR radiation interacts with the biochemical species, its oscillating electric field will cause the bonds of a polar molecule to vibrate. When the frequency of the oscillating field is equal to the natural vibration frequency of the molecule, which is called the resonance condition, energy is absorbed from the incoming MIR radiation at that frequency to induce a particular molecular vibration to vibrate with greater amplitude and unchanged frequency. The transmission spectrum of the waveguide recorded using MIR detector will show the missing frequency or wavelength absorbed by the molecule. Since a molecule of any composition and shape has definite calculable vibrational modes, depending on its molecular symmetries, it can be identified by examination of its transmission or absorption spectrum.

In absorption spectroscopy, calculation of limit of detection (LOD) is important as it defines the lowest concentration of analyte that can be detected reliably and accurately. It is a limitation of the measurement system and not the waveguide sensor. In terms of signal to noise (S/N) ratio, LOD is thrice the measurable signal from the low concentration of analyte in the sample as compared to noise (signal without the sample). S/N of the experimental set-up is crucial for LOD and is discussed in Chapter 7 where experimental measurement of IPA on waveguide sample is performed.

MIR absorption spectroscopic techniques based on interaction of light and matter have been studied both in *in vivo* and *in vitro*. The conventional MIR spectrometer such as Fourier transform infrared spectroscopy (FTIR) based on an interferometer is a non-destructive analytical technique developed in the 1960's [105]. The IR-active molecules to be tested are placed in the optical path such that their characteristic absorption features appear in the IR spectrum. This technique has been routinely used in research and industry for a number of applications such as assessment of archaeological samples [106], molecular structure determination, determination of absorption or transmission of various bio-chemical species [107], measurement of pollutants or trace gases in atmosphere [108-110] and kinetics and diagnosis of bio-molecules [111-113]. An FTIR with a ZnSe flow cell was used to determine the glucose concentration in whole blood [114].

1.4 MIR Evanescent sensing

When light is incident at the interface between a high RI core and a low RI cover/substrate, it undergoes total internal reflection (TIR) when the incident angle is greater than the critical angle at that interface, and light is guided in the core. This results in an exponentially decaying EM field in the lower RI medium known as an evanescent field, propagating along the waveguide surface and decreasing away from the boundary. It is present at both the film/cover and film/substrate. Evanescent field interacts with the analytes present within its penetration depth, d_P, which is given by the relation:

$$d_p = \frac{\lambda}{2\pi\sqrt{n_{core}^2 sin^2\theta - n_{air}^2}} \qquad 1.1$$

[40]

where λ is wavelength of incident radiation, θ is the angle of incident of the photons at the waveguide interface, n_{core} and n_{air} is the refractive index of the core and the superstrate (air in this case) respectively. When the analyte interacts with the film/cover interface, there is a change in the cover index; hence effective index of the waveguide will also change as a result of changes in optical path length and phase shift of the reflected light. This change in real or imaginary part of effective index is then measured. This is the fundamental premise of evanescent sensing in a waveguide. In this work, change in the imaginary effective index is measured by examining the absorption spectra of the analytes on the surface of planar waveguides as shown in Fig. 1.4.

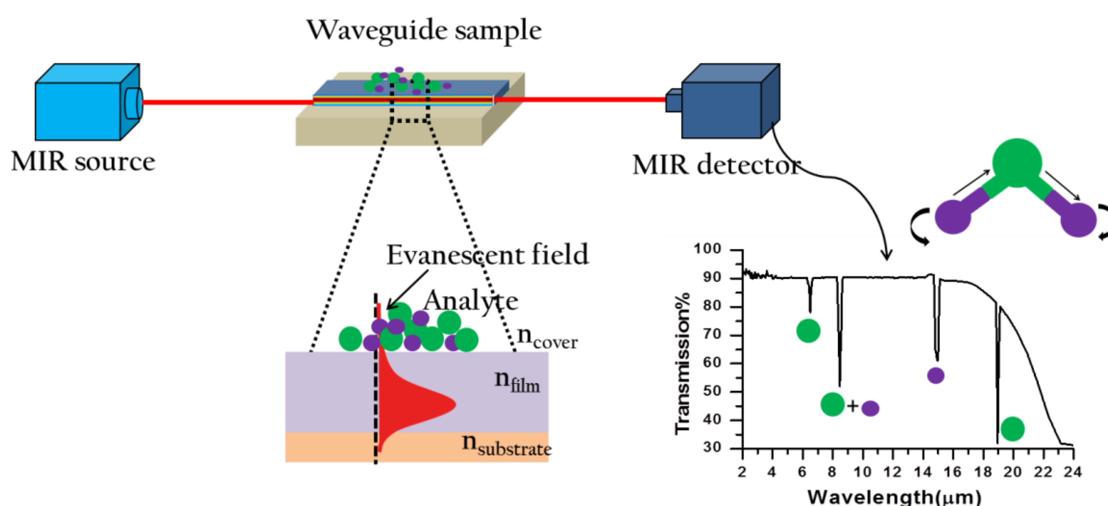

Fig. 1.4 Evanescent field based sensing of biomolecules in the mid-infrared region: light is coupled into the single mode waveguide and the transmission spectrum of the guided light is detected in the waveguide, with a biological analyte on its surface

Attenuated total reflection (ATR), which is a planar waveguide and follows the principle of TIR at the interface of two dielectric media creating an evanescent field is routinely used in analysis of thin films, solids and liquids in combination with FTIR. It is used to determine the analytical information down to ppb levels, such as concentration of hydrocarbon pollutants [105, 115, 116], low and high density polyethylene [117], chloroform which is considered to be carcinogenic and unsafe if present in more than 300 ppb in drinking water [118], detection of DNA hybridization [100].

The FTIR-ATR technique is limited by a number of factors such as some commonly used material of ATR element such as ZnSe is attacked by strong acids and bases that limits the detection of reactive species using ATR. It is also limited by the size of an ATR element.

The typical thickness of the ATR element is larger than the wavelength of propagating light and hence allows fewer reflections or bounces of the IR light along the long axis of the waveguide which limits the effective path length. As a result the sensitivity of the device is limited. To overcome these problems, a new FTIR accessory called fiber evanescent wave sensing (FEWS) was developed. Fiber optics can be considered as elongated ATR elements, which allows an increased number of reflections and hence enhanced sensitivity. A variety of research work has been carried out using FTIR-FEWS system such as a silver halide fiber was used to determine organic compounds in water [119,120], a chalcogenide fiber was used to determine spectral modification due to cerebral metabolism in a rat [121], protein identification and detection was carried out using MIR hollow fibers [122] and Se and Te based chalcogenide fibers were used to study human serum [123]. Recently, a silver halide fiber coupled photo acoustic sensor for glucose sensing in aqueous solution is shown to have a limit of detection (LOD) 57 mg/dL between λ = 9-10 μm [124]. The same paper also demonstrates the preliminary results on in vivo human skin spectra at the fingertip and forearm.

FEWS is an effective method for MIR sensing but it is not very practical as fiber assembly is a very sensitive to mechanical vibrations, they are difficult to integrate with other optical components on the same chip, fibers need cleaving and polishing which needs due maintenance and care in handling. These systems are bulky and not practical to be used for point of care applications. Planar waveguides on the other hand, are more robust, integrable to electronics and microfluidics and are a most effective platform for sensing applications. It is essentially an ATR element which is a lot thinner. As the number of reflections is approximately inversely proportional to the thickness of waveguiding layer, by decreasing the waveguide thickness, the discrete reflections are reduced to a continuous evanescent wave along the waveguide surface [38]. For a single mode waveguide, the number of totally internally reflected rays is reduced to one, allowing a single guided mode propagating with a unique propagation constant. It is shown in Fig. 1.5.

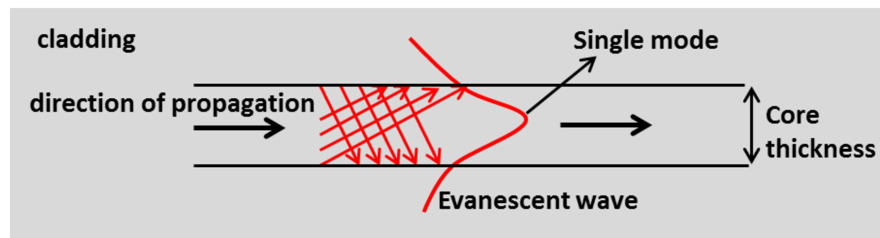

Fig. 1.5 Wave-model describing single mode guidance

1.5 MIR absorption biosensing

There is little published work on integrated waveguide evanescent field based sensing in the MIR. Air cladded Si pedestal waveguides were shown by J. Hu group to evaluate the absorption of organic mixtures of different concentrations of analytes such as methanol, toluene, hexane, water and acetone at MWIR [125]. The same group published results on spectroscopy of ethanol, toluene and isopropanol (IPA) at a wavelength of 5.2 µm, showing LOD as 0.05 ng for ethanol, 0.06 ng for toluene and 0.09 ng for IPA on Si microring cavities fabricated on a CaF_2 substrate [126]. The group of B. Mizaikoff has done most of the work using integrated waveguides for chemical sensing. They showed LOD of acetic anhydride to be 19.4 ng on GaAs/AlGaAs ridge waveguides at λ = 10.2 µm [37]. They also demonstrated polycrystalline diamond films grown using CVD on silicon nitride coated Si and oxidised silicon were made into strip waveguides by ICP etching were demonstrated to detection of acetone in D_2O with a detection volume of 200 pL [36]. This group has also worked on grating couplers on silver halide waveguides for analysing acetic acid at λ = 10.4 µm [127]. The group of F. N. de Rooij has demonstrated Ge on Si ridge waveguides integrated with microfluidic system using polydimethylsiloxane for detection of cocaine dissolved in tetrachloroethane at λ = 5.71 µm with the LOD of 100 µg/mL [128]. Recently, the group of J. Charrier presented results on evanescent field gas sensing of methane and nitrous oxide on a multilayer GeSbSe chalcogenide waveguides fabricated on Si working at λ = 7.7 µm, with LOD 14.2 ppm and 1.6 ppm for methane and nitrous oxide respectively, [129].

Table 1.3 Comparison of various MIR waveguide/analyte systems for sensing

Ref.	Waveguide/ substrate	Wavelength (μm)	Analyte	Matrix	detector	Limit of detection
[36]	Diamond waveguide on Si_3N_4 on oxidised Si substrate	5.78 – 6.35	Acetone	Deuterium oxide (D_2O)	Liquid nitrogen cooled MCT	200 pL
[37]	GaAs/AlGaAs waveguide on Si-doped GaAs substrate	10.3	Acetic anhydride	Diethylene glycol monoethyl ether(DGME)	Liquid nitrogen cooled MCT	18 pL
[37]	HgCdTe waveguide on CdTe substrate	5.78 – 6.35	Acetone	Isopropanol	Liquid nitrogen cooled MCT	2 nL
[125], [126]	Si microring resonators on CaF_2 substrate	5.2	Ethanol, Toluene, Isopropanol	Cyclohexane	Focal plane array	0.05 ng 0.06 ng 0.09 ng
[127]	Silver halide waveguides	10.4	Acetic acid	Water	Liquid nitrogen cooled MCT	-
[128]	Ge waveguide on Si substrate	5.71	Cocaine	Saliva	Liquid nitrogen cooled MCT	100 μg/mL
[129]	Ge-Sb-Se waveguides on Si	7.7	Methane and nitrous oxide	-	Thermographic camera	14.2 ppm 1.6 ppm

There is a lot of potential for waveguide evanescent field sensing of biochemical species for real and practical applications. There is a little published work on waveguide evanescent field MIR sensing of aqueous analyte because of number of reasons; MIR materials, optics, and technology is not fully matured. MIR region is dominated by water absorption, which makes it difficult for spectroscopy of aqueous analytes. There are ways to tackle water absorption problem, which are briefly discussed in chapter 7 of this thesis. This work is focussed to develop mass-producible cost-effective integrated optical waveguides suitable for label-free sensing of aqueous analyte in the MIR region.

1.6 Main directions of the project

The project involved identification of materials suitable for MIR wavelengths in terms of their spectral transparency, refractive index, mechanical and chemical stability at room temperature and ease in fabrication of devices. The two chalcogenide materials $GeTe_4$ and ZnSe were selected and used as the waveguide core and substrate in this work. $GeTe_4$ was deposited in thin films by using RF sputtering. $GeTe_4$ thin films were characterised for their structure, composition and optical properties. Lateral and vertical dimensions for channel and rib waveguides were calculated using Comsol numerical modelling. The films were fabricated into channel and rib waveguides using standard microfabrication techniques such as photolithography, lift-off and dry etching. The fabricated waveguides were characterised for waveguiding, mode profile and propagation losses at MIR wavelengths.

An additional scheme for CMOS compatible fabrication of chalcogenide waveguides was followed by depositing both $GeTe_4$ core and ZnSe lower cladding on Si substrate for many advantages discussed in section 2.3 of chapter 2. Comsol numerical modelling was used to calculate the thickness of lower cladding/isolation layer. The ZnSe isolation layer was deposited by RF sputtering and thermal evaporation. The optical quality of the deposited films were compared and reported.

A sensitivity model using Comsol was also prepared to model $GeTe_4$ waveguide thickness and length for optimal sensitivity with water as the waveguide cover region. A representative model analyte (IPA), which has distinct absorption peaks in the MWIR (λ = 2.7-3.5 μm) is used in the modelling and tested optically on the surface of the waveguides

in the MIR region. Finally, experimental results were compared with theory and future work is proposed. The results presented on spectroscopy are preliminary work carried out to establish the sensing set up paving the way for future measurements using biological species.

1.7 Structure of the thesis

Chapter 1 has introduced the project and the state of the art of materials, waveguides and biosensing in MIR. It also briefly explains the key concept of evanescent field sensing in the MIR region. Chapter 2 discusses the theory and modelling of waveguides. It explains the concept of light confinement and modes in a slab waveguide by ray and wave model. It also shows waveguide dimensions calculated by Comsol for single mode criterion. Bend losses of the waveguides were also calculated theoretically. It also discusses a theoretical model on waveguide sensing of the bulk analyte for surface sensitivity. In chapter 3, experimental tools and procedures used to carry out the deposition, characterization of thin films, fabrication of the channel and rib waveguides and the experimental setup used to characterize waveguides in MIR is discussed. Chapter 4, describes the optimization of $GeTe_4$ film deposition by RF sputtering along with structural, compositional and optical characterizations. It also describes the results on fabrication and optical characterization of $GeTe_4$ waveguides on bulk ZnSe for MWIR and LWIR regions. Chapter 5 presents the systematic and detailed study on deposition of ZnSe films on Si by RF sputtering and thermal evaporation and film characterizations. It also discusses the fabrication of ZnSe waveguides on oxidised Si and propagation losses in MWIR. Chapter 6 describes the $GeTe_4$ waveguides with ZnSe film as a lower cladding/isolation layer on Si. Here an optimised process of etching of $GeTe_4$ is also shown. In chapter 7, experimental results on sensing of IPA on waveguide surfaces and its comparison with the theoretical model is presented. Chapter 8 summarizes the conclusions and proposes the future work.

Appendix A discusses the dry etching of $GeTe_4$ films using reactive ion etching and inductively coupled plasma etching.

Appendix B discusses a theoretical model based on Comsol modelling to show the concept of mode stripping by changing isolation layer thickness for chalcogenide waveguides.

CHAPTER 2 Theory and modelling of waveguides for sensitive surface absorption spectroscopy

Dielectric waveguides are the key components of integrated optics. This chapter explains the basic waveguide theory starting with the simplest case of a planar slab waveguide which is a good first approximation to understand the basic concepts of mode propagation and physical understanding of an optical waveguide. Since a ray model is simple and intuitive, it is used to describe light confinement and polarisation in a slab waveguide in section 2.1.1. It is then extended to a wave-optic model employing Maxwell's equations for describing field profiles in section 2.1.2. Comsol numerical modeling is used to simulate two dimensional (2D) $GeTe_4$ waveguides with fully etched (channel) and partially etched (rib) geometries for single mode condition. Bend losses in these waveguides are also discussed. Comsol is also used to model the thickness of an isolation layer needed between a chalcogenide material core and a high refractive index (RI) Si substrate to confine the mode in chalcogenide core and to avoid significant light penetration into Si. Finally, a sensitivity model for a slab waveguide is designed using Comsol to determine the cross-section and length of the waveguide where it is most sensitive to detect a small change in absorption in a bulk aqueous medium on the surface of the waveguide.

2.1 Planar slab waveguides

An optical dielectric waveguide refers to a structure that is able to confine and guide electromagnetic (EM) waves. It consists of a high index dielectric material known as the core, where the light is confined, surrounded by a low index media known as the upper cover or lower substrate. If both the lower and upper media surrounding a waveguide core are same, it is a symmetrical waveguide; if they are different it is an asymmetrical waveguide [130]. For sensing applications, asymmetrical waveguides with a solid substrate underneath the waveguide core is preferred (generally air-cladded), because they are convenient to use. For this reason, only asymmetrical waveguides are considered in this chapter.

2.1.1 The ray model for a slab waveguide

Light propagation in waveguides can be exactly described by Maxwell's equations, yet a classical geometrical approach using a ray model provides a good approximation to introduce the concepts of propagation of light in a waveguide and its physical understanding. A dielectric slab waveguide which confines the light in one direction is considered, with no losses due to absorption or scattering. The theory is explained by referring to literature [130-134]. An asymmetrical waveguide structure which is infinite in x and z direction and has three regions shown in Fig. 2.1 (a), with central region with a RI (n) n_f, which forms the core/film of the waveguide surrounded by a substrate and a cover region with RIs n_s and n_{cov} respectively such that $n_f > n_s, n_{cov}$ is considered. We also assume $n_s > n_{cov}$, which is normally true. A schematic of the side view of a slab waveguide is shown in Fig. 2.1 (a), where we assume that light in the waveguide is propagating in the z direction in a zigzag manner and light confinement occurs transversely in the y direction and the structure is uniform in the x and z directions. When an incident light with wavelength ($\lambda = \lambda_0/n$) is coupled into the waveguide cross-section, the light is confined in the film by total internal reflection (TIR). λ_0 is the wavelength of light in free space. The angle of incidence at which TIR takes place is known as the critical angle. The critical angles that define the TIR for the cover-film interface (θ_{cov}) and the film-substrate interface (θ_s) are given by:

$$\theta_{cov} = sin^{-1}\left(\frac{n_{cov}}{n_f}\right) \qquad 2.1$$

$$\theta_s = sin^{-1}\left(\frac{n_s}{n_f}\right) \qquad 2.2$$

From $n_f > n_s > n_{co}$, we have $\theta_s > \theta_{cov}$

The first condition for the incident radiation to be confined in the core region is that the incident ray should propagate with an internal angle θ_f in the core region, should be large enough, such that it follows, $\theta_s < \theta_f < \pi/2$.

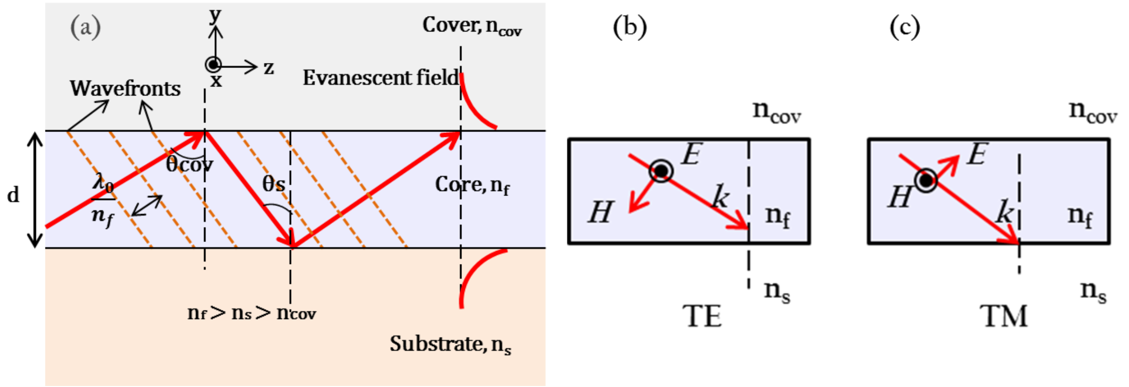

Fig. 2.1 (a) Side view of a slab waveguide showing ray and wavefront picture (b) TE and (c) TM polarisations (adapted from [130])

For an optical wave of angular frequency ω, the relationship between propagation constant β, wave vector k_0, and effective index n_{eff}, is given by the following equations.

$$k_0 = \frac{2\pi}{\lambda_0} = \frac{n_f}{c}\omega \qquad 2.3$$

$$\beta = k_0\, n_{eff}\,; \qquad n_{eff} = n_f \sin\theta_f \qquad 2.4$$

$$\beta = k_0\, n_f \sin\theta_f \qquad 2.5$$

where β is the component of wavevector along the propagation direction and n_{eff} is the measure of phase velocity of the guided mode and represents the refractive index experienced by the guided mode.

As the ray is reflected back and forth between the two interfaces, it interferes with itself and a guided mode exists when a repeated reflected ray has constructive interference with itself. A ray suffers a transversal phase shift τ_r in a round trip inside the core, depending on the core thickness and wavelength of incident light. From Fig 2.1 (a), the y component of wave vector, $k_y = k_0 \cos\theta_f$ and z component $k_z = k_0 \sin\theta_f$. The transverse round trip phase shift is given by $2k_0\, n\, d\cos\theta_f$. The second condition that establishes the guided mode is based upon constructive interference which implies that the total transversal phase shift in a round trip should be either zero or an integral multiple of 2π radians. τ_{cov} and τ_s are the phase shifts upon reflection at both the interfaces cover and substrate respectively and depends on the angle of reflection θ and the polarisation of the mode.

$$2k_0 d\, n_f cos\theta_f + \tau_{cov} + \tau_s = 2\pi m \qquad 2.6$$

where m = 0,1,2,3,… (mode number)

For a single mode waveguide there is only one specific angle that fulfils this condition. As the thickness of the waveguide increases, more discrete angles fulfil the above condition. Each of these specific angles corresponds to guided modes. Equation 2.6 can be solved numerically to obtain the modal angles.

For a slab waveguide, the light is confined in only the transverse direction, so there are two cases of light polarization. The transverse electric (TE) polarisation, where the electric field is perpendicular to the plane of incidence, i.e. if we define plane of incidence as y-z, the electric field is pointing in the x direction. From Fig. 2.1 (b) the electric field vector lies entirely in the xy plane and its components along the y and z axes are zero, $E_y = E_z = 0$, which implies the electric field is transverse to the direction of propagation. Similarly, from Fig. 2.1 (c), transverse magnetic (TM) mode can be defined as when magnetic field points in the x direction and $H_y = H_z = 0$, here electric field is no longer purely transverse and has a component along the z axis. For the TE polarisation, the phase shift at the two interfaces is given by:

$$tan\frac{\tau_{cov}}{2} = \sqrt{\frac{sin^2\theta_f - sin^2\theta_{cov}}{cos\theta_f}} \qquad 2.7$$

$$tan\frac{\tau_s}{2} = \sqrt{\frac{sin^2\theta_f - sin^2\theta_s}{cos\theta_f}} \quad 2.8$$

Substituting $\sin\theta_{cov}$ and $\sin\theta_s$ from equations 2.1 and 2.2 and n_{eff} from equations 2.4 and τ_{co} and τ_s from equations 2.7 and 2.8 into equation 2.6, for TE polarisation we obtain:

$$k_0 d\sqrt{n_f^2 - n_{eff}^2} - arc\tan\sqrt{\frac{n_{eff}^2 - n_{cov}^2}{n_f^2 - n_{eff}^2}} - arc\tan\sqrt{\frac{n_{eff}^2 - n_s^2}{n_f^2 - n_{eff}^2}} = m\pi \quad 2.9$$

For TM polarisation we obtain:

$$k_0 d\sqrt{n_f^2 - n_{eff}^2} - arc\tan\sqrt{\frac{n_{co}}{n_f}}\sqrt{\frac{n_{eff}^2 - n_{co}n_f}{n_f^2 - n_{eff}^2}} - arc\tan\sqrt{\frac{n_s}{n_f}}\sqrt{\frac{n_{eff}^2 - n_s n_f}{n_f^2 - n_{eff}^2}} = m\pi \quad 2.10$$

The fundamental mode is a guided mode with m = 0, and higher order modes are obtained when it is an integer and m ≠ 0. Ray-optics provides qualitative description of behaviour of light in a waveguide, but cannot be used to describe optical field distribution of radiation in a waveguide, we must resort to wave-optics description of EM theory. EM field profiles in one dimensional slab waveguides can be found by using Maxwell's equations which is discussed in the following section.

2.1.2 The wave model for a slab waveguide

For wavelengths of light comparable to waveguide dimensions (~ core thickness), Maxwell's equations are used, which are a set of four coupled equations that govern how electric and magnetic fields propagate, interact, and are influenced by objects. The solutions of Maxwell's equations for waveguides are known as modes, which are eigen functions of the equation system. A waveguide mode is distinguished by a field distribution whose amplitude and polarisation are constant along the longitudinal direction of propagation. It depends on operating wavelength, geometry and refractive indices of the waveguide. We consider a field *f* depending on time and position, which

allows the derivation of the relation between angular frequency ω and wave vector k. This field can be an electric or magnetic field.

$$f(t,z) \sim e^{-i\omega t} e^{i\boldsymbol{k}.\boldsymbol{z}} \qquad 2.11$$

The four Maxwell's equations in a material medium are:

$$\nabla.\boldsymbol{D} = \rho \qquad 2.12$$

$$\nabla.\boldsymbol{B} = 0 \qquad 2.13$$

$$\nabla X \boldsymbol{H} = \frac{d\boldsymbol{D}}{dt} + \boldsymbol{J} \qquad 2.14$$

$$\nabla X \boldsymbol{E} = -\frac{d\boldsymbol{B}}{dt} \qquad 2.15$$

where ρ and $\boldsymbol{J}$ are the charge and current densities respectively. ***D, B, H*** and ***E*** are electric displacement vector, magnetic induction, magnetic and electric field strengths respectively. Also,

$$\boldsymbol{D} = \varepsilon\boldsymbol{E} = n^2\varepsilon_0\boldsymbol{E} + \boldsymbol{P} \qquad 2.16$$

$$\boldsymbol{B} = \mu\boldsymbol{E} = n^2\mu_0\boldsymbol{E} + \boldsymbol{M} \qquad 2.17$$

ε is dielectric constant or permittivity and μ is permeability of the material. ***P*** and ***M*** are electric and magnetic polarizations. When an EM field is present in the matter, the electric field can perturb the motion of electrons and produce a dipole polarization ***P*** per unit volume and analogously magnetic field can also induce a magnetization ***M*** in materials. When the material is isotropic and non-magnetic, both ε and μ reduces to scalars, $\varepsilon = \varepsilon_0$ and $\mu = \mu_0$. Since in a dielectric waveguide, the material is non-conducting so ρ and $\boldsymbol{J} = 0$. If a medium is optically inhomogeneous, its refractive index is position dependant, n = n(**r**), then $\boldsymbol{D} = n^2\varepsilon_0\boldsymbol{E}$ and $\boldsymbol{B} = n^2\mu_0\boldsymbol{H}$. Rearranging the curl equations 2.14 and 2.15, and applying vector identities, we obtain the following simplified equations:

$$\nabla^2\boldsymbol{E} + \boldsymbol{\nabla}\left(\frac{1}{n^2}\nabla n^2\boldsymbol{E}\right) = \mu_0\varepsilon_0 n^2\frac{\partial^2\boldsymbol{E}}{\partial t^2} \qquad 2.18$$

$$\nabla^2 \boldsymbol{H} + \boldsymbol{\nabla}\left(\frac{1}{n^2}\nabla n^2 \boldsymbol{x}\, (\boldsymbol{\nabla}\, \boldsymbol{x}\, \boldsymbol{H})\right) = \mu_0 \varepsilon_0 n^2 \frac{\partial^2 H}{\partial t^2} \qquad 2.19$$

If n^2 is slowly varying in the distance of the order of wavelength so, $\nabla n^2 = 0$, then the second term on the left hand side of equations 2.18 and 2.19 can be neglected and fields ***E*** and ***H*** satisfy the wave equation. Assuming the refractive index of the medium depends only on one Cartesian coordinate, n = n(y), and propagation of light is along z-axis (refer Fig. 2.1 (a)) such that the wave has no dependence on x axis, the solutions of the above wave equations can be written as

$$\boldsymbol{E}\,(r,t) = \boldsymbol{E_a}(y) e^{i(\omega t - \beta z)} \qquad 2.20$$

$$\boldsymbol{H}\,(r,t) = \boldsymbol{H_a}(y) e^{i(\omega t - \beta z)} \qquad 2.21$$

where $\mathbf{E}_a$(y) and $\mathbf{H}_a$(y) are the complex field amplitudes. Now, the solutions for EM fields of a slab waveguide are reduced to finding out solutions for $\mathbf{E}_a$(y) and $\mathbf{H}_a$(y) as well as for β. From equations 2.20 and 2.21 we get six coupled equations in x,y and z axis for electric and magnetic fields, which are the modes of the waveguide and it represents the transverse field distribution which propagates in z direction with a phase velocity of ω/β. These modes can be confined in the waveguides or can be radiation modes that leak into substrate or cover region. Propagation modes can be calculated as two independent cases, TE and TM modes as discussed below.

For TE modes, the perpendicular component of the electric field corresponds to E_x, and E_y = E_z = H_y = 0. On substituting equations 2.20 and 2.21 in Maxwell's equations 2.14 and 2.15, the following coupled equations that relate the field amplitudes E_y, H_x and H_z are obtained:

$$H_x = -\left(\frac{\beta}{\omega \mu_0}\right) E_y \qquad 2.22$$

$$H_z = \left(\frac{i}{\omega \mu_0}\right) \frac{\partial E_y}{\partial x} \qquad 2.23$$

$$i\beta H_x + \frac{\partial H_z}{\partial x} = -i\omega\epsilon_0 n^2(x)E_y \qquad 2.24$$

On substituting H_x and H_z in equation 2.24, a second order ordinary differential equation is obtained where **E** is the function of x only:

$$\frac{d^2\boldsymbol{E_y(x)}}{dx^2} + (k_0^2\, n^2(x) - \beta^2)\boldsymbol{E_y}(x) = 0 \qquad 2.25$$

which is called the Helmholtz equation.

In order to resolve equation 2.25 for a planar structure, boundary conditions must be imposed at the interfaces. For TE propagation through an asymmetric waveguide, the boundary conditions imply the continuity of tangential components of electric field $\mathbf{E}_y$, magnetic field $\mathbf{H}_z$ and d$\mathbf{E}_y$/dx at the cover-film and film- substrate boundary.

Similarly for TM modes the non-zero components of electric and magnetic fields are E_x, E_z and H_y.

$$\frac{d^2\boldsymbol{H_y(x)}}{dx^2} + (k_0^2\, n^2(x) - \beta^2)\boldsymbol{H_y}(x) = 0 \qquad 2.26$$

In this case, the boundary conditions imply the continuity of transverse field components of electric and magnetic field to be continuous which leads to the continuity of $\mathbf{E}_z$, $\mathbf{H}_y$ and ($1/n^2$) d$\mathbf{H}_y$/dx field components at the interface.

From equations 2.25 and 2.26, general solutions can be inferred for $n_f > n_s > n_{cov}$, which are also presented in Fig. 2.2 [135], such that:

1. $\beta > k_0 n_f$ gives exponential solutions in all three regions. It implies infinite field amplitudes at large distances from the waveguide, which is physically unrealistic so these solutions are ignored.
2. $k_0 n_f > \beta > k_0 n_s$ gives discrete number of guided modes which are sinusoidal solutions in the core and decay exponentially outside the core in the cover and substrate

3. $k_0n_s > \beta > k_0n_{cov}$ gives sinusoidal solutions in both the core as well as the substrate while vary exponentially in the cover. These solutions are called substrate modes since these fully penetrate the substrate region.
4. $\beta < k_0n_{cov}$ gives a solution that varies sinusoidally in all three regions and are called radiation modes.

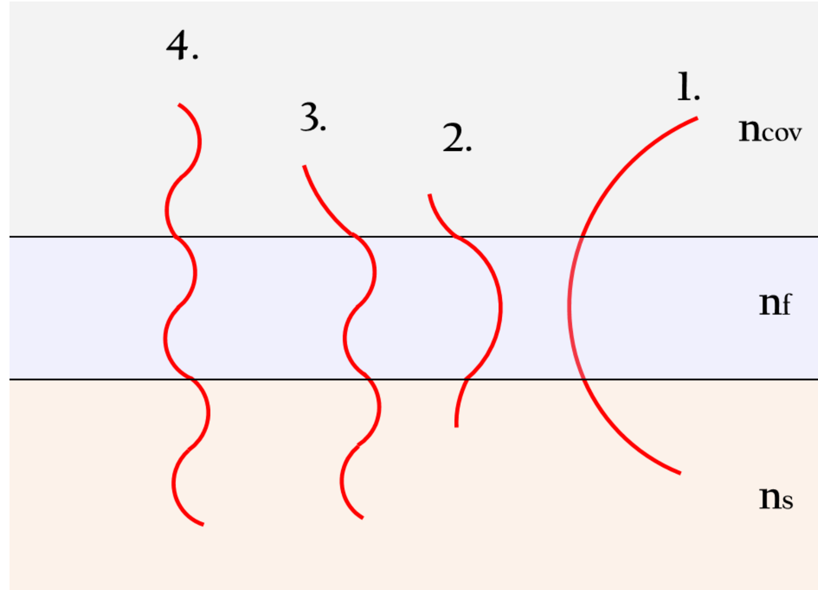

Fig. 2.2 Modal field distribution of an asymmetric slab waveguide (adapted from [135])

For more complex structures such as 2D channel and rib waveguides, numerical modelling is used to obtain the mode field patterns by solving the two equations 2.25 and 2.26 and imposing the above boundary conditions, which is discussed in the next section.

2.2 Simulation and design of 2D waveguides

Planar slab waveguides confine light in one dimension that supports transversal EM modes whereas a two dimensional waveguides confines light in two dimensions and allow TIR along the core thickness as well as at the lateral boundaries. It is described in Section 2.1 that slab waveguides have TE ($\mathbf{E}_z = 0$) or TM ($\mathbf{H}_z = 0$) modes depending on the orientation of electric or magnetic fields whereas 2D waveguides have hybrid modes where both $\mathbf{E}_z \neq 0$ and $\mathbf{H}_z \neq 0$. These are important for many applications as it confines light in two dimensions along the structure's main axis thereby restricting propagation in one dimension, without being diffracted as in the case of a slab waveguide where light

diffracts in the plane of the film. This allows fabrication of complex structures such as rib, channel, rings etc. to be used in modulators, interferometers, grating couplers, on-chip sensors and many other devices. Comsol multiphysics may be used to simulate both 1D and 2D waveguides. It is a finite element analysis solver and simulation software that treats multiple simultaneous physical phenomena involving solving coupled partial differential equation systems. It has many different modules for electronics, fluid and heat, chemical and so on. In this work the wave optics module in the frequency domain has been used which provides dedicated tools for electromagnetic wave propagation in linear and non-linear optical media. Matlab (**Ma**trix **lab**oratory from MathWorks) which is a numerical computing fourth generation computing language and Origin (Originlab) which is a scientific data analysis and graphing tool were used to plot the graphs.

2.2.1 Channel and rib waveguides

It is essential to design a waveguide before starting the fabrication to know the dimensions of the structures needed at a wavelength of interest. In this section channel and rib waveguides are designed to find out their lateral and vertical dimensions for a single mode condition at a representative wavelength of λ = 7.5 μm. A representative width and height for both channel and rib waveguide is selected and n_{eff} is calculated for λ = 2-10 μm, in both polarisations. Bend losses using Marcuse's work [137] has been described for the above selected channel and rib waveguide design at λ = 7.5 μm.

At λ = 7.5 μm, n of $GeTe_4$ is taken to be 3.264 and that of ZnSe is 2.416 (extracted from experimental data). For a $GeTe_4$ core and ZnSe substrate with an air cladding, a range of widths and heights of fully etched channel waveguides and partially etched rib waveguides were calculated using an online mode solver based on effective index method [136], at λ = 7.5 μm which are tabulated in table 2.1.

Table 2.1 $GeTe_4$ channel and rib waveguide dimensions at λ = 7.5 µm for single mode operation

	width (µm) X height (µm)
Channel	1.7 X 6.3 2.0 X 5.4 3.0 X 3.0 4.0 X 2.0
	width (µm) X rib height (µm) X slab height (µm)
Rib	1.7 X 1.3 X 2.2 2.0 X 0.7 X 2.2 3.0 X 0.5 X 2.0 4.0 X 0.3 X 2.0

A representative dimension for a channel (width = 3.0 µm and height = 2.0 µm) and a rib (width = 3.0 µm, rib height = 0.5 µm and slab height = 1.5 µm) waveguide is selected to simulate the mode field profiles of the waveguides at λ = 7.5 µm. E_x, E_y and E_z component of electric field distribution of a 2.0 µm thick and 3.0 µm wide $GeTe_4$ channel waveguides in TE and TM polarisations are shown in Fig. 2.3 at λ = 7.5 µm.

For the selected geometries of channel and rib waveguide at λ = 7.5 µm, n_{eff} for a range of wavelengths, λ = 2-10 µm is calculated using Comsol in both the polarisations and is shown in Fig. 2.4. It can be seen that n_{eff} decreases with wavelength for both channel and rib geometries for both polarisations. As the wavelength is increased, more light travels in the lower index medium, extending the evanescent field in both the cover and substrate of the waveguide, thereby decreasing the n_{eff}.

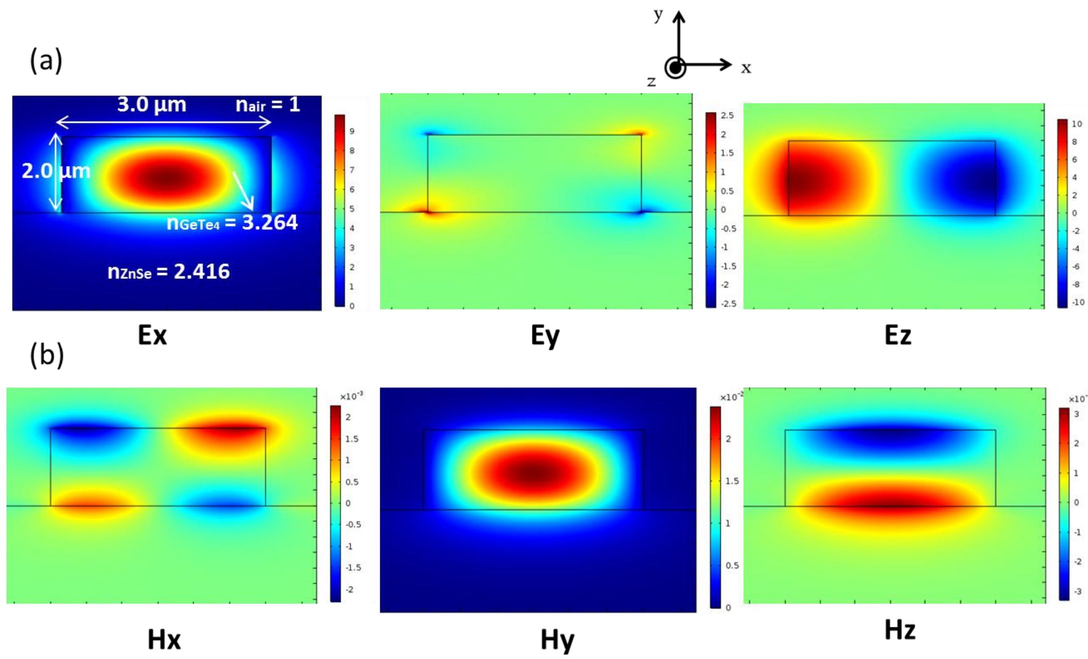

Fig. 2.3 Mode field distribution of the electric field components for (a) TE and (b) TM polarisations at λ = 7.5 µm for a channel waveguide

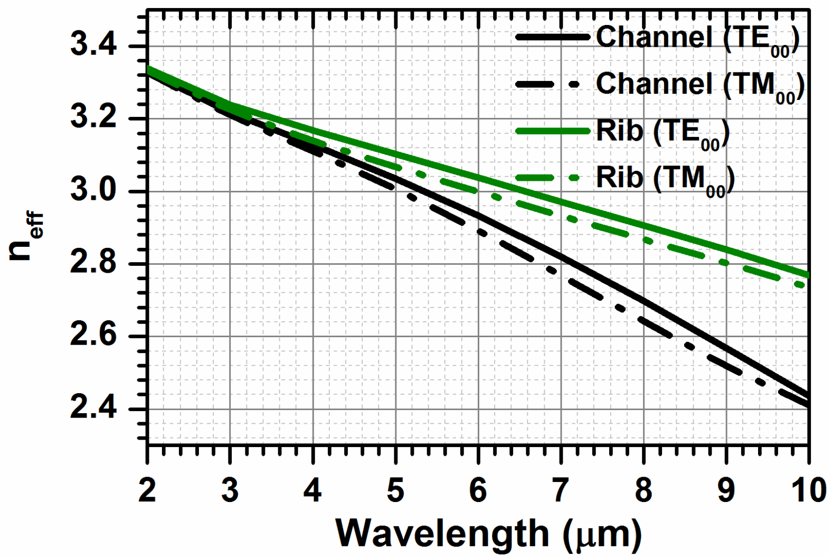

Fig. 2.4 n_{eff} of channel and rib $GeTe_4$ waveguides on ZnSe substrate simulated using Comsol

In designing the waveguides, there is a trade-off between single mode condition (waveguide dimensions are small) and high n_{eff} depending on the type of application. However, rib height and width can be manipulated to get the maximum n_{eff} while working within the single mode regime. The other advantage of using a rib waveguide is

that it has lower propagation losses as the mode does not interact with side walls of the waveguide which causes scattering of light. The advantage of using a channel waveguide is that it confines light more strongly and allows tight bending radii (refer section 2.2.2). For evanescent field sensing, the most desirable design is to have a single mode waveguide optimized for its surface sensitivity with its evanescent field interacting with the sensing medium on the cover region (discussed in section 2.4).

2.2.2 Bends

So far all the waveguides discussed have been described as straight 1D or 2D structures in the z-direction. For many photonic circuits and sensors (splitters, MZI's, MMI's), light guidance through bent waveguide structures is required. Designing of bends should be such that there is a gradual change in geometry from one direction to the other to have minimum losses. 2D analysis based on Marcuse's work is used for calculating bend losses in channel and rib waveguides [137]. Here a 2D waveguide structure is reduced to 1D using the effective index method and bend loss in dB's is calculated for a given angular section Δθ of radius R as

$$Loss_{bend} = -10\log(\exp(-\alpha_{bend}\,\Delta\theta R)) \qquad 2.27$$

Where α_{bend} is in radians and is known as the optical bending loss coefficient. It is given by:

$$\alpha_{bend} = \frac{\alpha_y^2}{k_0^3 n_e\left(1+\alpha_y\frac{w}{2}\right)}\frac{k_y^2}{(n_{e2}^2-n_{e1}^2)}\exp(\alpha_y w)\exp\left(\frac{-2\alpha_y^3}{3n_e^2k_0^2}R\right) \qquad 2.28$$

$$\alpha_y = k_0(n_e^2 - n_{e1}^2)^{1/2} \qquad 2.29$$

$$k_y = k_0(n_{e2}^2 - n_e^2)^{1/2} \qquad 2.30$$

$$k_0 = \frac{2\pi}{\lambda} \qquad 2.31$$

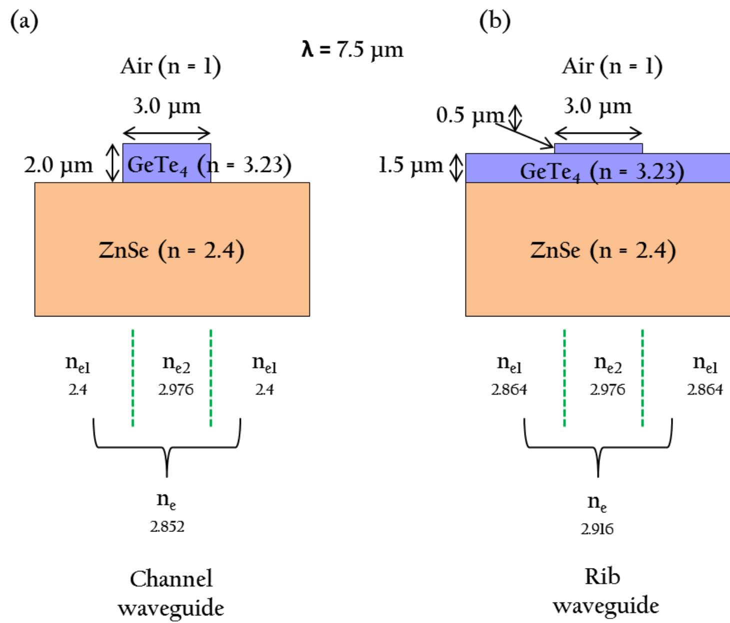

Fig. 2.5 Schematic of the (a) channel and (b) rib $GeTe_4$ waveguides on ZnSe substrate showing effective indices of the vertical and lateral regions

The effective indices n_e, n_{e1} and n_{e2} are calculated by Comsol for the example designs used for illustration, as shown in Fig. 2.5 for channel as well as rib geometries. The values of effective indices were used in equation 2.28 to estimate the bend losses. Fig. 2.6 (a) and (b) shows the bend losses calculated at three bend angles 30°, 60° and 90° for channel and rib waveguides respectively at λ = 7.5 μm. It can be seen that higher the angle, greater are the losses for both channel and rib waveguide. From Fig. 2.4 (a) and (b) the minimum bend radii needed to have losses of ~ 0.1 dB/cm for a 90° bend is 40 μm for a channel and 900 μm for a rib $GeTe_4$ waveguide. Rib waveguides exhibit lower light confinement compared to a channel waveguide because in a rib waveguide, a part of the light is leaked into the bottom partially etched slab, it therefore, requires high radii of curvature to reduce losses [138]. From these calculations, the bend radius was kept larger than 1 mm for the experimental sections of this work.

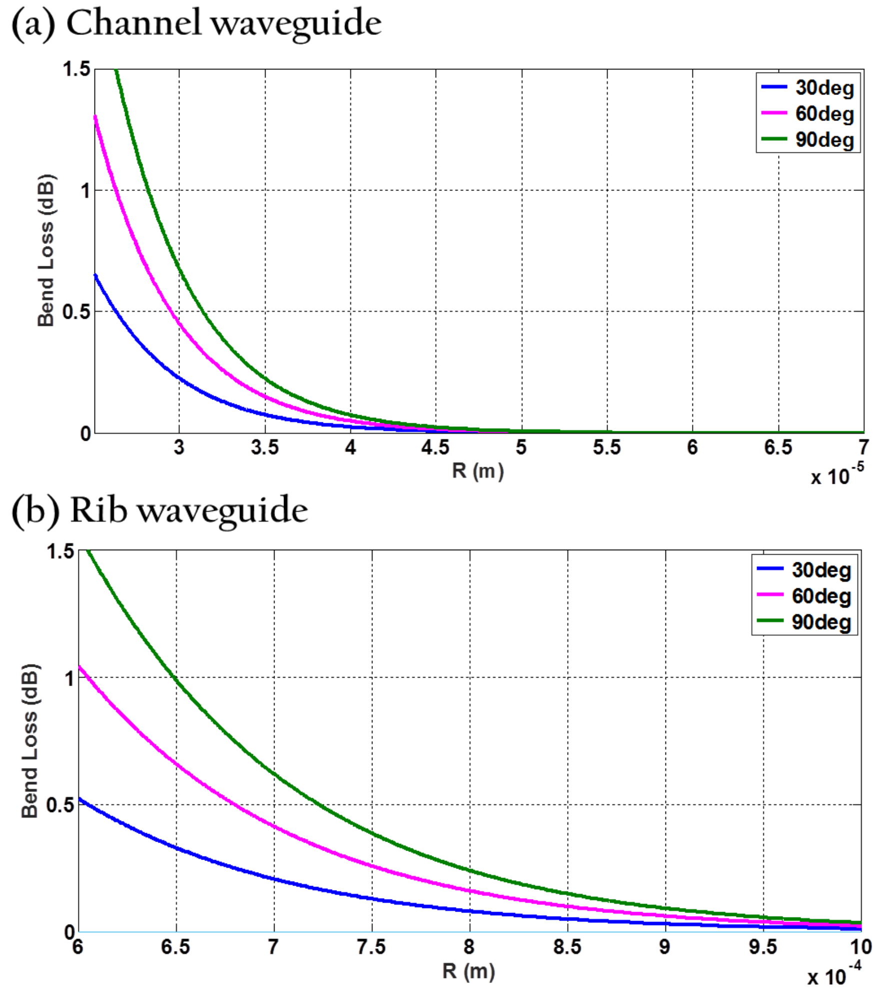

Fig. 2.6 Bend losses calculated for (a) channel and (b) rib $GeTe_4$ waveguides at bend angles of 30°, 60° and 90°

2.3 Calculation of isolation layer thickness for chalcogenide waveguides on Si

In this section, a design of slab waveguide for fabrication of chalcogenide waveguides on Si substrate is proposed. Si is a cheap and convenient flat substrate, fabrication of chalcogenide waveguides on Si can be used for mass-production of integrated waveguides with both optical and electronics components. However, Si has a high RI (>3.4) which is higher than the RI's of most of the chalcogenides (n_{GeTe4} ~ 3.3), so it requires deposition of low index thick cladding layer or isolation layer in between the silicon substrate and the chalcogenide material core to avoid light penetration into Si, as described in Fig. 2.7.

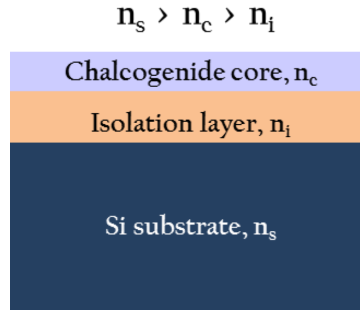

Fig. 2.7 Schematic of fabrication of chalcogenide waveguide on silicon

Comsol numerical modelling was used to calculate the waveguide n_{eff}. The imaginary part or extinction coefficient of the n_{eff} was used to determine propagation loss due to Si substrate as a function of isolation layer thickness on silicon substrate for chalcogenide cores from the following formula:

$$\frac{P_o}{P_{in}}\left(\frac{dB}{cm}\right) = \frac{4.34 * 4\pi k}{\lambda(cm)} \qquad 2.32$$

The acceptable loss due to silicon substrate is taken to be less than 0.1 dB/cm. The following combinations of chalcogenide core and isolation layer were simulated and used experimentally:

1. For a $GeTe_4$ core, thickness of ZnSe isolation layer on Si as well as on oxidised Si substrate was estimated from the propagation losses due to Si at different wavelengths in both MWIR and LWIR. $GeTe_4$ was deposited by RF sputtering and ZnSe was deposited by thermal evaporation for fabrication of waveguides. Si and oxidised Si substrates were bought commercially.
2. For ZnSe core, thickness of SiO_2 on Si was calculated for MWIR only since SiO_2 starts to absorb above λ = 3.7 μm (above which the transmission of 6 mm bulk silica drops to 50% (> 5dB/cm for λ > 3.7 μm [14]) so these samples would not be useful for LWIR.

The waveguides were simulated using slab waveguide which are a good approximation. The model includes real and imaginary parts of refractive indices for Si and SiO_2 taken from literature [139] as shown in Fig 2.8. From Fig. 2.8 (a), the multiphonon edge of Si can be observed to be around ~ 7-8 μm. Beyond this wavelength, the losses in Si starts to increase rapidly. The dispersion curve of silica shown in Fig. 2.8 (b) shows a rapid

increase in the imaginary part of RI beyond 4 µm wavelength region. The dispersion of $GeTe_4$ and ZnSe calculated experimentally in the MIR using IR-Vase ellipsometry were also used in the model.

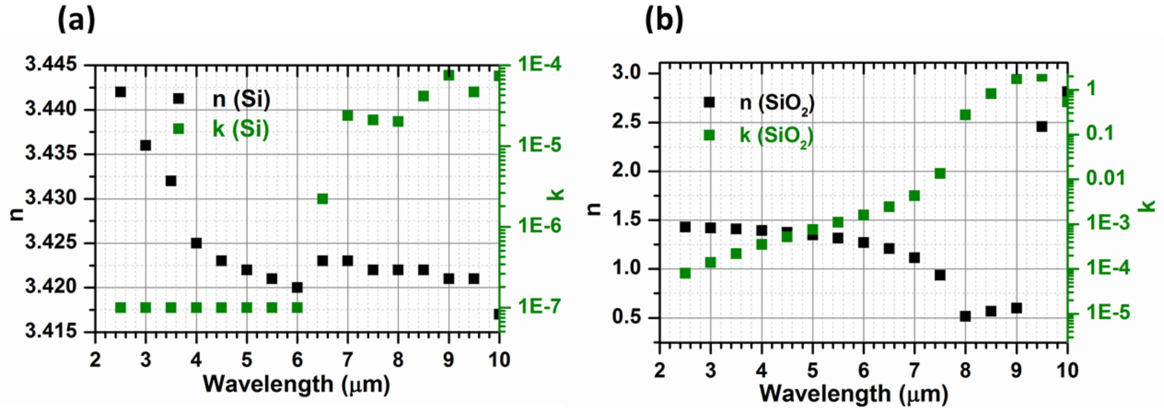

Fig. 2.8 Optical constants of (a) Si and (b) Silica

The procedure for calculating thickness of isolation layer is as follows. For a given core material and an isolation layer, first thickness of the waveguide core is calculated to support a single mode for an asymmetric slab waveguide at a particular wavelength. Then the core thickness is kept fixed and isolation layer thickness is varied with silicon as a substrate underneath and the propagation loss is estimated at each isolation layer thickness. For example, $GeTe_4$ thickness as a core layer on ZnSe substrate was calculated to be in between 0.9-2.1 µm to support a single TE and TM mode with air as cover at λ = 7.5 µm. A 2.0 µm thick $GeTe_4$ core is selected for the purpose of calculations. The dispersion of $GeTe_4$ and ZnSe and the n_{eff} for TE_{00} and TM_{00} for an asymmetric waveguide with air as upper cladding, 2 µm thick $GeTe_4$ core and ZnSe as the substrate are shown in Fig. 2.9.

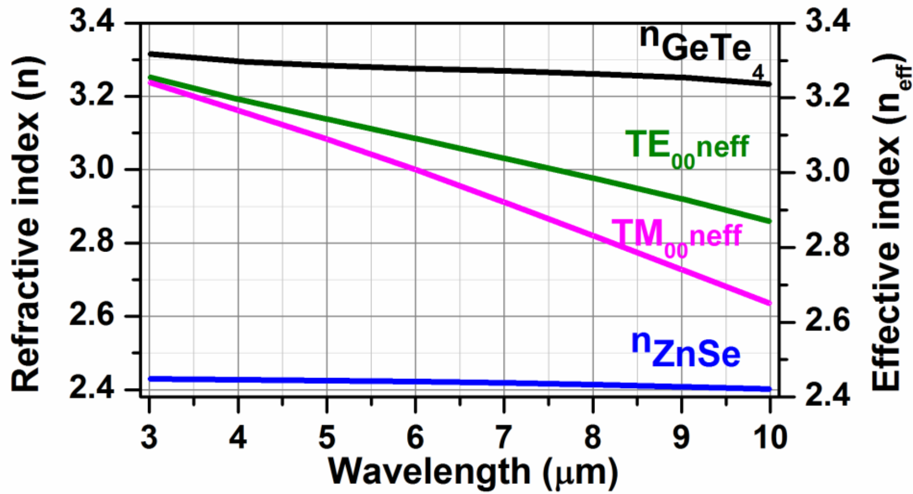

Fig. 2.9 Dispersion profile of $GeTe_4$ and ZnSe and effective indices of $GeTe_4$ waveguide on ZnSe substrate in both the polarisations waveguide on ZnSe substrate

Keeping the $GeTe_4$ thickness fixed as 2.0 μm, ZnSe isolation layer thickness was varied on silicon and oxidised Si substrates (with a 2.5 μm thick silica) to obtain n_{eff} with real (n) and imaginary part (k) for the fundamental TE_{00} and TM_{00} modes.

<u>For $GeTe_4$ waveguides on Si and oxidised Si</u>, a schematic diagram of the waveguide design is shown in Fig 2.10 (a) and (b). Fig 2.10 (c) shows the thickness of ZnSe needed for a propagation loss of less than 0.1 dB/cm in both TE and TM polarisations for a $GeTe_4$ waveguide on Si and oxidised Si substrates for 3-10 μm wavelength region. It can be seen that for an oxidised Si substrate, the thickness of ZnSe layer needed is much lower than for a bare Si substrate for similar losses, at all the wavelengths and in both the polarisations. For example, from Fig. 2.10 (c), the thickness of ZnSe needed up to λ = 8.0 μm with bare Si substrate is ~ 4.0 μm and is ~ 2.5 μm for an oxidised Si substrate. Since Si is transparent up to 8.0 μm wavelengths in MIR, and has the higher refractive index than the core $GeTe_4$, the mode tries to penetrate into Si, hence the thickness of the ZnSe layer needed is more to avoid light penetration into Si. On the other hand, a layer of SiO_2 in between ZnSe layer and Si acts as a shielding layer for the mode to not see the underneath high refractive index Si substrate.

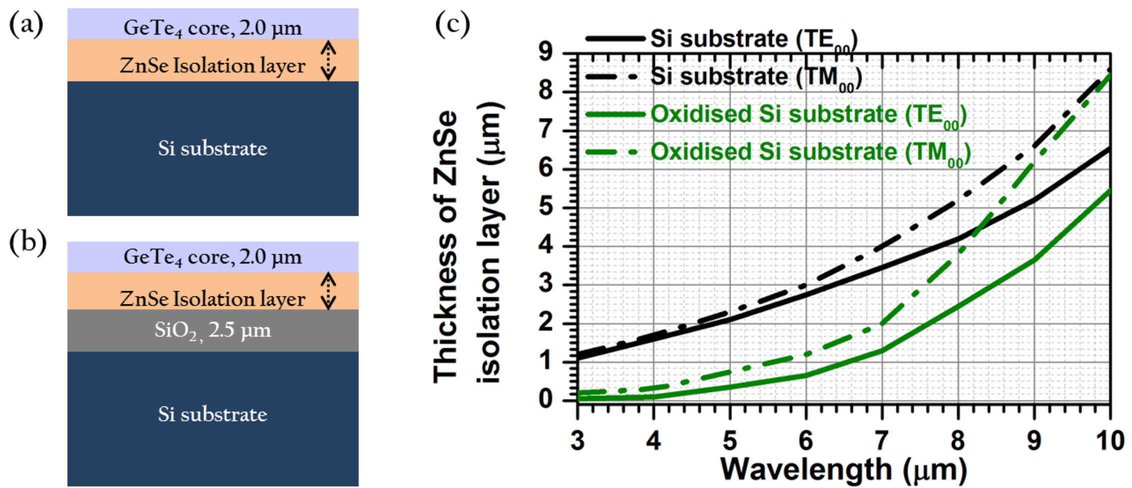

Fig. 2.10 (a) and (b) Schematic of the $GeTe_4$ waveguide with ZnSe isolation layer on Si and oxidised Si respectively, (c) Thickness of ZnSe isolation layer needed to achieve a loss of less than 0.1 dB/cm for both Si and oxidised Si substrates

For ZnSe/oxidised Si waveguides, the calculations are performed for MWIR (λ = 2.5 – 4.0 µm) since silica starts to absorb above 3.7 µm wavelength. The thickness of ZnSe to support single TE and TM modes for silica substrate and air as cover was found to be in between 0.4-1.0 µm at a wavelength of 3.5 µm. A 1.0 µm ZnSe core thickness was chosen for calculations and a schematic of the simulated ZnSe waveguide is shown in Fig. 2.11 (a). In this design, since SiO_2 is deposited on Si, there are two factors to consider, one is tunnelling of light into high RI Si and the other is absorption of light by silica above 3.7 µm wavelengths. On simulating the design of Fig. 2.11(a) at a fixed wavelength of 3.5 µm and varying the thickness of SiO_2 isolation layer in both TE and TM polarisations, the imaginary part of the effective index was obtained. It was used to calculate propagation losses. Propagation losses and n_{eff} as a function of SiO_2 thickness at a fixed wavelength of 3.5 µm is shown in Fig. 2.11 (b). It can be seen that the losses start to decrease as thickness of SiO_2 was increased but after reaching a thickness of 2.5 µm, the losses became constant. Even after increasing SiO_2 thickness to 10.0 µm, the losses remain constant. It is because of thin ZnSe core ~1.0 µm which allows large part of the mode to propagate in the bottom SiO_2 layer. As silica has a larger absorption at these wavelengths compared to Si (refer Fig. 2.8), for 1.0 µm thick ZnSe core losses below 0.1 dB/cm cannot be achieved even by choosing a thicker layer of SiO_2 on Si. However, by choosing a thicker ZnSe core, the mode can be confined well within the waveguide core such that a small percentage of mode

reaches the SiO_2 underneath, and hence reduces the losses due to absorbing SiO_2. A thicker core, however will not be single moded.

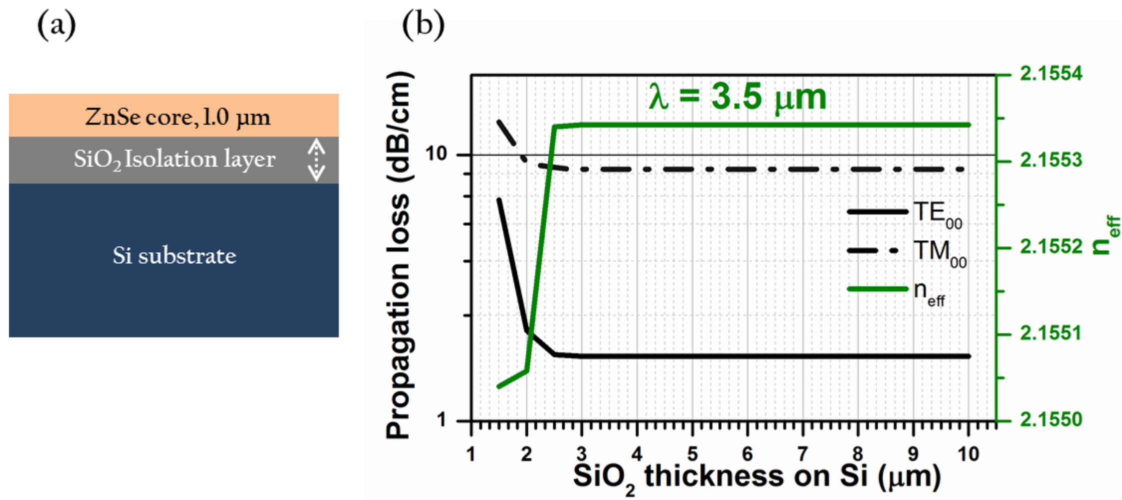

Fig. 2.11 (a) Schematic of the ZnSe waveguide with SiO_2 isolation layer on Si and (b) Propagation losses and n_{eff} of ZnSe waveguide with different SiO_2 thickness on Si

Next, in the model, thickness of SiO_2 isolation layer is fixed as 2.5 μm and losses were calculated with ZnSe core thickness of 1 and 2 μm for λ = 2.5 – 4 μm in TE and TM polarisations as shown in Fig. 2.12. It is seen that with increasing the thickness of ZnSe core, the losses came down by almost an order of magnitude. The percentage of electric field intensity in SiO_2 isolation layer as compared to the whole waveguide with ZnSe core thickness for 1.0 μm was found to be 6.7% whereas for 2.0 μm thick core was found to be 1.4%.

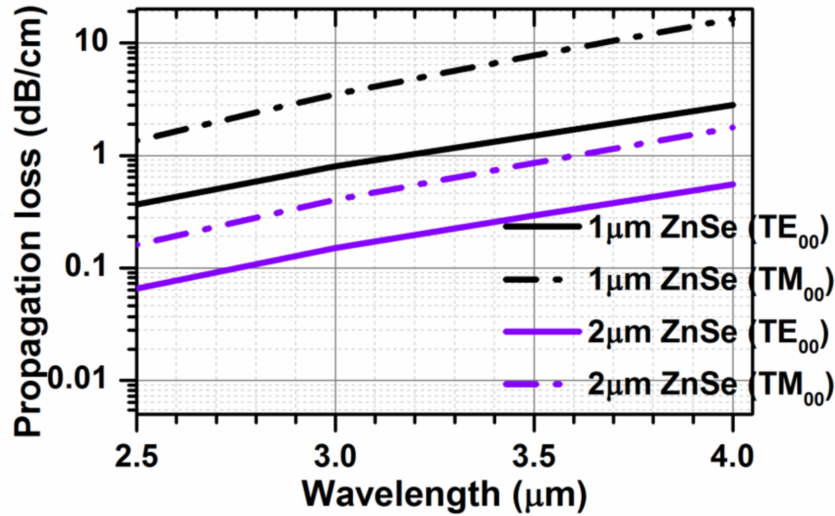

Fig. 2.12 Propagation losses in ZnSe waveguides for ZnSe core thickness of 1 and 2 μm vs. wavelength, when SiO_2 thickness was fixed as 2.5 μm

For a $GeTe_4$ core and Si substrate, the thickness of ZnSe isolation layer chosen for wavelengths up to 8.0 μm is > 4.0 μm and for ZnSe core and Si substrate, the thickness of SiO_2 isolation layer was kept fixed as 2.5 μm.

2.4 Waveguide sensitivity model

A key application of this work is to perform evanescent field based sensing on the waveguides using aqueous analytes. There are two key aspects required to design an optical waveguide for surface sensitive evanescent spectroscopy for label free, specific detection of aqueous biological analytes are the n_{eff} and the mode intensity profile at any cross-section of the waveguide. n_{eff} contains both real (n^r_{eff}) and imaginary (n^i_{eff}) parts given by the following relation:

$$n_{eff} = n^r_{eff} + i\, n^i_{eff} \tag{2.33}$$

In absorption spectroscopy (this work), the imaginary part of n_{eff} is important and represents the absorption. An IR spectrum is measured in transmission-absorption mode where the incoming radiation propagates through the sample and is absorbed at resonant frequencies. The wavelength dependant light reduction is calculated and defined as transmittance (T):

$$T = \frac{I}{I_0} \tag{2.34}$$

where I_0 is the intensity of incident radiation and I is the intensity of radiation after passing through the sample. For absorption spectroscopy, the above equation is usually rearranged in terms of absorbance (A), to give more quantitative information:

$$A = -\log\,(T) \tag{2.35}$$

Absorbance is also defined by the Beer-Lambert law as

$$A = \varepsilon c l \tag{2.36}$$

where ε is the molar absorptivity, c is the concentration and l is the optical path length of light through the sample.

Surface waveguide sensing can be broadly divided into two categories, which involve a bulk or a uniformly distributed analyte extending over a distance well above the evanescent field penetration depth, or thin film (few monolayers) of analyte which is much thinner than the evanescent field penetration depth. The penetration depth, d_p is defined as the distance of evanescent field into the cladding region where the amplitude of electric or magnetic field falls to 1/e of its value at the interface. It is given by the following expression, also defined in chapter 1, section 1.4:

$$d_p = \frac{1}{k_0\sqrt{n_{eff}^2 - n_{cov}^2}} \tag{2.37}$$

The sensitivity for the bulk analyte is defined as the rate of change of effective index of the mode with changes in the refractive index of the analyte in the waveguide cover region (dn_{eff}/dn_{co}). For a thin film analyte, sensitivity is often defined as the change in effective index of the waveguide relative to the variation of thickness *a* of analyte layer with a given refractive index (dn_{eff}/da) [140]. The sensitivities of both bulk and thin film analytes are influenced by the waveguide core thicknesses as the modal power in the waveguide cover carried by the evanescent field interacts with the analyte located on the waveguide

surface leading to changes in n_{eff}. Therefore, the waveguide thickness (cross-sectional geometries in case of 2D waveguides) needs to be optimised for highest sensitivity. A too thick waveguide core will lead to a more confined mode in the centre of waveguide core that will reduce the extent of evanescent field on the waveguide surface and its interaction with the sensing molecules will not be maximised and hence will not lead to highest sensitivity of the analyte. If a waveguide core is too thin, the mode will not be well confined in the core but will spread out in the substrate since in an asymmetrical waveguide, substrate usually has higher refractive index than the analyte medium index. Hence it is important to maximise the proportion of the evanescent field on the analyte side of the waveguide.

Bulk analyte: A numerical model using Comsol is used to optimize the design of a slab waveguide for highest sensitivity for a bulk analyte on the surface of the waveguide, which can be achieved by maximising the fraction of modal power carried in the analyte in the waveguide cover region [141]. The model calculates the change in imaginary part of effective index of the waveguide induced by introducing a bulk aqueous absorbing medium on the surface of the waveguide. The smallest change in absorption due to the analyte a device can detect, the more sensitive it is. Since the purpose of this work is to detect an aqueous analyte on the surface of the waveguide, water is taken as the bulk cover medium as water is the real background for most biological samples including blood, urine, saliva, etc. In the model, the real and imaginary parts of refractive indices of water are included in the model, taken from literature [142] and shown in Fig. 2.13 (a). As an example Isopropanol (IPA) is taken as an analyte which is miscible in water and has distinct absorption peaks in the MIR as shown in Fig. 2.13 (b), the data for optical constants are taken from literature [143]. It can be seen that water also has strong absorption in the MIR which makes the measurement of aqueous analytes difficult. The purpose of our device is not to sense water but for example a very small change introduced by absorbing species dissolved in water. For this purpose, six wavelengths are selected to model the waveguide sensitivity with a combination of water and IPA absorption as shown by red circles in Fig. 2.13 (c) which compares k for both water and IPA. The arrows in the figure represent the IPA peak at that wavelength. The six wavelengths are 2.5 μm, 3.36 μm, 3.7 μm, 7.25 μm, 7.5 μm and 8.85 μm. These

wavelengths are also useful as the laser source used in experiments cover all six wavelengths.

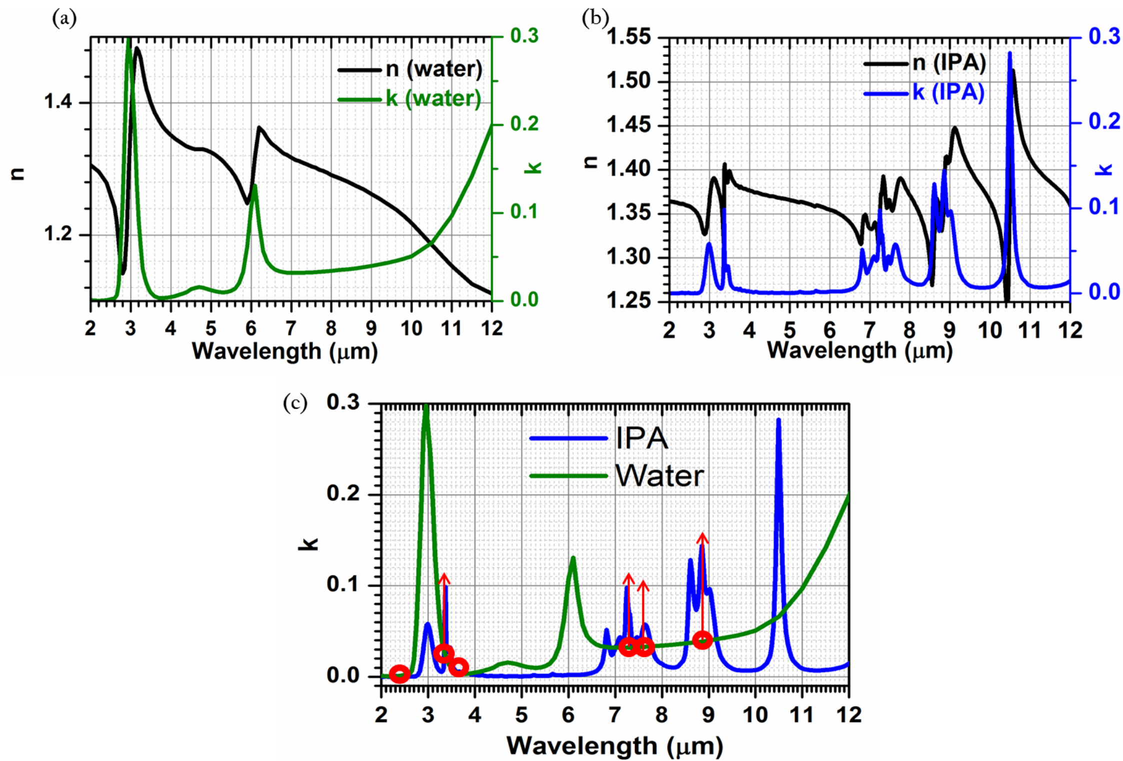

Fig. 2.13 (a) Optical constants of water, (b) IPA and (c) comparison of k for water and IPA (the red circles indicate points on water spectrum showing the corresponding wavelengths at which the calculations are carried out and the arrows indicate the IPA absorption)

In real clinical samples such as paracetamol, the k values are of the order of 10^{-4} - 10^{-5} for the wavelengths range of 5 – 8.5 μm [144]. The k value of water at these wavelengths is of the order of 10^{-2}, and the waveguide should be designed to be sensitive for real samples mixed in water. Therefore, waveguides were simulated to determine optimum designs for sensitivity to bulk absorption changes of the order of 10^{-6}. The waveguide core is taken as $GeTe_4$ and substrate is ZnSe, the dispersion of both of these materials is included in the model as shown in Fig. 2.8 in Section 2.3. A schematic of the simulated waveguide is shown in Fig. 2.14 (a). The thickness of $GeTe_4$ is varied and an optimum thickness was calculated where the waveguide is most sensitive by finding out the fraction of modal average intensity in the cover region (water) given by I_{cov} to the average intensity in the whole $GeTe_4$ slab waveguide including cover, film and the substrate given by I_T. So far, no absorption other than water is introduced in the model. Comsol calculates the average intensity by integrating the poynting vector over the cross-section of the waveguide. The

average intensity in the 1D model used here is defined per unit thickness of the waveguide per unit 1 m thickness in the out of plane direction. Hence the units are W/m^2. Mathematically it is given by:

$$I_{avg} = \frac{|E^2|}{2Z} \qquad 2.38$$

where E is the magnitude of electric field and Z is called the impedance of the wave, which is given by:

$$Z = \sqrt{\frac{\mu_0}{\varepsilon_0 \varepsilon_r}} = \frac{1}{n} Z_0 \qquad 2.39$$

To get the fraction of intensity in the cover region, after obtaining the waveguide fundamental mode in both polarisations, the average intensity is integrated over the cover area and divided by the intensity integrated over the waveguide cover, film and the substrate areas.

The calculations are performed at six different wavelengths for the fundamental mode in both the polarisations and are shown in Fig. 2.14 (b). It can be seen from the graph that the fraction of average power in the cover region depends upon the thickness of the waveguide core, wavelength and polarisation of the incident light. It can be observed that for $GeTe_4$ thickness close to the cut-off thickness, the power in the cover is zero, as the thickness of $GeTe_4$ is increased, it goes through a maximum value, above which, it again starts decreasing as observed in [140, 145-146]. The fraction of power in the cover is more in the TM polarisation, as compared to TE polarisation in agreement with the literature [147]. Fig. 2.14 (c) shows the electric field profile along the vertical direction of the waveguide for both TE and TM polarisations, showing the extent of field in cover, film and substrate of the waveguide.

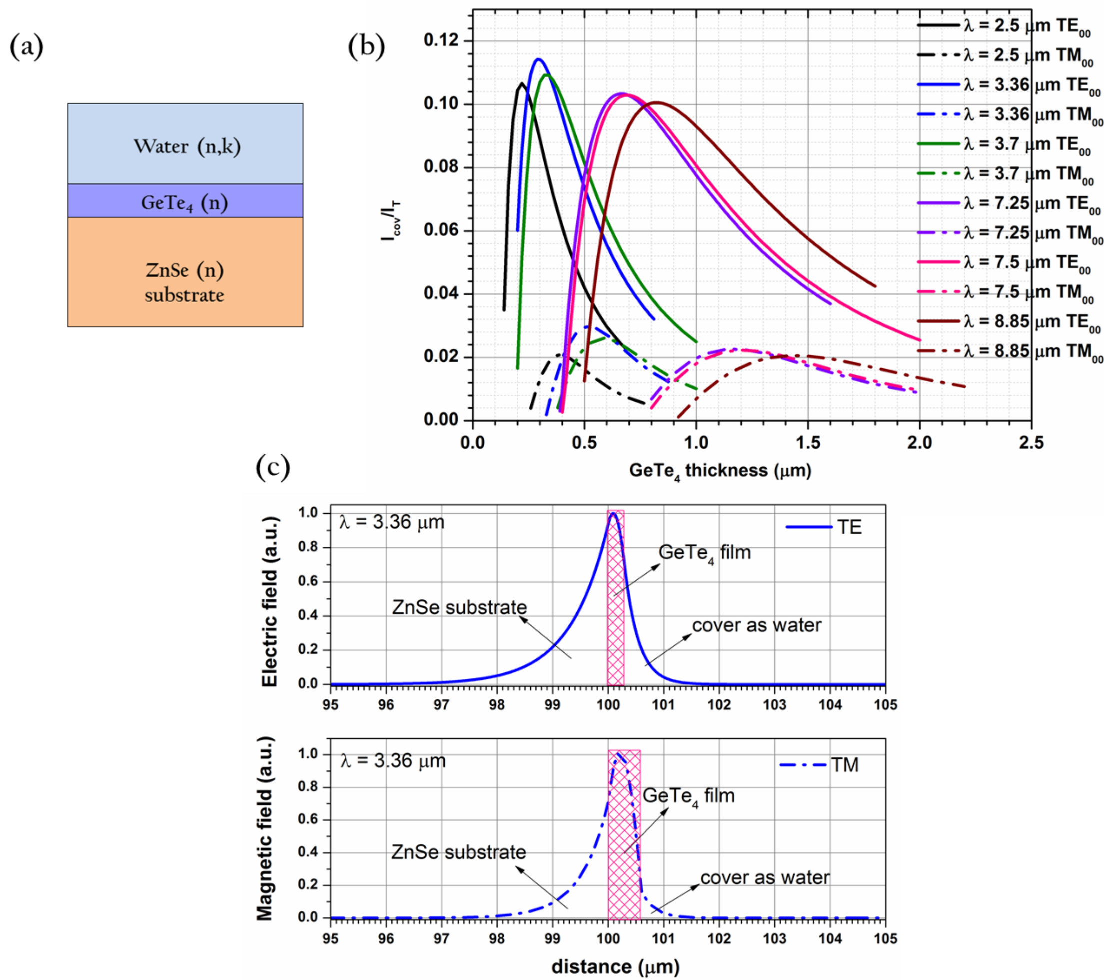

Fig. 2.14 (a) Schematic of the waveguide simulated for the sensitivity model and (b) ratio of modal power in the cover of the waveguide to the total power in the waveguide for TE and TM polarisations at different wavelengths in the MIR and (c) Electric and magnetic field profile of the waveguide at λ = 3.36μm for both TE and TM polarisations in vertical direction.

The thickness where the intensity in the waveguide cover is highest is called the optimised thickness of the waveguide and is shown in Fig. 2.15 as a function of wavelength. It can also be observed that the wavelength dependence of I_{cov}/I_T depends strongly on the real part of refractive index of water and the waveguide n_{eff}. The graph in Fig. 2.15 gives is a good reference for selecting a waveguide design depending on the working wavelengths and polarisations. It can also be seen that thickness of $GeTe_4$ needed is more for TE polarisation than TM, therefore, device working in TM polarisation is advantageous for a thinner or compact device whereas TE polarisation may be chosen for its large waveguide cross-section to improve coupling efficiency because the coupling fibers and lens are generally of the order of microns in the MIR.

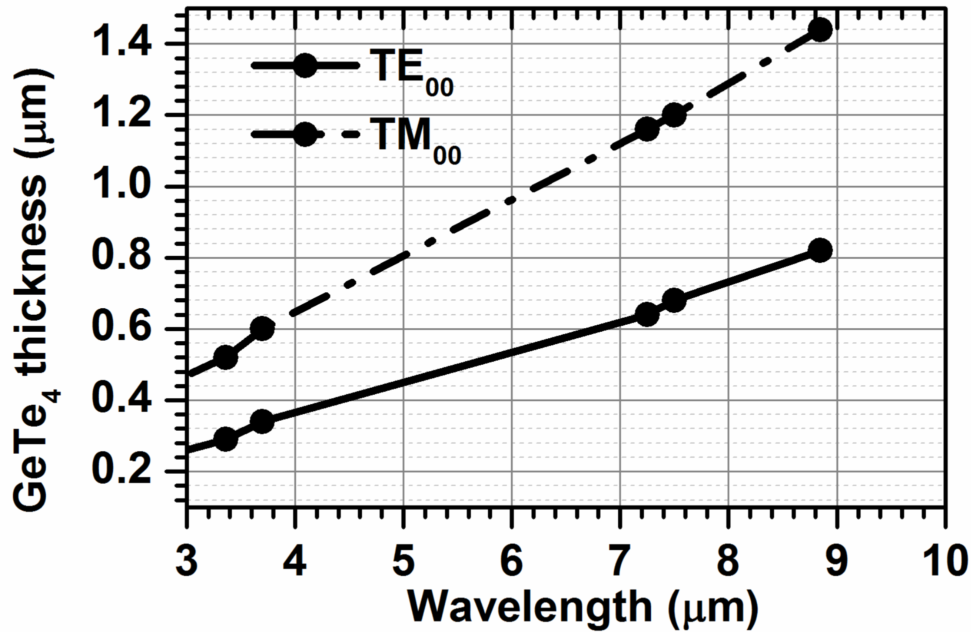

Fig. 2.15 Optimised $GeTe_4$ thickness for maximum sensitivity vs. wavelength

Now, for each wavelength, the thickness of $GeTe_4$ where the waveguide is most sensitive is fixed as obtained in Fig. 2.15 for each polarisation and transmission, $T(k_{water})$ of the waveguide was calculated by using the following formula:

$$T(k_{water}) = e^{\frac{-4\pi n^{i}_{eff} L}{\lambda}} \qquad 2.40$$

where n^{i}_{eff} is the imaginary part of effective index given by Comsol. L is the length of the waveguide.

2.4.1 <u>Waveguide design optimisation for an arbitrary small Δk = 10^{-6} in the cover region</u>

In order to optimise the sensitivity of the waveguide for small changes in absorption, an arbitrary small absorption of $\Delta k = 10^{-6}$ is introduced in the cover region which is water, such that the cover region has $k = k_{water} + 10^{-6}$, and the transmission using equation 2.37 is calculated. A dimensionless quantity, S, which is the sensitivity of the waveguide is defined as the change in transmission of the waveguide due to the introduction of a small absorption in the cover region and is given by the following equation:

$$S = \frac{\delta T}{\delta k} = \frac{T(k_{water}) - T(k_{water} + 10^{-6})}{10^{-6}} \qquad 2.41$$

The sensitivity for the six wavelengths at the optimised $GeTe_4$ thickness is calculated by using equation 2.41 and is plotted in Fig. 2.16 along the length of the waveguide, L. The inset shows a detailed plot for L=0-2 mm. It can be noted that S first increases with the length and after reaching a maximum, it starts to decrease. The length at which S is maximum is called an optimum waveguide length (L_{opt}). In all the wavelengths, S is always higher for TM polarisation.

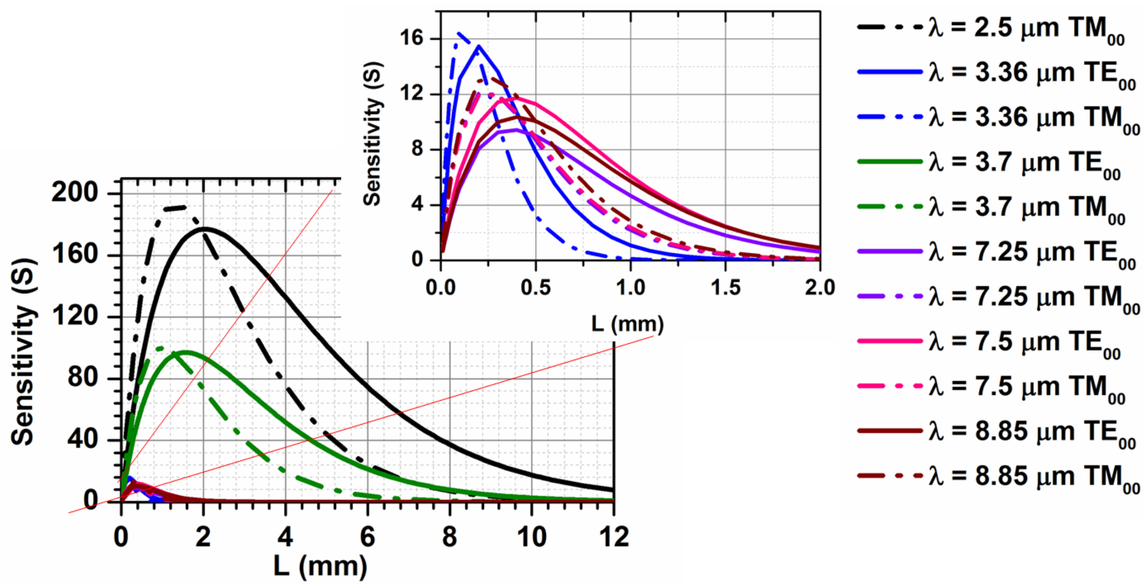

Fig. 2.16 The sensitivity of the waveguide to a small change in absorption in the waveguide cover region, plotted against the length of the waveguide

Both S and L_{opt} are tabulated in Table 2.2. It can be seen from table 2.2 that L_{opt} and S follow the same trend with wavelength. It can also be seen that S depends on wavelength, polarisations as well as k values in the cover region. S follows the exact trend as followed by water absorption spectrum shown in Fig. 2.13 (a) because the absorption added to water is much smaller than water's own absorption. TM polarisation has lower field intensity than TE polarisation, as seen in Fig. 2.14 (b) and (c), however, the sensitivity is greater in the TM polarisation as observed in literature [145, 146].

Table 2.2 Optimised lengths (L_{opt}) and sensitivity (S) for a small absorption change of 10^{-6} in the cover of the $GeTe_4$ waveguide at different wavelengths

λ (μm)	**L_{opt} (mm) TE_{00}**	**S TE_{00}**	**L_{opt} (mm) TM_{00}**	**S TM_{00}**
2.5	2	177	1.3	193
3.36	0.2	15.5	0.1	16.5
3.7	1.6	97	1	100
7.25	0.4	9.5	0.2	0.2
7.5	0.4	11.5	0.3	12
8.85	0.4	10.5	0.3	13

2.4.2 Waveguide design optimisation for k_{IPA} in the cover region

The effect of adding IPA to water in the cover region of the waveguide is discussed in this section. IPA has higher absorption than water at some specific wavelengths (3.36 μm, 7.25 μm, 7.5 μm and 8.85 μm). This corresponds to symmetric and anti-symmetric stretching vibrations of C-H bonds and O-H bonds in IPA.

From literature, we have k of 100% water and 100% IPA, in order to calculate k of a water-IPA mixture (k_m), the following equation is used:

$$k_m = k_{water}c_{water} + k_{IPA}c_{IPA} \quad 2.42$$

where k_{water} and k_{IPA} are imaginary part of water and IPA and c_{water} and c_{IPA} are fractional concentrations of water and IPA respectively. Using equation 2.42, k_m for different concentrations of IPA mixed in water is calculated and is plotted in Fig. 2.17. The concentration 1 on the x-axis of the graph represents 100 % IPA. The slope of each line will give dk/dc.

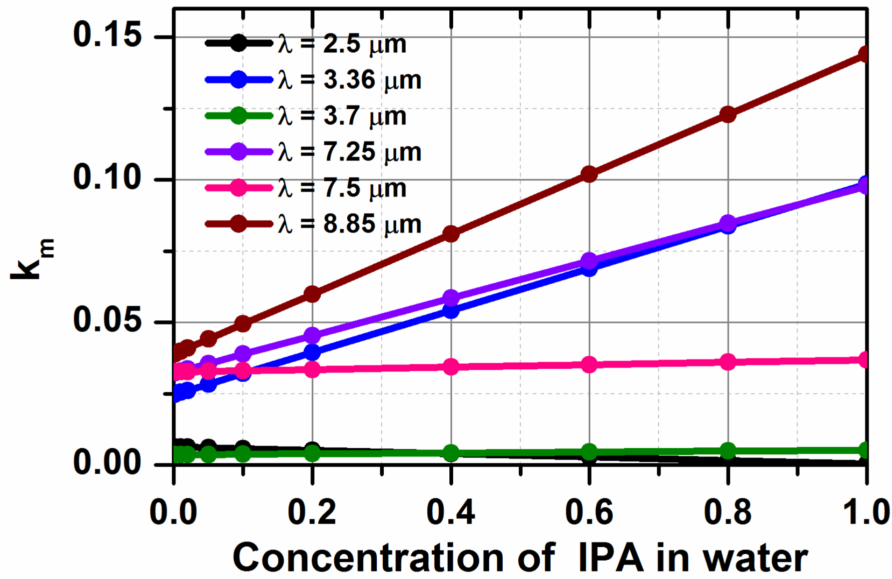

Fig. 2.17 k_m calculated for mixture of water and IPA

In order to calculate change in transmission, the following equation is used:

$$\frac{dT}{dc} = \frac{dT}{dk}\frac{dk}{dc} \qquad 2.43$$

$$\frac{dT}{dc} = S.\frac{dk}{dc} \qquad 2.44$$

Table 2.3 Change in transmittance of IPA in water at various wavelengths

λ (µm)	**dk/dc**	**dT/dc TE₀₀**	**dT/dc TM₀₀**
2.5	-5.9 x 10^{-3}	-1.04	-1.14
3.36	7.37 x 10^{-2}	1.14	1.22
3.7	1.62 x 10^{-3}	1.57 x 10^{-1}	1.62 x 10^{-1}
7.25	6.55 x 10^{-2}	6.22 x 10^{-1}	1.31 x 10^{-2}
7.5	4.24 x 10^{-3}	4.88 x 10^{-2}	5.09 x 10^{-2}
8.85	1.05 x 10^{-1}	1.1	1.37

Change in transmittance is calculated using equation 2.44 by taking values of dk/dc from Fig. 2.17 and the values of S from table 2.2 for both the polarisations. The values of dk/dc and dT/dc in TE and TM polarisations at selected wavelengths are tabulated in Table 2.3. From Table 2.3, the fractional change in the transmission of a $GeTe_4$ waveguide for a small change in concentration of an analyte mixed in water at a particular wavelength is obtained.

Discussion:

From Table 2.2, the sensitivity of the $GeTe_4$ waveguide on ZnSe substrate with a small absorption in water, taken as waveguide cover, is estimated to be 11.5 and the corresponding optimum length is 0.4 mm for TE polarisation. For the same $GeTe_4$ waveguide geometry as simulated with a water cover, at a wavelength of 7.5 μm, if the cover instead is taken as air, the sensitivity of the waveguide with a small absorption in air as waveguide cover is > 12000 and optimum length is 400 mm (when 0.1dB/cm losses were included in the model). The sensitivity and optimum length with air as waveguide cover as compared to water as cover are three orders more. The strong absorption of water due to OH stretching and bending vibrations in the MIR region causes the optimum length to be much shorter and the sensitivity to be much lower. This is a universal problem in direct sensing of aqueous biological samples. The MIR region is dominated by water absorption as shown in Fig. 2.13 (a). Water is the main constituent in most human fluids (blood, urine, saliva), which need to be tested for practical clinical diagnostics and treatment. However, there are a number of ways to remove water from the background of a measurement; 1) by drying the aqueous samples, or 2) combining MIR waveguides with microfluidics and simultaneously extracting the water out and inserting the MIR transparent solvent that has higher affinity towards the analyte into the sample chamber. One such example is lipids, which are hydrophobic, so can be easily extracted from water and mixed in a desired solvent that does not interfere with the MIR light for the absorption spectroscopy.

The model using a bulk media as the waveguide cover is a way to prove the agreement between the theory and the experiment. The real advantage of using waveguides is for studying mono molecular films of the order of 1 nm thick. In transmission through a film

at normal incidence, the absorption due to monolayer will be immeasurably small as the path length is 1 nm. On a waveguide, the overlap between the monolayer and the light can be kept strong over centimetres of lengths, without light being diffracted, and thereby exhibiting a strong absorption.

2.5 Conclusion

Ray and wave model for slab waveguide were discussed to introduce the concept of light guidance and its propagation. Numerical modelling (Comsol simulation) was used to calculate channel and rib geometries as well as bend losses in the waveguide. Comsol was also used to calculate isolation layer thickness between a chalcogenide core and silicon substrate to avoid propagation of light in silicon, due to its higher refractive index than chalcogenide core. A slab waveguide model is described using Comsol, to design a $GeTe_4$ waveguide for maximum sensitivity for a waveguide at any wavelength of choice. The numerical model is useful in comparing theory with the experiment. An investigation of the effect of aqueous media on the waveguide surface on limiting the maximum sensitivity of a waveguide is presented.

CHAPTER 3 MIR Waveguide Fabrication and Characterisation Procedures

This chapter presents the tools and techniques used for deposition and characterization of $GeTe_4$ and ZnSe thin films, procedures followed for fabrication of low loss $GeTe_4$ channel and ZnSe rib waveguides. It also includes the experimental approach used for establishing apparatus for characterisation of the waveguides in both the MWIR and LWIR bands.

Deposition of thin films and fabrication of the waveguides were carried out in class 1000 clean room facilities. Two physical vapour deposition (PVD) techniques are used for the deposition of chalcogenide films: RF sputtering and thermal evaporation. Two different makes and models of RF sputtering systems were used, one each for $GeTe_4$ and ZnSe films. For comparison, both RF sputtering and evaporation were used to determine the best process for ZnSe film deposition. The thickness of the deposited films was measured by profilometry and ellipsometry. Scanning electron microscopy (SEM) was used to observe the surface and cross-section of the deposited films and fabricated waveguides. X-ray diffraction (XRD) was used to study the crystal structure and atomic force microscopy (AFM) was used to measure the roughness of the deposited films. Energy dispersive X-ray spectroscopy (EDX) and X-ray photoelectron spectroscopy (XPS) were used to determine the composition of the films. Optical transmission of the films was determined by Fourier transform infrared (FTIR) spectroscopy. Optical constants were determined by ellipsometry and prism coupling. Contact angle measurement with DI water was also performed for ZnSe films to determine the surface hydrophobicity.

Waveguides were fabricated by photolithography and dry etching as well as by lift off and a step by step procedure is given in this chapter. For characterising the waveguides in the MIR, two set of apparatus were used: one for the MWIR range (2.5-3.7 μm) and the other for the LWIR range (6.4-12 μm), and these are described in the last section of this chapter.

3.1 Tools used for deposition of thin films

In a film deposition process, an approaching atom from the starting material can be either reflected or absorbed on to the surface of the substrate. It depends on the incoming flux of atoms, sticking coefficient and the energy of the substrate surface. For an atom to physically or chemically absorb on the substrate surface, it has to overcome the local energy barriers, since addition of atoms on the surface of substrate creates extra surface enegy. Once the atom sticks to the surface, a tension is created on the surface depends on the atoms stretching or compressing the bonds. Further diffusion of the atoms depends on the overall surface energy and the diffusion rate increases with temperature. In a physical vapour deposition method (sputtering and evaporation), The atoms of the deposition material should have lower chemical potential than a vapour in order to condensate on the substrate. For a stable film, size if the nuclei is critical. 2D smooth films are obtained when the substrate-vapor surface energy is greater than the combined surface energy of the substrate and the vapour (Frank van der Merwe layers) [154].

3.1.1 RF Sputtering

$GeTe_4$ deposition (Oxford Instruments Plasma Technology (OIPT), Plasmalab 400+): In Rf sputtering, a plasma is created between the cathode (target) and the anode at pressures in the mTorr range when a high RF voltage is applied. The magnetic field generated by the magnetron is oriented parallel to the cathode surface such that the secondary electrons emitted from the cathode forms a closed loop close to the target. This increases the confinement of secondary electrons and causes an increase in plasma density close to the surface of the target, producing a high sputtering rate. The OIPT machine used for $GeTe_4$ film deposition contains two 150 mm diameter magnetrons and can accommodate 100 mm diameter substrates. It is a top down system with the magnetrons facing the samples downwards as shown in a schematic diagram in Fig. 3.1. The distance between the target

and substrate is ~ 80 mm. The system operates under high vacuum of ~ 10^{-8} Torr except during deposition when the pressure is increased to 1-30 mTorr [148]. There is a provision for three gases: Argon, nitrogen and oxygen to generate the plasma in an inert or reactive atmosphere. The substrates are transferred into the deposition chamber via a load lock. A commercially bought powder pressed $GeTe_4$ target (Testbourne Ltd.) 150 mm in diameter and 6 mm thick with 99.99 % purity was used. The $GeTe_4$ films were deposited in an inert atmosphere using argon gas. Substrates can be heated up to 300 °C.

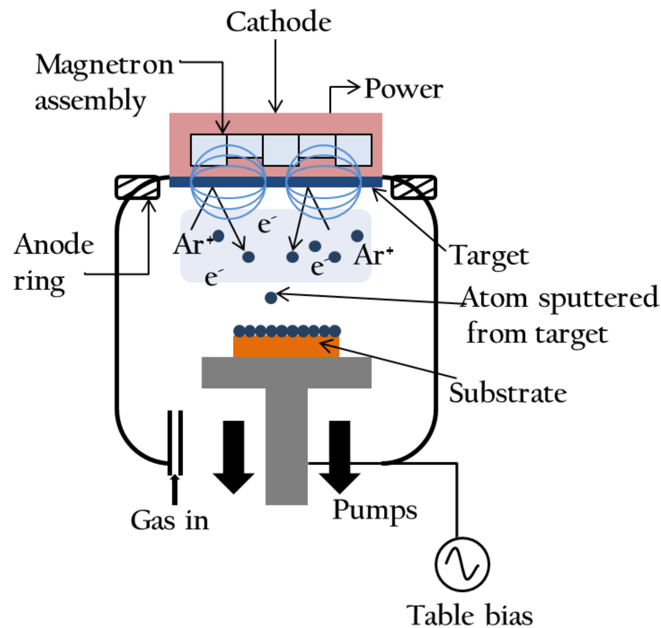

Fig. 3.1 Schematic of the OIPT RF sputtering system

ZnSe deposition (AJA, Orion 8): A different sputtering machine was used for ZnSe deposition because the OIPT machine takes 150 mm diameter of sputtering targets and a CVD grown ZnSe target was not available in that dimension. So a different magnetron sputtering system that can take 75 mm diameter (3 mm thick) targets was used for ZnSe film deposition. A CVD made target is selected for its purity whereas a small target size reduces the cost. The AJA machine contains five sputter sources, three of which have local plasma generated using a DC voltage. The other two sources are connected to RF supplies (max. 600 W). DC is suitable for conducting targets whereas dielectric materials require an RF source. The sputtering system has all the sources placed facing up towards the substrates as shown in a schematic diagram in Fig. 3.2. It can accommodate up to 150 mm diameter substrates. The tool has confocal sputter sources oriented at specific angles to

aim at a common focal point to enable highly uniform films. It gives a much better uniformity (~ 2%) at a working distance of 140 mm over a 100 mm diameter substrate [139], than OIPT machine which gives ~10 % thickness uniformity when substrate rotation was not used. The samples are transferred into the main chamber via a load lock. The samples can be heated up to 300 °C and argon, nitrogen and oxygen can be used for deposition. The ZnSe films were deposited from ZnSe target (Crystran Ltd.) formed by CVD.

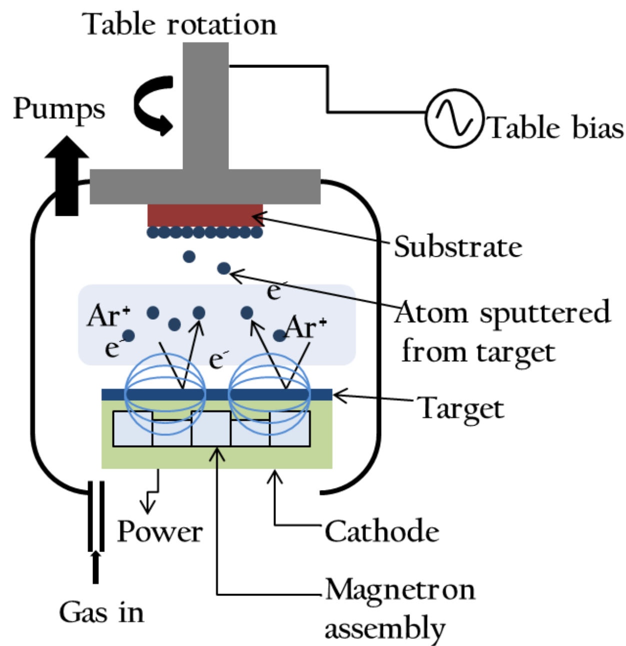

Fig. 3.2 Schematic of the AJA RF sputtering system

3.1.2 Thermal evaporation

Thermal evaporation (BOC Edwards, E306a) is based on electrical resistive heating of the source material where a current is passed through a resistive element such as a filament or boat. The solid material inside the boat is heated under high vacuum to a sufficient temperature to produce a high vapour pressure. The vapour of the evaporated material traverse the chamber and hits the substrates which are mounted inverted at the top of the chamber, hence coating the substrates with the source material [149]. The evaporator used for deposition of ZnSe has four sources that can be used consecutively and an additional source is also available for co-evaporation of two materials concurrently. ZnSe pieces made by CVD were placed in a wide tantalum (Ta) boat and the substrates were mounted

on the platen, facing down towards this evaporation source. A schematic of the evaporation system is shown in Fig. 3.3 (a) a photograph of the evaporation chamber while depositing ZnSe is shown in Fig. 3.3 (b). A Ta boat used is also shown in Fig. 3.3 (c). The system was operated at a base pressure of 5 x 10^{-6} mbar. The substrates were screwed on a substrate holder platen which was heated at 250 °C and rotated to maintain the thickness uniformity of the films. A crystal monitor was used to monitor the thickness of the films. The evaporation chamber was filled with liquid nitrogen from time to time to maintain high vacuum inside the chamber.

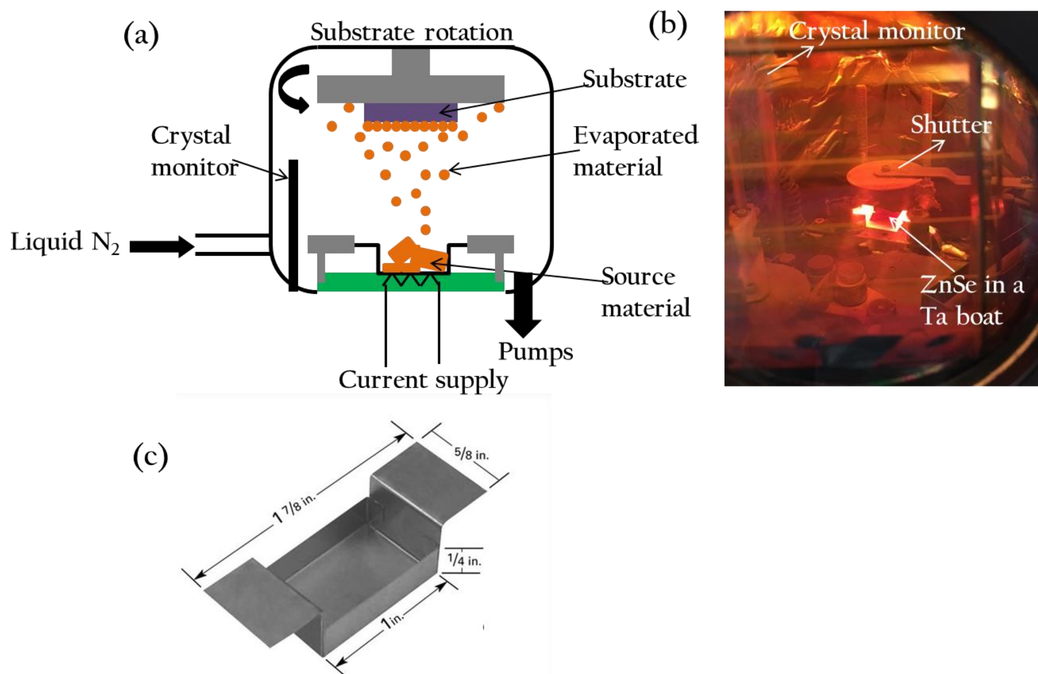

Fig. 3.3 (a) Schematic of a thermal evaporator system, (b) a photograph of the chamber while depositing ZnSe films and (c) a Ta boat used for evaporation

3.2 Tools used for film characterisation

3.2.1 Film Thickness

Stylus Profiler (KLA Tencor, P16+): A 2 μm radius stylus tip was used to measure the thickness of the deposited films. A step is created by covering a small portion, usually two diametrically opposite corners of a substrate with kapton tape while depositing the films. A maximum height of ~ 300 μm can be measured with a vertical resolution of nearer 1 nm using this model.

UV-Vis-NIR Ellipsometry (Woollam Co. Inc., M-2000): This tool can be used to measure the thickness as well as optical constants of the films. In this work, it is primarily used to measure the thickness of the deposited films and as well as after etching. It covers the wavelengths from 193nm to 1690nm, and a range of incident angles 45°-90°. It has a beam diameter of ~ 3 mm, which can be reduced to ~ 300 μm with the help of focussing probes provided by the manufacturer. An inbuilt software package called Complete Ease was used to analyse the data, where a dispersion model is created to best fit the experimental data.

3.2.2 Surface morphology by microscope and SEM

Microscope (Nikon, LV100D): The preliminary inspection of the substrates after cleaning as well as deposited films was performed using a microscope in both bright field and dark field configurations with a maximum magnification of 1000x.

SEM (Carl Zeiss, EVO 50): An SEM system using tungsten filament, operating under an accelerating voltage between 0.2-30 kV and argon and nitrogen purge gases were used to observe the surface and morphology of the deposited films as well as to optimise the photolithography procedure. A resolution of 3 nm can be obtained at 30 kV.

FESEM (Jeol, JSM-7500F): A field emission SEM utilizes a highly focussed electron beam which provides better resolution that filament based SEM. An FESEM operating between accelerating voltages 0.1-30 kV under high vacuum was used to obtain top surface and cross-section images of the deposited films as well as channel and rib waveguides. It has a surface resolution of 1.0 nm at 15 kV.

3.2.3 Crystallinity by XRD

XRD (Rigaku, Smartlab) is used to determine the crystallinity or phase of the deposited film. An XRD system with a monochromatic Cu kα target in 2 theta geometry was used where only the detector moves and the source remain at a fixed angle. The sample was placed in the XRD chamber, where X-rays are incident on the sample at a grazing angle of 1° and are detected by a detector in the range of 10°-80°. The scattering of X-rays from the atoms of the film at different planes produces a diffraction pattern given by a plot of X-ray

intensity as a function of angles with respect to incident beam. It gives the information about the crystallanity and phases of the sample (film or substrate).

3.2.4 Surface roughness by AFM

AFM (Bruker, Veeco Nanoscope V) in tapping mode was used to measure the surface roughness of the deposited films and the substrate. Here a Si_3N_4 cantilever with a sharp tip (~8 nm radius) is used to measure the atomic forces between the sample and the tip, without contacting the sample surface. This way, surface damage of the sample is avoided. This high resolution scanning probe microscopy system can produce very stable and low noise image of 0.3 Å in vertical dimension. The lateral resolution depends on the size and shape of the AFM tip, the detectors sensitivity and scan size and number of sampling points. An ~ 8nm diameter tip was used for the measurements.

3.2.5 Composition by EDX and XPS

EDX (Carl Zeiss, EVO 50): EDX is a compositional analysis tool used in conjunction with SEM. An electron beam is bombarded on to the sample and electrons are ejected from the atoms of the samples. The electrons vacancies are filled by higher energy electrons and hence X-rays are emitted between the two electron states from the sample. Since X-ray energy is characteristic of the element from which it was emitted, this gives the elemental composition of the analysed volume of the sample.

XPS (Fisher Thermoscientific, Thetaprobe): XPS is a surface sensitive technique that is used to determine the elemental composition of the outermost atomic layers of a solid material. It can also be used to determine chemical and electronic state of the elements present in a material. It acquires information of the top few nm of the surface of a flat sample. Soft X-Ray (wavelength 0.1-1nm) photoelectrons of low energy irradiated from Al Kα target (1486.6eV) strike the surface of the sample and ionize the surface by knocking out the electrons from different energy levels of the atoms [150-152]. As low energy X-rays are used so it cannot penetrate deeper into the surface, unlike in SEM, where X-Ray of high energy are used to penetrate deeper into the sample. Electrons that escaped from the first few layers are detected and the deeper ejected electrons are either recaptured in the solid or loose energy during travel to the surface, hence they contribute in the spectrum background [152]. Every element has a fingerprint spectrum for binding energy, so they

can be easily identified from other elements present on the same surface. When a photon of known energy hν knocks an electron out of the shell of an atom, these electrons are measured by the detector as a function of their kinetic energy; hence their binding energy can be calculated from the following equation:

$E [A] + h\nu = E [A^+] + E [e^-]$

$E [e^-] = h\nu - (E [A^+] - E [A])$

$K.E. = h\nu - B.E.$

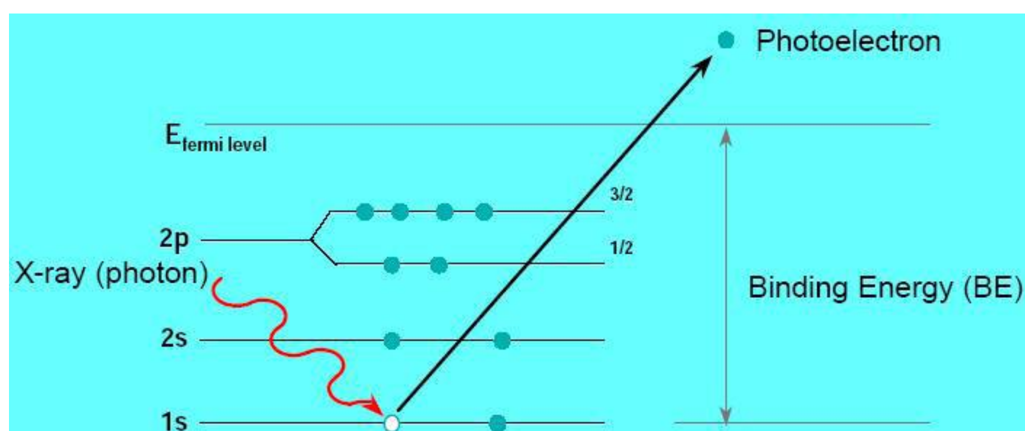

Fig.3.4 Schematic of principle of photoelectron emission in an XPS (Image taken from [152])

A schematic of the principle of photoelectron emission in an XPS is shown in Fig. 3.4. Electrons from all orbitals of an atom with BE < X-ray energy can be excited [3]. On plotting the intensity or electrons counts to B.E/K.E., the elements present in a given sample can be found. The position of the peaks tells the information about the element present whereas the peak intensities show the amount of the element present. The shape of the peak and the shifts in peak gives the information about chemical state of the element.

In this work, XPS with a monochromatic aluminium (Al) Kα X-ray source (hν = 1486.6 eV) operating at a base pressure of 2 x 10^{-9} mbar was used to determine the composition of films. The X-ray source was operated at 6.7 mA emission current and 15 kV anode bias with a spot size of 400 µm and photoelectrons were collected over a cone of ±30° with the lens mounted at 40° in respect to the sample surface. Ar ions with a current of 1 µA and 3 kV energy were used to etch the sample surface for depth profiling. Depth profiling

enables acquisition of XPS spectra from a fresh surface exposed on etching the film surface with Ar ions at every fixed interval. A flood gun was also used to compensate for charge build up in the sample. C 1s core level at 284.8 eV was used as reference for correcting the charge shift. The data was analysed using the in-built Avantage software package.

3.2.6 Optical transmission by FTIR

An FTIR spectrometer (Agilent Technologies, Cary 670) in normal incidence was used to measure the transmission of thin films. The instrument consists of a broadband globar infrared source, several mirrors, a potassium bromide (KBr) beam splitter and a deutrated triglycine sulphate (DTGS) detector. The spectrometer is based on an interferometer where an infrared beam is split into two parts after passing through the beam splitter (BS) and travel in two directions at right angles, one beam to a stationary mirror and back to the BS and the other beam to a moving mirror and back to the BS. When the two beams recombine at the BS, a constructive or destructive interference is created according to the path difference between the two beams. An interferogram is generated giving optical intensity versus optical path difference. A Fourier transform of the interferogram gives the FTIR spectrum. A 4 cm^{-1} resolution and a total of 64 averaged scans were used to reduce noise in measured data.

3.2.7 Optical constants by IR-VASE Ellipsometry and Prism coupler

IR-VASE Ellipsometry (Woollam Co. Inc.): In order to determine the optical constants of $GeTe_4$ films and ZnSe substrates in the MIR, IR-VASE variable angle spectroscopic ellipsometer for the infrared was used. This collects data from 2 to 30 μm with angle of incidence ranging from 30 - 90°. The backside of the sample was roughened prior to the measurement to avoid spurious reflections. Data were collected from the centre of the sample and optical constants were modelled using a generalized Gaussian oscillator layer modelling the thickness and roughness of the film, as well as the optical constants [153].

Prism coupler (Metricon™): The refractive indices of the deposited film, the respective effective indices of the propagating modes and the propagation loss for TE and TM polarizations were determined by an automatic prism-coupler operating at 1550 nm wavelength. The Metricon system consists of a controlled rotation stage attached to a

motor for an angular resolution of 0.45°, a photodiode placed at the output facet of the prism measures the relative intensity of light that is not coupled into the guiding layer against the incident angle. Dedicated software records and recognise the minimum intensity associated with coupling and determines the modal effective indices of the guiding layer. The propagation loss due to scattering was also determined using Metricon where once the guided mode is excited, an associated weak streak of light scattering out of the waveguide plane was recorded. A fibre is then scanned along the direction of propagation of streak to calculate the decay rate of the propagating mode with respect to the distance which is used to determine the loss of the guiding layer. The measurement assumes the direction of scattering is out of plane of the guiding layer. The system is sufficiently sensitive to measure losses from 1-30 dB/cm with an error of ±0.1 dB/cm.

3.2.8 Surface wettability by contact angle measurement

Contact angle (Kruss DSA 10) measurements were performed to inform future work on surface modification for binding of biological monolayers, the hydrophobicity of the surfaces were measured using the surface wettability test. The test was carried out by static contact angle measurement with deionized (DI) water on the deposited films and the angle between the water drop and the underneath surface was calculated to define hydrophilic or hydrophobic nature of the surface in contact. A hydrophilic surface has strong affinity to water therefore wets a large area of surface by maximizing the contact and by definition has the contact angle less than 90°. Hydrophobic surface repels water and has a contact angle greater than 90°.

3.3 2D waveguide fabrication procedures and tools used

2D channel and rib waveguides were fabricated using etching and lift-off techniques. Etching is a subtractive method whereas lift-off is an additive method. For etching, a positive photoresist (S1813) was used. Lift-off was carried out by both positive (S1813 and LOR 30B) and negative photoresists (AZ2070) explained in detail in sections 3.3.2 and 3.3.3. Three different masks were used: 1) identical bands of straight opaque stripes of width ranging from 1 to 10 μm with centre to centre distance 100 μm and 20-70 μm thick stripes separating each bands, 2) straight opaque stripes with width ranging from 1 to 5 μm and distance between adjacent waveguides was varying from 50 μm to 2 mm and 3) a

mask with various features including straight channels from 3 to 30 μm wide with centre to centre distance of 400 μm, 90° bends and splitters including gratings at the output end. The following tools were used for photolithography and etching:

Mask aligner (Suss Microtec, MA-6): An i-line and h-line mask aligner operating at 365 nm and 405 nm respectively was used to transfer patterns. It can accommodate up to 100 mm diameter substrates. A 5″ mask with a 350W Hg lamp emitting at intensity of 16-18 mW/cm^2 was used. The best resolution of 800 nm can be obtained using this system.

Reactive ion etching (Oxford Instruments Plasma Technology, Plasmalab RIE80+): RIE is a dry etching process based on parallel plate induced etching. The substrate is placed on a graphite or quartz substrate holder. It is connected to the following gases; CHF_3, O_2, Ar and SF_6. The gases are introduced in the chamber via a gas-inlet in the top electrode (anode) and the substrate holder table acts as the lower electrode (cathode). Plasma is generated by applying an RF voltage between the two electrodes. The neutral atoms of the plasma and the negatively charged electrode results in a potential difference called as self-bias voltage, which drives the positively charged ions in plasma towards the negatively charged substrate table. Etching is achieved by both physical and chemical process.

Inductively coupled plasma (ICP) etching (Oxford Instruments Plasma Technology, Plasmalab 100ICP380): ICP is an RIE process which includes an RF source where excitation is performed inductively by a coil wrapped around an RIE plasma discharge region, which produces a change in magnetic field. The change in magnetic field induces an electric field which circulates the plasma in the chamber. The electrons from plasma bombarding the chamber walls create a static voltage, which is different from the self-bias voltage. The dual plasma system offers flexibility in altering plasma density and energy independently [154, 155]. The substrate is transferred into the etching chamber via a load lock where it is placed on a helium cooled table. It is connected to the following gases; C_4H_8, O_2, Ar, Cl_2, HBr, SF_6.

Ion beam system (Oxford Instruments Plasma Technology, Ionfab 300+): 150 mm collimated argon ion beam was used to etch the ZnSe waveguides. The sample holder can be rotated from 0°-90°, in order to optimise the etching conditions to obtain vertical walls.

There is a trade-off between using lower angles to get the vertical walls as it causes material re-deposition. The system was optimised for etching at an angle of 45°.

3.3.1 Photolithography and dry etching

Photolithography followed by etching was carried out to pattern the film into rib/channel structures with the aim of achieving low surface roughness and vertical sidewalls. A schematic of the entire process is shown in Fig. 3.5 and the process steps are explained below.

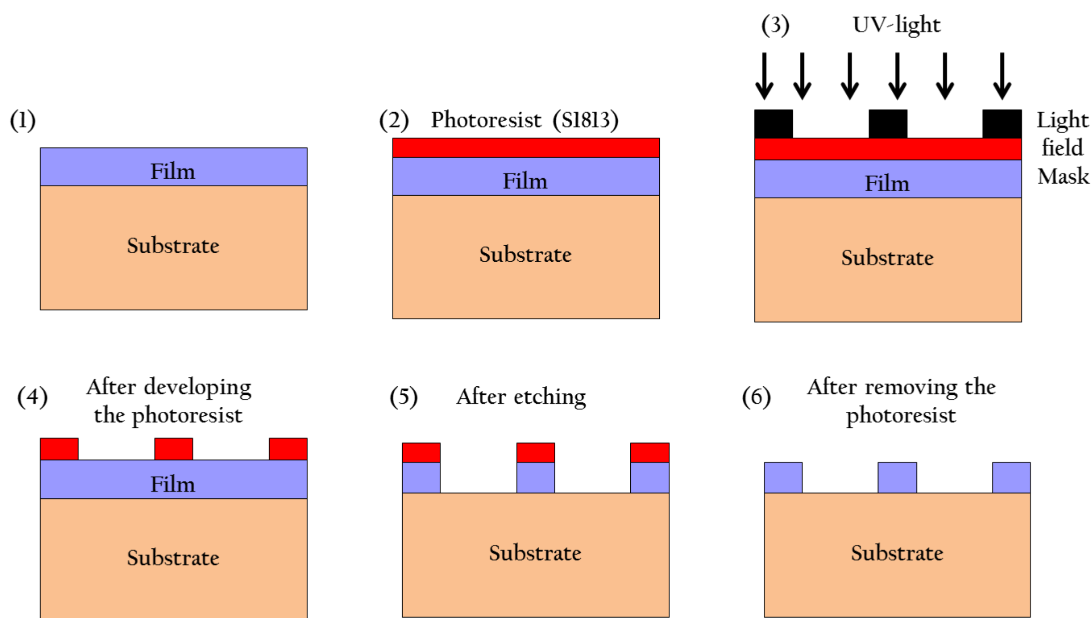

Fig. 3.5 Schematic of the standard photolithography and dry etching process steps

The fabrication process steps shown in Fig 3.5 are explained below:

1. A film (waveguide core) was deposited on a cleaned substrate.
2. On the clean surface of the film, a positive photoresist (Shipley, S18 series) was spun using resist spinner. After spinning the resist, the sample was soft baked at 90°C on a hot plate for one minute.
3. A light-field photolithographic mask with opaque stripe patterns of various widths (1-70 μm) is used to transfer the patterns on to the sample. The sample is exposed to UV-light coming from a mercury lamp.
4. The sample is then developed in a developer solution (MF-319) with continuous stirring. On developing the photoresist, the exposed regions are dissolved in the

developer solution while unexposed regions stayed on the film. The sample is washed with DI water and dried with compressed N_2 and then hard baked on a hot plate for two minutes at 110°C.

5. The sample is then etched using ICP or Ar ion beam systems to etch away the exposed film leaving behind the partially or fully etched stripes.
6. The left over photoresist is then washed away in acetone.

3.3.2 Photolithography and Lift-off

The lift-off technique is used to avoid etching as some materials are difficult to etch. This process requires a sacrificial layer of photoresist to be deposited and patterned by an inverse mask pattern to create the undercut photoresist layer. The film (waveguide core) is deposited over the undercut photoresist layer such that the opening of undercut defines the width of the final waveguide. The photoresist is then washed off, leaving behind the desired film patterns. Here any material that is deposited on the sacrificial photoresist layer will be washed away (or lifted off) and the material deposited on the substrate directly will remain [156]. This method also prevents any contact of the film with water which can lead to oxide contamination in the chalcogenide film and hence may lead to losses in the final device. Lift-off was carried out by two different approaches differing in the type of resist used and both the approaches are discussed in detail below.

3.3.2A Dual layer process with lift-off resist (LOR 30B) and a positive photoresist (S1813): An LOR is a polymer which is not photo-sensitive to UV light but is affected by a developer solution. It is used where thicker layers of films or core materials are needed that cannot be achieved by photoresist alone. It is used as a bottom layer below a photoresist. The process steps of this technique are shown schematically in Fig. 3.6 and are as follows:

A lift-off resist (LOR 30B) is spun on a cleaned substrate using a resist spinner. The process was optimised to achieve an 8μm thick LOR layer by spinning dual layer of LOR 30B [157].

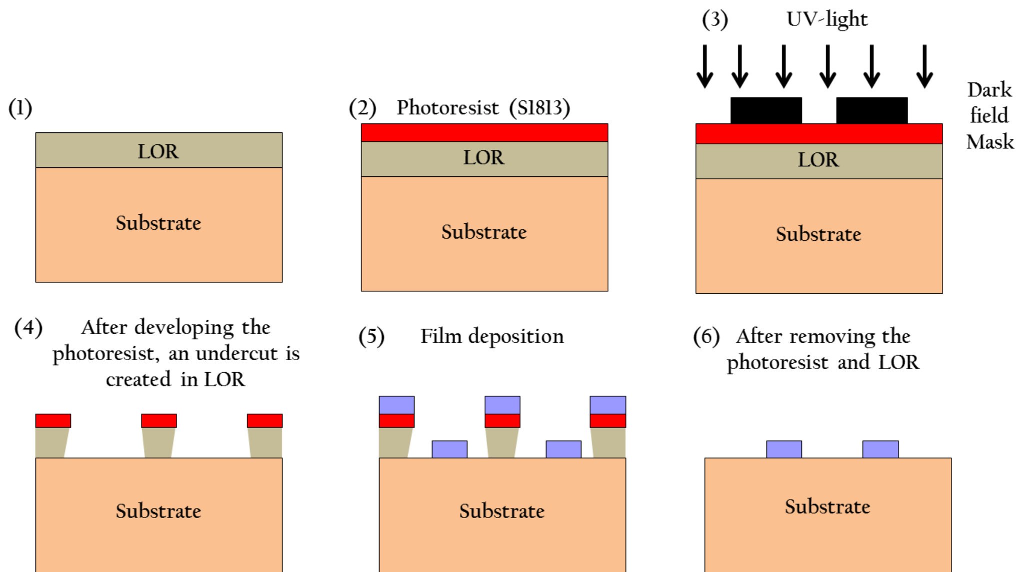

Fig. 3.6 Schematic of the Lift-off process using photolithography and LOR photoresist

1. A positive photoresist S1813 (Shipley) was then spun over the lift off resist to define the pattern using UV light. After spinning the resist it is soft-baked on a hot plate at 90°C for 1 minute.
2. The sample was exposed to UV light using a dark-field photolithographic mask having transparent straight stripes of varying thickness and separation. The dark-field mask used had similar straight stripes (from 1-70 μm wide) as that of light-field mask used in the conventional photolithography but a reverse pattern is obtained as compared to the pattern obtained after developing a light-field mask pattern. An exposure time of 8 sec was optimised for an 8 μm thick LOR layer with a 1.3 μm photoresist layer on it.
3. The sample is then developed in a developing solution (MF 319) to create the undercut by removing the exposed resist to open the channels. Different developing time were tried to open the channels fully such that the developer reaches the surface of the substrate.
4. The $GeTe_4$ film is then deposited on the sample by RF sputtering.
5. LOR and photoresist is then stripped off in a resist stripper solution (SVC 14) to obtain the desired features.
6. Exposure and developing time vary with thickness of the resist and minimum feature size required. There is no hard bake required for the resist after development as etching is not performed.

3.3.2B Single layer process with a negative photoresist (AZ2070): While optimizing lift-off procedure with the LOR, another photoresist was found to be useful for lift-off. It is a negative resist AZ2070. It reduces the processing steps as it does not require any LOR underlayer. AZ2070 can be deposited over a range of thicknesses (2-30 μm) and is also sensitive to UV-light. A negative resist is the one which will cross-link all the exposed regions and hence these regions are not attacked by the developer. Hence a light-field mask is used to create straight channels. The process steps are as follows and a schematic is shown in Fig. 3.7:

1. A negative photo-resist (AZ2070) is spun on a cleaned substrate using a resist spinner optimised for a thickness of ~6-8μm. The sample is then baked on a hot plate at 110°C for 90 sec.
2. The sample is then exposed to UV light. A light-field photomask having straight stripes of varying thickness and separation was used to transfer the pattern on the substrate.
3. The sample is then baked again at 110°C for 90 sec before developing; this is called post exposure bake (PEB). The exposure dose determines the part of the resist cross-linked after the PEB.
4. The sample is then developed in a developing solution (AZ716) to create an undercut and the opening of the channels.
5. The waveguide core is then deposited on the sample.
6. The photoresist is then stripped off in acetone to obtain the desired features.

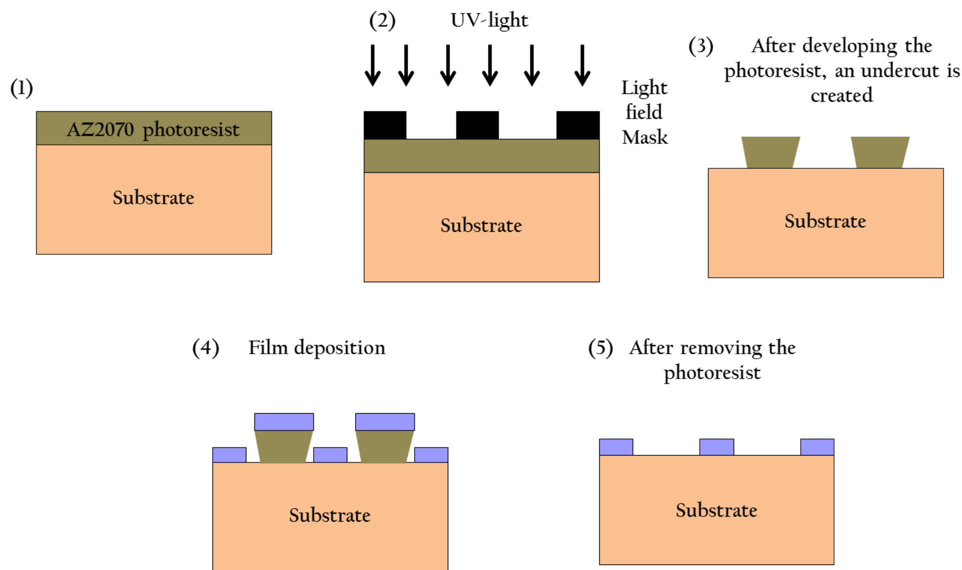

Fig. 3.7 Schematic of the Lift-off process using photolithography and AZ2070 photoresist

3.4 Waveguide end-facet preparation

It is important to have smooth optical quality end facets for coupling of light into the waveguide. Rough end facets lead to scattering of light off the edges of the waveguides and leads to high coupling loss. Conventional polishing was tried for end facet polishing of chalcogenide waveguides, but due to the soft and brittle nature of these materials, it was not successful. Therefore, an optimized ductile dicing procedure [158, 159] using a nickel bonded blade (Disco ZH05-SD4800-N1-50 GG, width of 50–60 μm and 4800 grit), with a depth of cut ~260 μm, a rotational speed of 20 krpm and a translation speed of 0.1 mm/s was used to machine the $GeTe_4$ waveguide on bulk ZnSe end facets.

Waveguides fabricated on Si substrates were cleaved along the crystal planes of Si.

3.5 Waveguide characterization in the MIR

In order to characterise the waveguides for waveguiding, propagation losses and mode profiles in the MIR region, two sets of experimental apparatus were used. One for the MWIR and the other for the LWIR regions of the MIR. The generic experimental set-up is shown in Fig. 3.8 and is explained below.

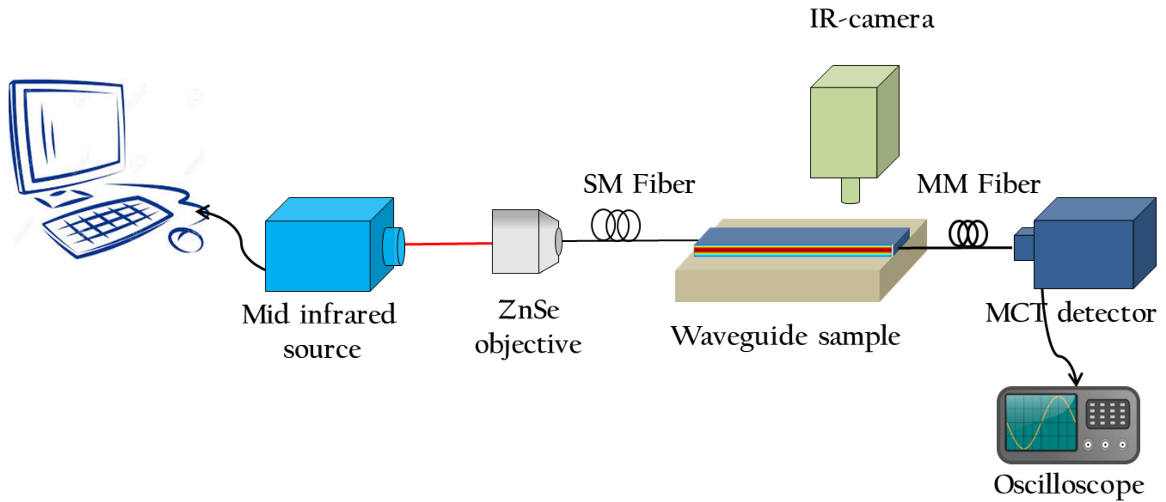

Fig. 3.8 Schematic of the experimental set-up used for characterisation of waveguides in the MIR

3.5.1 MWIR experimental apparatus

3.5.1A Light source (M-Squared Lasers, Firefly-IR): An optical parametric oscillator (OPO) based pulsed, tunable light source operating at wavelengths between 2.5 μm and 3.7 μm with an average power of 100 mW was used to characterise waveguides in MWIR. The OPO optical output power spectrum is shown in Fig. 3.9. The three scans projected on each other shows the repeatability of the laser output with wavelength. The laser has high repetition rate of 150 kHz with pulse duration of ~ 10 ns and the line width is < 10 cm^{-1} (at λ = 3.0 μm). The beam diameter is 2 mm [160].

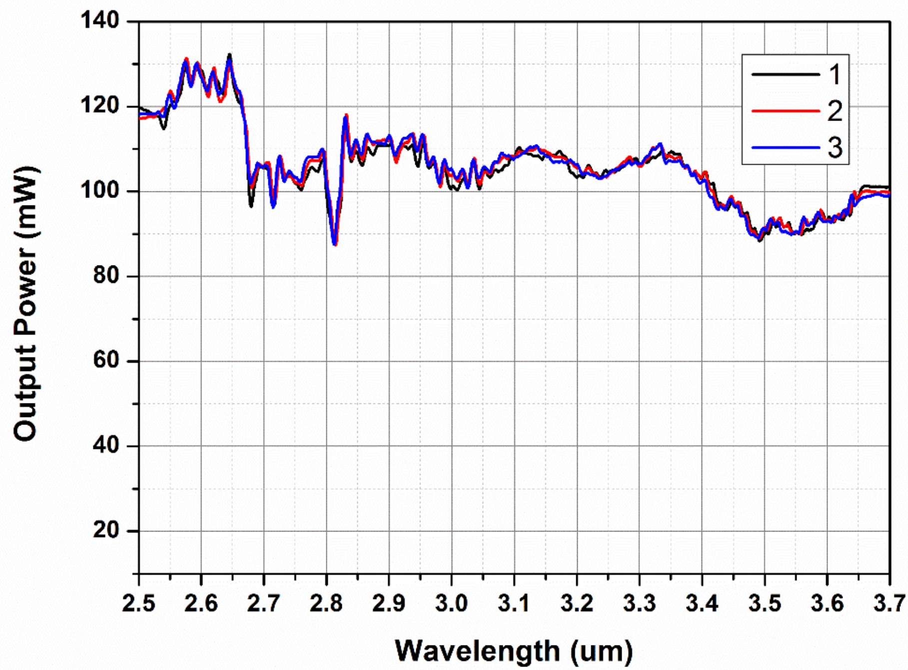

Fig. 3.9 Output power recorded from the OPO laser operating at wavelengths between 2.5 μm and 3.7 μm

3.5.1B ZnSe objective (Innovative Photonics): Light from the OPO was focused onto a ZnSe objective lens with an anti-reflection coating centred at 3.75 μm wavelength and a numerical aperture (NA) of 0.25. The focal length of the lens is 6 mm. The beam diameter is reduced to ~15 μm at the focus of the lens [161].

3.5.1C Optical fibers (Thor labs): The light from ZnSe lens was focused into a single mode (SM) zirconium fluoride (ZrF_4) fiber with a core diameter of 9 μm. This fiber operates in a single mode at wavelengths between 2.3 μm and 3.6 μm and has an NA of 0.19 ± 0.02 [162]. The other end of the fiber was butt-coupled into the input facet of the waveguide and the output of the waveguide was collected using a multimode (MM) indium fluoride (InF_3) fiber with core diameter ~100 μm and operating wavelengths of 310 nm to 5.5 μm. This fiber has an NA of 0.26 ± 0.02 [162].

3.5.1D Thermal imaging camera (FLIR, A6540sc): The top surface and the cross-section of the guided modes at the output of the waveguide were imaged using an InSb MIR camera. The input and output coupling between the waveguide and the fibers were also ensured by imaging using this MIR camera, which covers the spectral range from 1.5 μm to 5.1 μm and has a pixel array of 640 x 512 with a pixel pitch of 15 μm.

3.5.1E Detector (Vigo System, PVMI-2TE-10.6): A thermo-electrically (TE) cooled Mercury Cadmium Telluride (MCT) photovoltaic detector [163] was used to detect the signal coming out of the collection fiber. The MCT detector has an active area of 1 mm with a barium fluoride window. The detector's responsivity or detectivity curve is shown in Fig. 3.10, which was reproduced from the diagram provided by the manufacturer. The detector's time constant is ~3 ns.

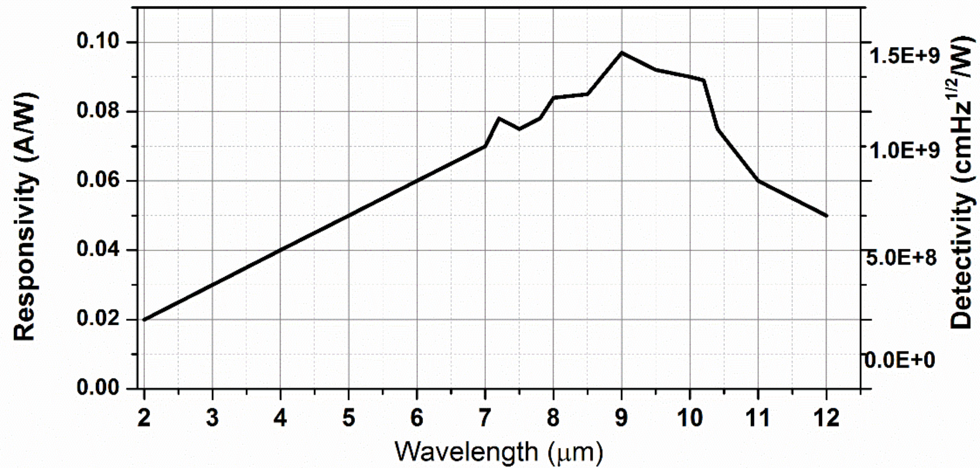

Fig. 3.10 TE cooled MCT detector's responsivity and detectivity spectrum [from manufacturer's test data]

3.5.2 <u>LWIR experimental apparatus:</u>

For waveguide characterization at wavelengths from 6 μm to 12 μm, a similar set-up as shown in Fig. 3.7 is used with suitable laser source, objective lens and coupling fibers for LWIR.

3.5.2A Laser source (Pranalytica): A tunable and pulsed quantum cascade laser (QCL) operating at wavelengths between 6 μm and 12 μm was used as a light source. It operates at room temperature with 50-500 ns pulse operation at a pulse repetition rate of 1-2 MHz and has four laser chips inside which can be tuned continuously across the whole tuning range. The average output power is 150 mW for a duty cycle of up to 50%. The output power of the QCLs vs wavelenngth is shown in Fig. 3.11, as provided by the manufacturer.

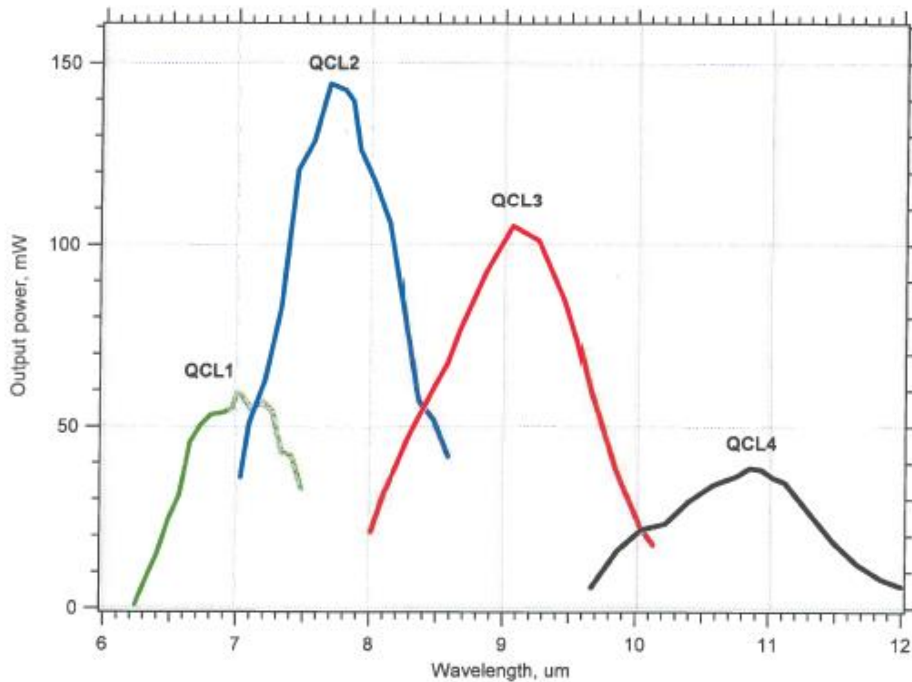

Fig. 3.11 Output power spectrum of QCL operating at wavelengths between 6 µm and 12 µm

3.5.2B ZnSe objective (Innovative Photonics): Light from the QCL was focussed into a ZnSe objective lens with an anti-reflection coating centred at λ = 8.5 µm. It has an NA of 0.13 and a focal length of 6 mm. The beam diameter is reduced to ~30 µm at the focus of the lens [161].

3.5.2C Optical fiber (Cor Active/IRFlex): Light from the ZnSe objective coupled into a SM As_2Se_3 fiber. Two SM As_2Se_3 fibers were used, one with a core diameter of 27 µm (Cor Active) and an NA of 0.22 and the other with a core diameter of about 12 µm (IRFlex) with an NA of ~ 0.47. The other end of the fiber was used to butt-couple with the waveguide. The coupling efficiency between the laser and the input fiber is ~ 13% and between the fiber and the waveguide is estimated to be ~50%.

3.5.2D Thermal imaging cameras (Xenics-Gobi 640/ FLIR SC660): The top and cross-section of the guided modes of the waveguides were imaged using microbolometer based thermal imaging cameras. The Xenics camera covers a spectral band of 8 -14 µm and has a thermal sensitivity ~ 50 mK at 30°C with a pixel array of 640 x 480 and a pixel pitch of 17 µm. The FLIR camera covers the wavelength range from 7.5 µm to 13 µm and has a

thermal sensitivity of 30 mK at 30°C with a pixel array of ~ 640 x 480 and a pixel pitch of 25 μm.

3.5.2E Detector (Vigo System, PVMI-2TE-10.6): The same TE cooled MCT detector is used for LWIR, as explained in 3.5.1E.

3.6 Conclusion

The $GeTe_4$ and ZnSe film deposition tools and procedures were discussed. The tools used to determine the film's surface, morphological, crystallinity, roughness, compositional and optical properties were briefly explained. An overview of the procedures followed for fabricating channel and rib waveguides by photolithography, lift-off and etching was presented. The apparatus used for waveguide characterisation in the MWIR and the LWIR regions of MIR were described. The next chapter includes the results on deposition of $GeTe_4$ films, fabrication of channel waveguides as well as its characterisation in both the MWIR and the LWIR regions.

CHAPTER 4 $GeTe_4$ thin films and waveguides on ZnSe

In this chapter deposition, fabrication and characterization of $GeTe_4$ waveguides on bulk ZnSe substrate are discussed. A high refractive index (RI) contrast configuration with a $GeTe_4$ core layer and ZnSe as the substrate, (n_{GeTe4} = 3.34 and n_{ZnSe} =2.4 at λ =3.5 μm) has been used. $GeTe_4$ films were deposited by RF sputtering and characterised for their structure, morphology, composition, transparency and dispersion. A two-step lift-off technique (explained in chapter 3, section 3.3.2A) using a positive photoresist and a lift-off resist (LOR) was used to fabricate channel waveguides. The end facets of the waveguides were prepared by ductile dicing. Waveguiding in the MWIR at wavelengths between 2.5 μm and 3.7 μm and in the LWIR at wavelengths between 6.4 μm and 9.4 μm was demonstrated. The mode intensity profile and the estimated propagation losses are given for the 3.5 μm wavelength.

4.1 Deposition of $GeTe_4$ films

A commercial target of $GeTe_4$ (150 mm diameter x 6mm thick) with Ge:Te ratio of 1:4 with 99.99% purity was used. $GeTe_4$ films were deposited on 2 mm thick and 50 mm x 50 mm square polycrystalline ZnSe substrates by RF magnetron sputtering in an argon atmosphere. The base pressure of the system was 7.5 x 10^{-7} Torr before deposition. Several films were deposited at different temperatures to study the effect of deposition temperature on film properties. However, the waveguides were fabricated using films

deposited at room temperature. Deposition parameters such as sputtering power, pressure, and argon flow rate were varied to optimize the deposition rate.

The $GeTe_4$ deposition rate was measured as a function of sputtering pressure and sputtering power at room temperature. The sputtering pressure was varied from 3 mTorr to 30 mTorr at a fixed power of 50 W and an Ar flow rate of 20 sccm. The sputtering power was varied from 30 W to 60 W at a fixed sputtering pressure of 10 mTorr and a fixed Ar flow rate of 25 sccm. Fig. 4.1 shows the relationship of deposition rate to sputtering pressure and power respectively for $GeTe_4$ films deposited on ZnSe substrate. It is seen that deposition rate decreases with sputtering pressure because the amount of sputtered species increases with pressure as long as the mean free path of the sputtered species is lower than the target-substrate distance. After that the number of collisions between Ar gas and the sputtered species increases and hence the deposition rate decreases. At a fixed pressure, with increasing power, the velocity of sputtered species increases and hence the deposition rate [164].

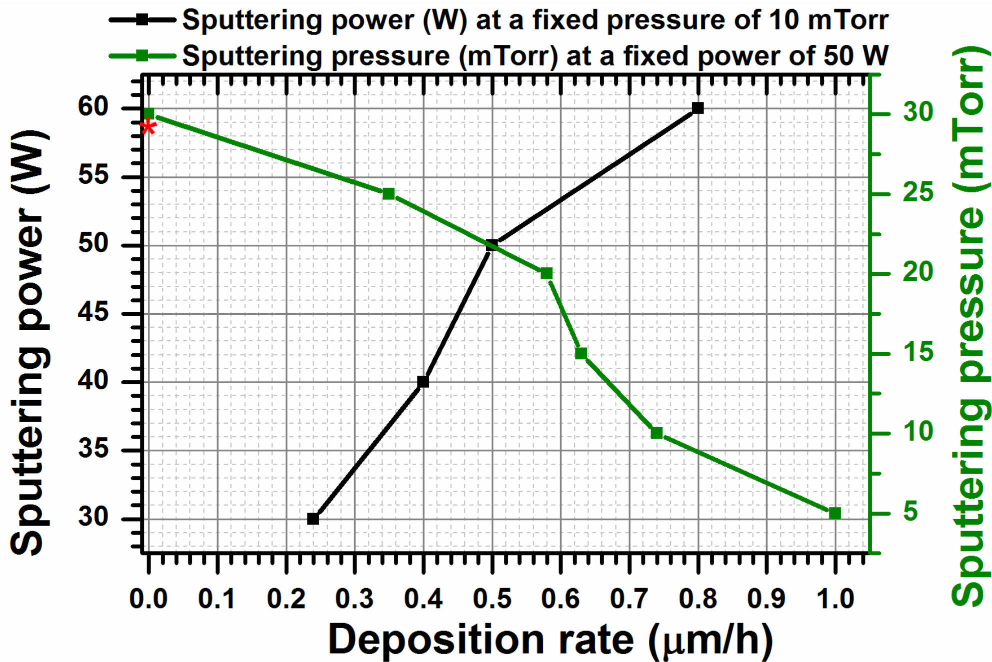

*Fig. 4.1 Deposition rate of $GeTe_4$ films as a function of sputtering pressure and sputtering power. (*indicates the plasma did not strike at that pressure)*

A sputtering pressure of 10-15 mTorr and power of 40−50 W yielded visibly defect free films with a deposition rate of 0.6−0.7 µm/h. The red asterisk in Fig. 4.1 shows that the

plasma did not strike at that pressure. Films of thicknesses ranging from 1−8 μm were deposited.

4.2 Characterisation of $GeTe_4$ films

4.2.1 Crystallinity, surface morphology and roughness

XRD was used to determine the crystallinity or phase of the deposited film. The sample was kept in the XRD chamber, where X-rays are incident on the sample at a grazing angle of 1° and are detected by a detector in the range of 10°−80°. For crystalline materials, this gives a sharp peak at a unique angle since all the atoms are in an ordered arrangement. For polycrystalline materials, a number of sharp peaks at different angles are obtained that represent diffraction from many grain boundaries of a polycrystalline material as seen in Fig. 4.2(a) (i) which shows the XRD pattern of a polycrystalline ZnSe substrate.

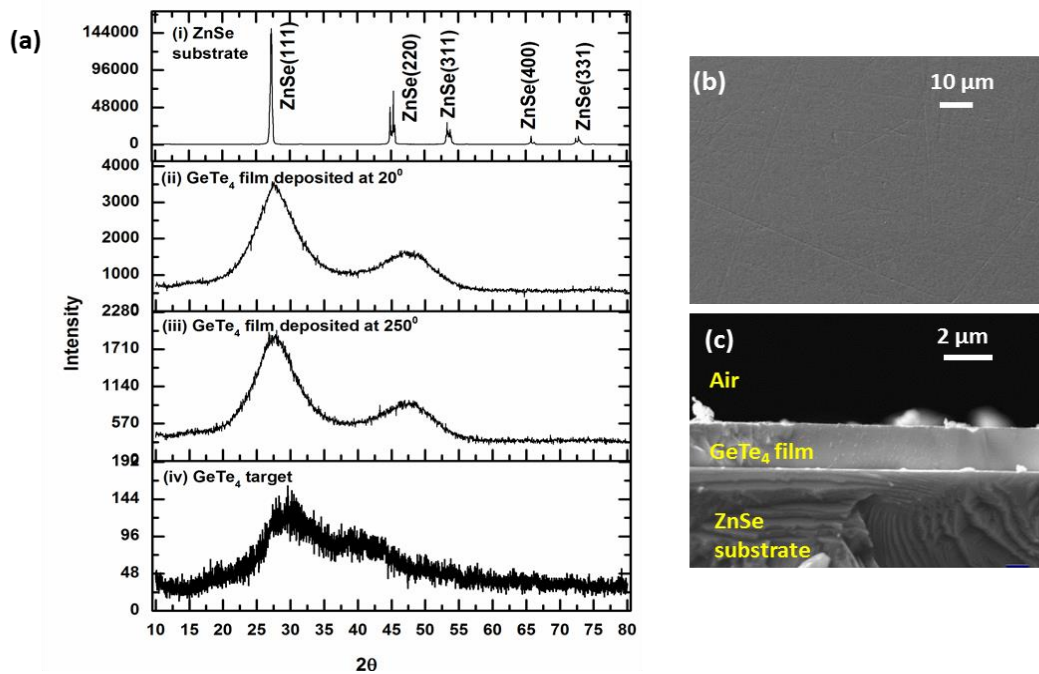

Fig. 4.2 (a) XRD pattern of (i) a polycrystalline ZnSe substrate, (ii), (iii) a $GeTe_4$ film deposited at a temperature 20°C and 250°C, respectively, and (iv) $GeTe_4$ target, SEM images of (b) top surface and (c) the cleaved cross-section of an as-deposited $GeTe_4$ film on ZnSe substrate

For amorphous material, a broad curve is obtained because the molecules lack the long range order. Fig. 4.2(a) (ii) and (iii) shows the XRD pattern of sputtered $GeTe_4$ films at room temperature (20°C) and at 250°C respectively. It was found that deposited films

were amorphous. The films remain amorphous at different sputtering powers from 30-60 W and different deposition temperatures from 20-250°C. Fig. 4.2(a) (iv) shows XRD pattern of the $GeTe_4$ target showing its amorphous nature.

The surface of the deposited films was observed under an optical microscope and SEM to ensure that the film formation is two dimensional that is it is flat and there is no three dimensional growth or island formation. Fig. 4.2 (b) shows SEM images of the top surface of a deposited $GeTe_4$ film which shows that the surface of the film is smooth. Fig. 4.2 (c) shows the cleaved cross-section of a $GeTe_4$ film showing a dense film, free from any porosity or defects [165, 166]. Since the substrate is polycrystalline, its different planes are also visible in the SEM image.

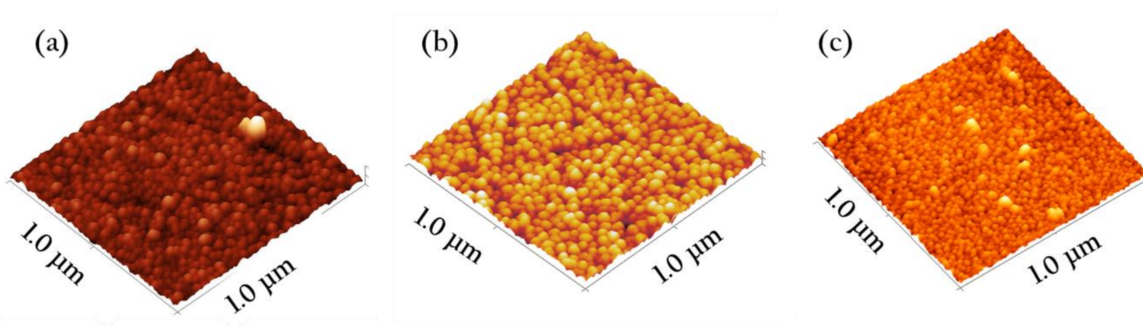

Fig. 4.3 AFM image of 1x1 µm2 scan area of (a) ZnSe substrate and $GeTe_4$ film deposited at temperature (b) 20°C and (c) 250°C respectively

AFM in tapping mode was used to measure the surface roughness of the deposited films and the substrate. Fig. 4.3 (a), (b) and (c) shows the AFM graphs of the surface of the 1x1 μm^2 ZnSe substrate, the $GeTe_4$ film deposited at room temperature (20°C) and that deposited at 250°C respectively. The local roughness value for the surface of the substrate is found to be ~2.4 nm whereas that of the film deposited at 20°C is ~4 nm. Although this value of roughness is acceptable for our device and application since we are working at long wavelengths (2.5−14 µm), still this roughness could be significantly reduced when the films are deposited at higher deposition temperatures; for instance it is 1.2 nm for the film deposited at 250°C. Difference in particle size of the film deposited at different temperatures was observed and explains their different surface roughness. The films used to fabricate the waveguides were all deposited at room temperature.

4.2.2 Optical transmission

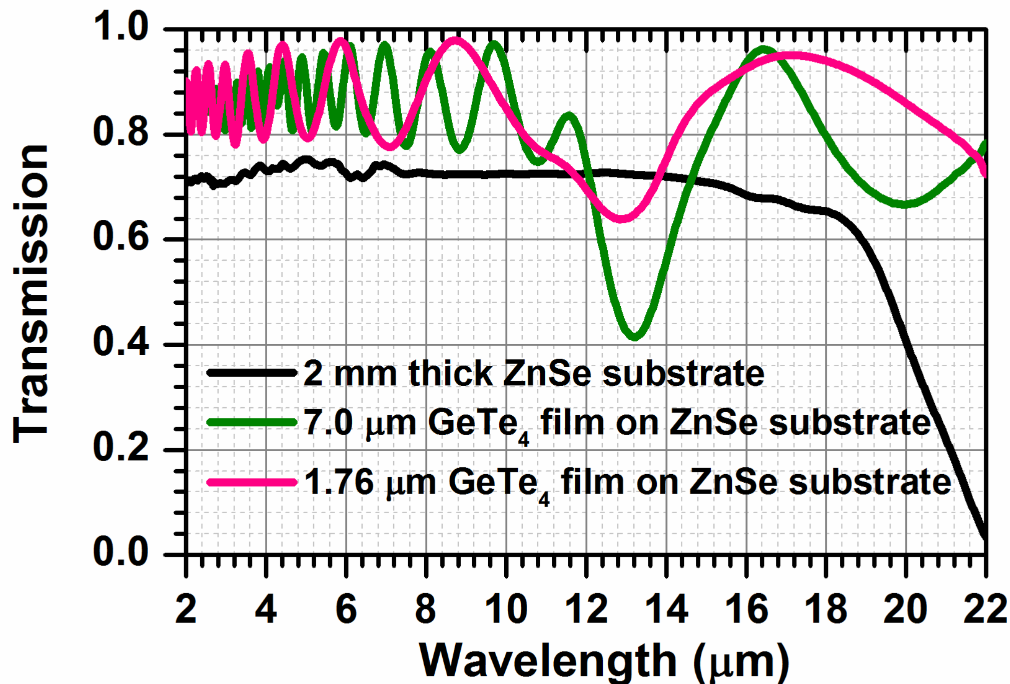

Fig. 4.4 FTIR spectra of 1.76 μm and 7.0 μm thick $GeTe_4$ film, and 2 mm thick ZnSe substrate

It is important to ensure that the film and the substrate material transmit in the MIR region. The transmission from a 2 mm thick ZnSe substrate with no $GeTe_4$ film and with 1.76 μm and ~ 7.0 μm thick $GeTe_4$ films were measured by FTIR and the spectra are shown in Fig. 4.4. The $GeTe_4$ films were found to transmit over the spectral range from 2−20 μm. However, in the wavelength region of 12−15 μm, $GeTe_4$ films caused a significant drop in transmission. A 2 mm ZnSe slab cuts off at ~ 19 μm, where its transmission reduces to 50%.

In order to understand the absorption of $GeTe_4$ film (in ~ 7.0 μm thick $GeTe_4$) in the wavelength region of 12−15 μm shown by FTIR, a theoretical model based on matrix method using Fresnel's coefficients constructed from O. S. Heaven [167]. The model assumes normal incidence of light on a thin absorbing film on a transparent substrate. For an absorbing film, refractive index n is replaced by a complex refractive index, and the imaginary part is related to the absorption of energy by the medium. A schematic of the single layer structure used in the model is shown in Fig. 4.5. When a plane wave enters the plane boundary of an isotropic, absorbing medium, the planes of equal phase of the

wave in the medium are perpendicular to the direction of propagation. The reduction in the amplitude of the wave depends directly on the distance travelled by the wave in the medium, for normal incidence, planes of equal phase are parallel to those of equal amplitude. On applying the boundary conditions to the solutions of Maxwell's equations (discussed in Chapter 2, section 2.2), light reflected or transmitted by a boundary separating the two media can be calculated.

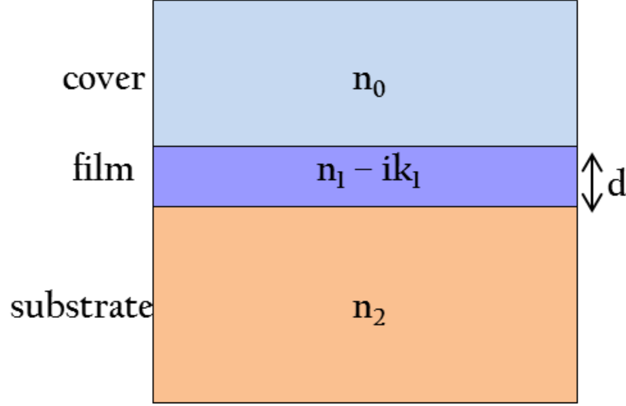

Fig. 4.5 Schematic of an absorbing film on a transparent substrate

The complex Fresnel reflection (r_m) and transmission coefficient (t_m) are given by:

$$r_m = g_m + ih_m \quad 4.1$$

$$t_m = 1 - r_m \quad 4.2$$

where m denotes the number of layers. For a single absorbing film on a transparent substrate, the transmittance (T_1) is given by:

$$T_1 = \frac{n_2}{n_0} \cdot \frac{[(1+g_1)^2 + h_1^2][(1+g_2)^2 + h_2^2]}{e^{2\alpha_1} + (g_1^2 + h_1^2)(g_2^2 + h_2^2)e^{-2\alpha_1} + Ccos(2\gamma_1) + Dsin(2\gamma_1)} \quad 4.3$$

where

$$g_1 = \frac{n_0^2 - n_1^2 - k_1^2}{(n_0 + n_1)^2 + k_1^2} \quad 4.4$$

$$g_2 = \frac{n_1^2 - n_2^2 + k_1^2}{(n_1 + n_2)^2 + k_1^2} \quad 4.5$$

$$\alpha_1 = \frac{2\pi k_1 d_1}{\lambda}; \gamma_1 = \frac{2\pi n_1 d_1}{\lambda} \quad 4.6$$

$$h_1 = \frac{2n_0 k_1}{(n_0 + n_1)^2 + k_1^2} \quad 4.7$$

$$h_2 = \frac{-2n_2 k_1}{(n_1 + n_2)^2 + k_1^2} \quad 4.8$$

$$C = 2(g_1 g_2 - h_1 h_2) \quad 4.9$$

$$D = 2(g_1 h_2 + g_2 h_1) \quad 4.10$$

The subscript 1 is used for the cover-film interface and 2 is used for the film-substrate interface. The values of n_1 and k_1 are the real and imaginary parts of RI of $GeTe_4$ and n_2 is the RI of ZnSe taken from ellipsometry measurement discussed in section 4.2.3. The thickness of $GeTe_4$ from the model is calculated to be 7.08 µm. The transmission T_1 from the model is calculated from equation 4.3. The transmission T_1 corrected for ZnSe background is plotted in Fig. 4.6 along with the transmission of $GeTe_4$ film obtained from the FTIR measurement. The model is in general in agreement with the theory, except at shorter wavelengths. Further work is under investigation.

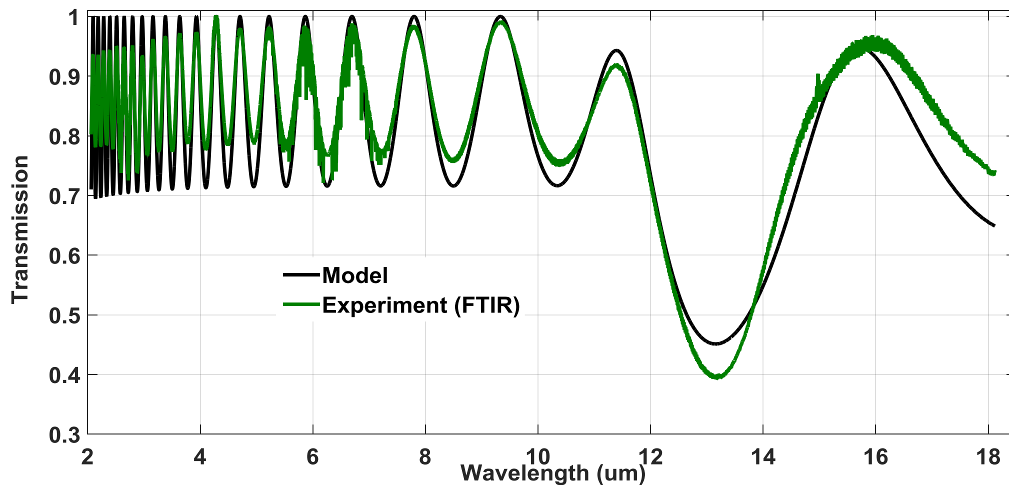

Fig. 4.6 Experimental and theoretical transmission of ~7.0 µm $GeTe_4$ film deposited on ZnSe substrate

4.2.3 Optical constants

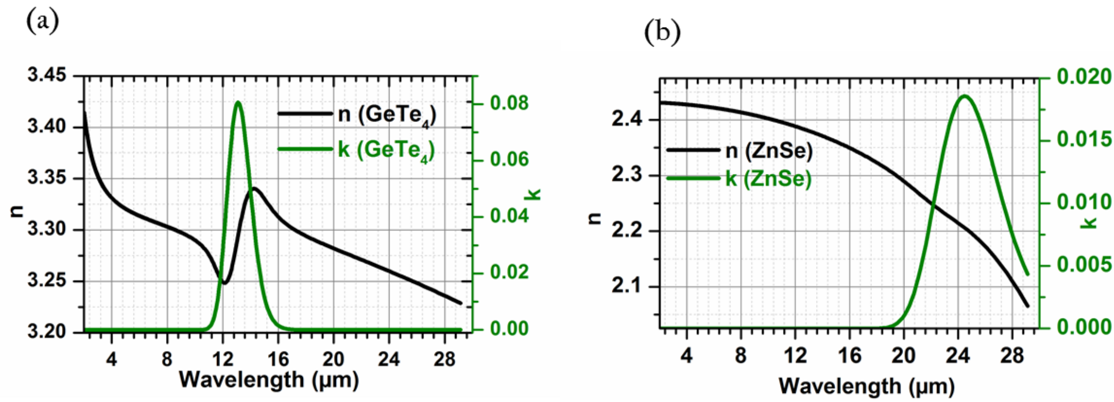

Fig. 4.7 Ellipsometry graphs showing the optical constants n and k for (a) the $GeTe_4$ film and (b) ZnSe substrate

The optical constants n and k of the $GeTe_4$ film and of ZnSe substrate were determined by IR-Vase ellipsometry. It is important to know the dispersion and absorption of a material which is given by n(λ) and k(λ) respectively, in order to design a waveguide to ensure there is no intrinsic material absorption at the wavelength of interest. Fig. 4.7 (a) shows n and k plotted against wavelength for a 2.7 μm $GeTe_4$ film as measured by ellipsometry. An absorption peak in the 12−15 μm wavelength region is clearly seen in the absorption spectrum, which corresponds to the Ge-O bond [168]. This absorption is also observed was also indicated by the FTIR results shown in Fig. 4.4. In Fig. 4.7 (b), n and k for ZnSe substrate is shown and it can be observed that the ZnSe substrate did not show any such absorption in the entire wavelength region from 2−18 μm, above which it starts to absorb.

The material loss in dB/cm was calculated using the extinction coefficient, k, obtained from the ellipsometry data of $GeTe_4$ film and is shown in Fig. 4.8. In the same figure the inset shows the magnified image of a region close to 10 μm wavelength. It can be seen that the losses are very high in the region above 10.8 μm, which are believed to be caused by the GeO absorption. However, the film shows negligible losses for wavelengths below 10 μm, which is very promising for the spectroscopy of many clinical analytes in MIR. In order to establish the cause of this strong absorption peak, a detailed compositional analysis was required which is explained in the next section.

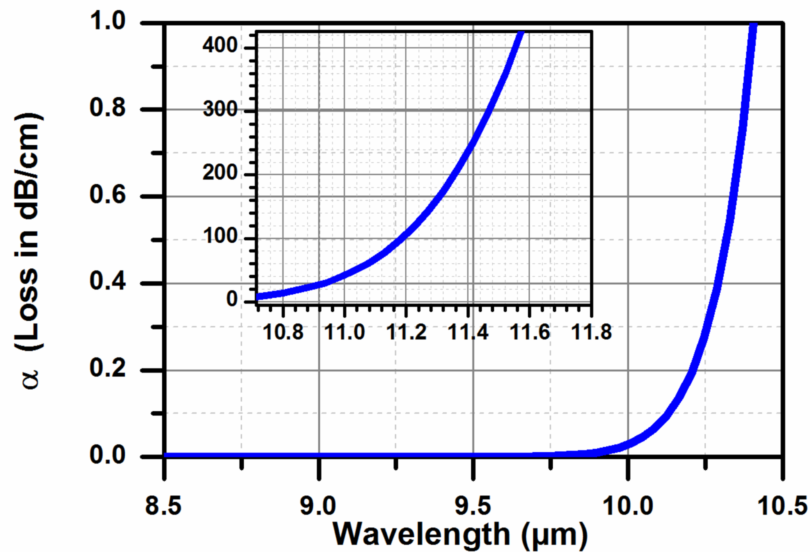

Fig. 4.8 $GeTe_4$ material loss in dB/cm calculated using extinction coefficient, k, from ellipsometry data. Inset: A small region is zoomed in around 10 μm wavelength, where losses start to appear

4.2.4 Composition:

The composition of the film was determined in order to ascertain the reason behind the strong absorption peak in the 12–15μm spectral range. EDX was used initially to measure the composition, however, as it gives the spatially averaged amount of each element depending on the probe area, the results were not satisfactory, as it could not be known if this contribution of oxygen is from the surface, interface between the film and the substrate, or the bulk of the film. From EDX, an oxygen content of 7-8 atomic % was obtained in 2.0 μm thick $GeTe_4$ films whereas 11-22 atomic % oxygen was found in the $GeTe_4$ target (the measurements were performed on three different regions of the sample). The EDX measurement on the target was performed after using it for deposition for more than three years whereas the films were measured during the first few months of deposition. A surface sensitive technique that can give a detailed analysis of the elements as well as information on their bonding with other elements was required. XPS was a suitable choice because of its availability as well as its ability to provide surface sensitive measurements of the elemental and chemical information. The probe depth is about the top few nm of sample. The instrument gives a plot of electron counts vs. binding or kinetic energy. The position of the peaks gives the information about the element present whereas the peak area shows the amount of the element present. The shape of the peaks

and their shifts in binding energy gives the information about the chemical state of the element.

Chalcogenides have history to form bonds with oxygen or hydrogen, which leads to unnecessary material absorption in the wavelength region of interest, so it was important to confirm the penetration of oxygen in the samples, which is performed by XPS. It utilised to study the depth profile of a material by physically etching out the material by argon ions to introduce a fresh surface every time for the measurement. This way it can found how a particular element environment or its composition is varying with depth.
Initially, to estimate the etch depth corresponding to Ar^+ ion etching, measurements were conducted after every 10 minutes of etching on a 2.5 μm thick $GeTe_4$ film. One hour of etching exposed the ZnSe surface, so it is estimated that every minute of etching corresponds to about 40 nm of the film thickness. After fitting the data, it was found that the top-most layer of the film was mostly oxide (about 72%), which consists of Ge-O and $Te\text{-}O_2$. The further etched levels showed absence of $Te\text{-}O_2$ and Ge-O settled down at 2 atomic %. It can be seen in Fig. 4.9 (a) and (b). To further explore the composition of the $GeTe_4$ film surface, another depth profile experiment was set-up with the depth profile obtained every 20 seconds, shown in Fig. 4.9 (c). It clearly shows that the oxygen content stabilises after about 40 nm of etch depth and about 2% oxygen in the form of Ge-O always remain throughout the thickness of the film.
This oxygen contamination is in agreement with the FTIR and ellipsometry data reported above in sections 4.2.2 and 4.2.3, where Ge-O absorption at 12-15 μm spectral region was found. The XPS results confirmed that the top 40 nm of the $GeTe_4$ film surface was comprised of GeO and TeO_2. A more detailed analysis also showed that TeO_2 was in the first few nm (10 nm) of the film but approximately 2% Ge-O was present throughout the film. The contamination may result from the impurity in the commercial target material. These could be eliminated by purifying the target material or by depositing a passivation layer on the surface of the deposited films respectively.

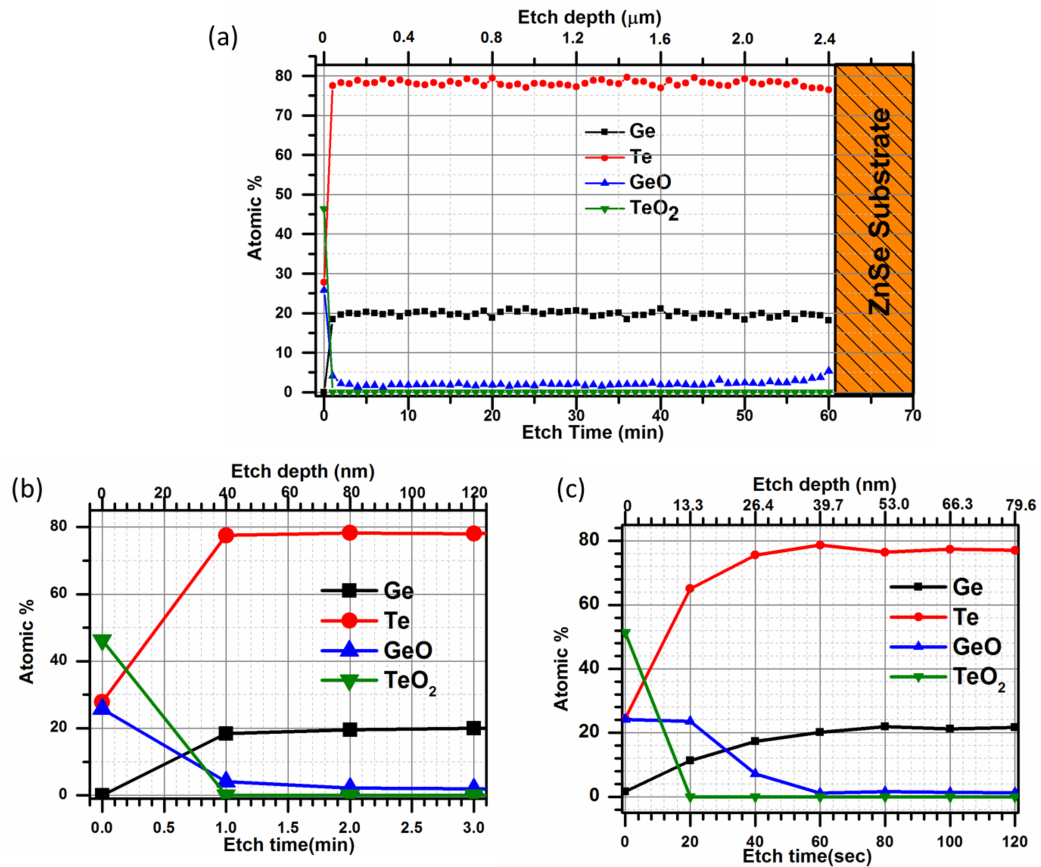

Fig. 4.9 Depth profile of GeTe4 film by XPS showing composition of the film (a) after every minute etching until the substrate was reached (b) shows the initial 3 minutes with every 1 minute etching data and (c) shows the initial 120 sec etched every 20 sec

4.3 GeTe4 waveguide fabrication

After the film characterisation, $GeTe_4$ channel waveguides were fabricated using the lift-off technique as explained in chapter 3, section 3.3.2. A two layer photoresist process was followed. First, an 8 µm thick layer of lift off resist (LOR 30B) was spun on a cleaned ZnSe substrate, followed by a 1.3 µm thick film of S1813 photoresist. The sample was then UV-exposed through a photolithography mask comprising straight opaque stripes of width ranging from 1 to 10 µm with centre to centre distance 100 µm and developed to create the desired undercut profile shown in Fig 4.10 (a) [169].

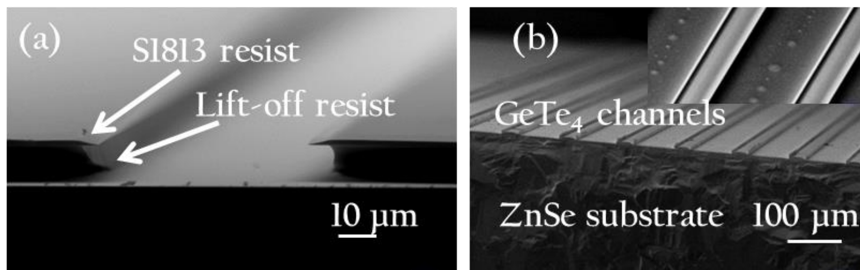

Fig. 4.10 (a) Undercut created by LOR and photoresist and (b) Cleaved cross-section of $GeTe_4$ channels on bulk ZnSe substrate after stripping off the LOR and photoresist (inset: top view of the channels)

A $GeTe_4$ film of about 4.6 μm thickness was deposited onto the patterned resist by RF sputtering as discussed in section 4.1. Finally, the resist and the LOR were lifted off in resist stripper (SVC-14) to obtain the waveguide channels shown in the SEM images in Fig. 4.10 (b). The process was not optimised so 1–10 μm wide stripes on the mask widened to 15–35 μm on the sample after the photolithography procedure. These wide channels are highly multimode (> 20 modes) for 3.5 μm wavelength. The wide channels were characterised in the MIR in order to establish waveguiding at longer wavelengths with sufficient coupling efficiency using commercially available single mode fibers having core diameters of 12 and 30 μm. In addition, the resolution of MIR optics is poor because of the fundamental diffraction limit and imaging single mode waveguides with submicron dimensions is extremely difficult.

In order to prepare the end-facets of the waveguide for coupling light in, conventional polishing with ethane-diol was evaluated. Ethane-diol was used instead of water to mix the alumina slurry for polishing to avoid any unwanted absorption due to water. The polishing was not successful and resulted in chipped edges of the samples. A microscope picture of the polished sample is shown in Fig. 4.11 (a), where the rough and chipped off edges of the substrate are clearly visible. To overcome the polishing problem, ductile dicing was employed to machine the $GeTe_4$ waveguide end facets. Here the sample was coated with S1813 photoresist to protect the $GeTe_4$ channels from coming in direct contact with water which was used in dicing and also to protect the sample from any mechanical damage. The ductile dicing process created smooth and chip free waveguide facets as shown in the SEM image in Fig. 4.11 (b). The average surface roughness of the end facets was obtained with a white light interferometer (Zemetrics, ZeScope) and found to be ~3.0 nm [159]. A schematic and an SEM image of the cross-section of the waveguide facet

machined in the ductile dicing regime (after removing the protective photoresist) are shown in Figure 4.11 (c) and (d) respectively.

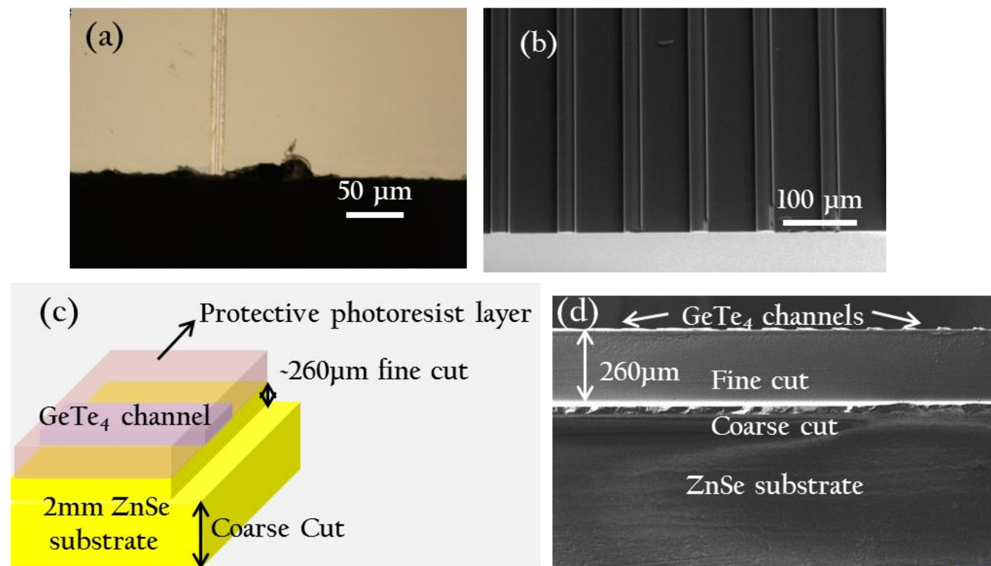

Fig. 4.11(a) A microscope image of the polished $GeTe_4$ channel waveguides on ZnSe substrates, (b) an SEM image of $GeTe_4$ channel waveguides cut by ductile dicing, (c) a schematic of the end facet of the waveguides cut by ductile dicing and (d) an SEM image showing the cross-section of the diced end facet of the waveguides

4.4 $GeTe_4$ waveguide characterisation in the MIR

The diced samples were characterised with a tunable OPO working at wavelengths between 2.5 μm to 3.7 μm. Light from the OPO was focused on a ZnSe objective lens into a SM ZrF_4 fiber. The other end of the fiber was butt-coupled into the input facet of the channel waveguide and the output was imaged on the InSb MIR camera from the top and at the output cross-section. A schematic of the experimental set up is shown in Fig. 4.12.

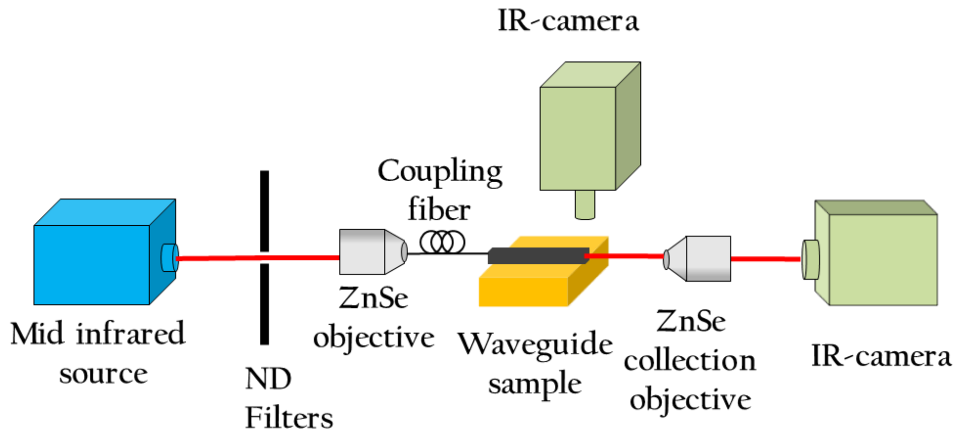

Fig. 4.12 Experimental apparatus for optical characterisation of the waveguides

Fig. 4.13 (a) and (b) shows a top view and the cross-section of the output end of the waveguide sample showing light scattered from the end of a 26 µm wide and 4.6 µm thick channel waveguide at a wavelength of 3.5 µm. The channels are clearly seen in Fig. 4.13 (a). The insets in Fig. 4.13 show the magnified image of the guiding channel.

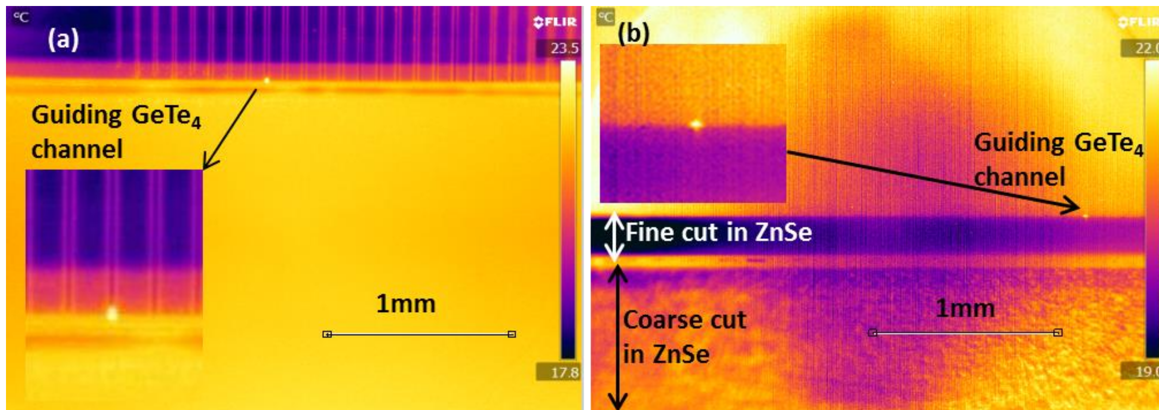

Fig. 4.13 Infra-red camera images (taken with the inbuilt camera lens) of the output facet of the guiding channel waveguide seen from (a) top and (b) cross-section view (inset: magnified image of the guiding channel)

In order to magnify the mode emerging from the waveguide end-facet, the built-in camera lens was replaced by an external ZnSe objective lens (refer Fig. 4.10) and the mode was magnified by a factor of ~ 8 by adjusting the distance between the waveguide, ZnSe lens and the camera. Fig. 4.14 (a) shows the background corrected infrared image of the magnified guiding mode. It is the difference between the images with the OPO on and off,

and is a true thermal image of the temperature difference. The scale of the modal images was calibrated using the known distance between two waveguides. Light guidance was observed over the wavelength range from 2.5 μm to 3.7 μm. On moving the input fiber exactly 100 μm, which is the distance between two waveguides, another channel output is illuminated confirming the confinement of light.

The experimental horizontal and vertical mode profiles were extracted from Fig. 4.14 (a) and are shown in Fig 4.14 (b) together with theoretical mode profiles for the fundamental mode of the $GeTe_4$ channel waveguide calculated using COMSOL. The experimentally measured full width half maxima (FWHM) mode intensity spot-sizes for the waveguide output intensity distribution in the horizontal and vertical directions of the 26 μm wide and 4.6 μm thick channel waveguide are 10.2 μm and 7.8 μm, respectively. The "vertical" direction is defined as normal to the substrate surface. The FWHM spotsizes calculated by COMSOL for the fundamental mode in the horizontal and vertical directions at λ=3.5 μm are 13.2 μm and 2.4 μm respectively. As the waveguide is highly multimoded at this wavelength and the image resolution is ~5 μm, it is unclear which modes have been excited in practice. If the fundamental mode has been excited in the vertical direction, then the measured mode profile compares well with the theoretical mode profile, taking in to account the resolution of the imaging system. It is unclear why the measured spotsize in the horizontal direction is smaller than that predicted theoretically. It is postulated that the 9 μm core input fiber excites several modes (laterally) in the waveguide and that these self-image along the waveguide, acting like an MMI [170], to produce a narrow resultant intensity distribution at the waveguide output facet.

In order to explore waveguide losses, the streak of scattered light at λ=3.5 μm was observed from above the waveguide as shown in Fig. 4.14 (c). It is clear that there are many large scattering centers along the waveguide in addition to a more uniform scattering distribution. The former are due to imperfections in the lift-off process which has left irregularities on the walls of the channels. The propagation loss calculated from these data was found to be in the range of 1-5 dB/cm, depending upon the region of the image selected for analysis.

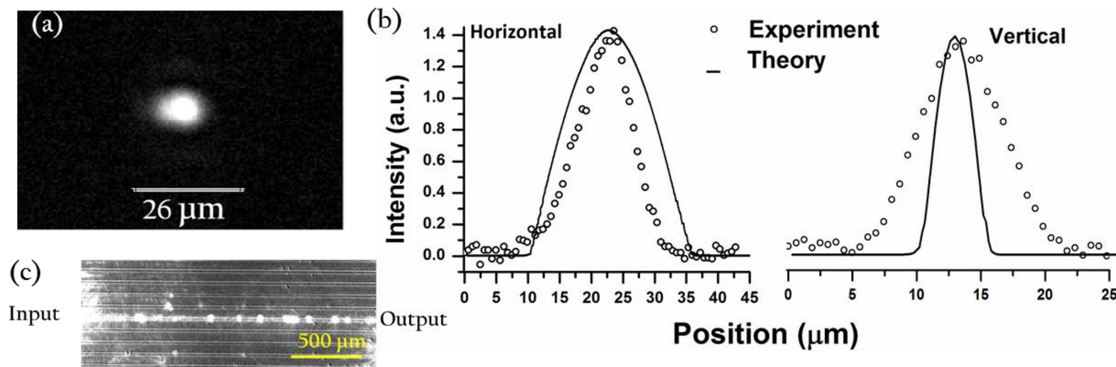

Fig. 4.14(a) Magnified background corrected infrared image of the mode at 3.5μm wavelength, (b) measured horizontal and vertical fundamental mode profiles with theoretical comparison and (c) Infrared image showing streak of light in the guiding channel at λ=3.5μm

For waveguide characterisation in 6.4−9.4 μm region, light from a tunable QCL was coupled in to the waveguide end facet using a single mode As_2Se_3 fiber with a core diameter of about 30 μm. The output was imaged using a microbolometer based mid-infrared camera from the top. The same waveguide sample (the one tested at shorter wavelengths) was tested at longer wavelengths, using the QCL, and was found to be guiding light over 6.4−9.4 μm wavelength region. Fig. 4.15 (a) and (b) shows infrared images using the mid-infrared camera with its as-supplied in built lens. Fig. 4.15 (a) and (b) shows the top and cross-section view of the guiding channel at λ = 6.8 μm emerging from a waveguide end and this region is shown expanded in the inset. On moving the sample exactly 100 μm, the distance between two waveguides, consecutive channels are excited. As explained above, the guided mode was magnified by using an external ZnSe lens and the magnified mode image is shown in Fig. 4.15 (c) where a clear bright circular spot was observed.

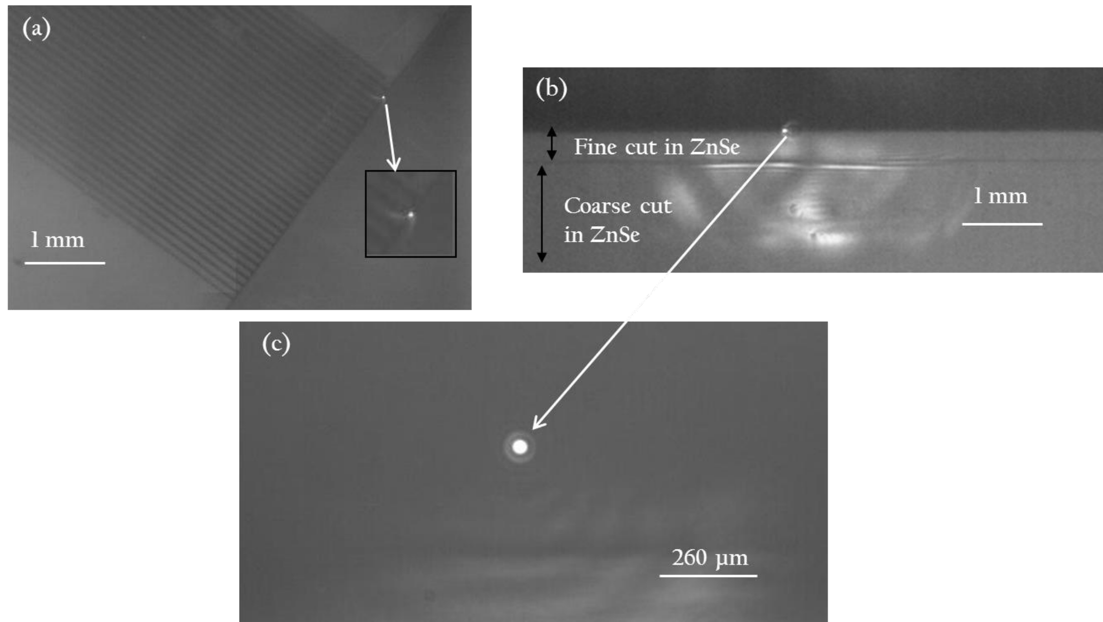

Fig. 4.15(a) Top view and (b) cross-section of the infra-red camera image of the output facet of the guiding channel waveguide at 6.8 µm wavelength (c) magnified image of the guiding channel

A FLIR camera image of the waveguide sample guiding at λ = 8.5 µm is shown in Fig. 4.16 and the inset shown the magnified image of the guiding spot.

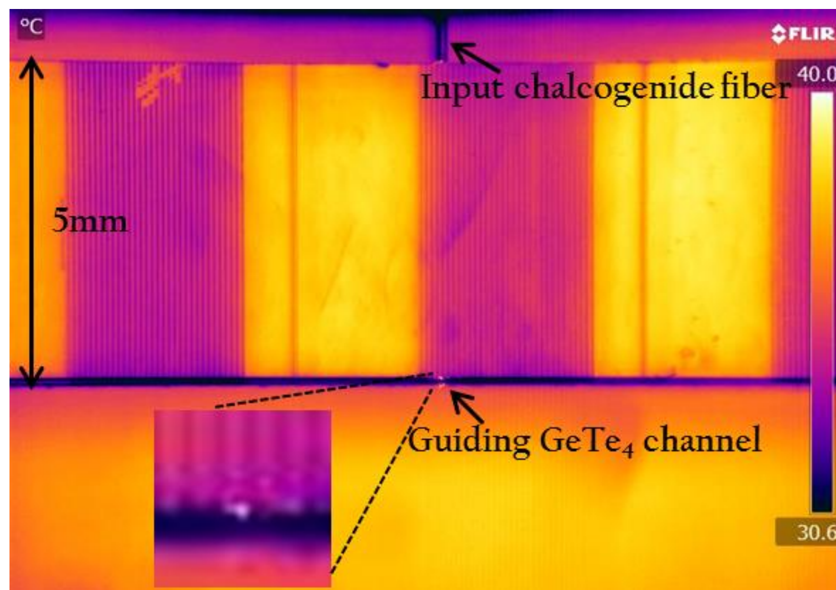

Fig. 4.16 Infrared image showing waveguiding at 8.5µm wavelength (inset: magnified image of the guiding channel)

4.5 Conclusions

$GeTe_4$ films were deposited on ZnSe substrate by RF sputtering in an argon atmosphere. Deposition parameters, sputtering pressure of 10−15 mTorr and sputtering power of 40−50 W were found to give a deposition rate of 0.5−0.6 μm per hour which was used to deposit the films of various thicknesses. The average surface roughness of the films deposited at room temperature was found to be 5 nm or less, sufficiently low for low-loss waveguides at MIR wavelengths. The deposited films were amorphous, as required to minimize scattering. The films were found to transmit over a spectral range of 2−20 μm. XPS analysis showed the presence of oxygen contamination in the film which is primarily due to the Ge-O absorption at 12-15 μm. This contamination resulted in large losses at wavelengths longer than 10 μm, as determined by spectroscopic ellipsometry. Further improvements in the material purity are expected to lead to waveguide films suitable for the full spectral region between 2 μm to 20 μm. Waveguiding was demonstrated in the 2.5−3.7 μm and 6.4−9.4 μm wavelength ranges. The mode intensity profile was extracted at a wavelength of 3.5 μm and preliminary estimates of propagation losses were reported.

In order to realise $GeTe_4$ waveguides on Si, ZnSe films were required. Fabrication of chalcogenide waveguides on Si is advantageous for many reasons, to utilise the mature Si microfabrication technology, to integrate various optoelectronic components and also to provide a solution for difficulty in end-facet preparation of chalcogenide waveguides on bulk substrates by utilising well-known cleaving planes of Si. The next chapter details the deposition and characterisation of ZnSe films and waveguides on oxidised Si.

CHAPTER 5 ZnSe thin films and waveguides on Si

In this chapter, the deposition of thin films of ZnSe by RF sputtering and thermal evaporation methods is described. After optimising the deposition conditions, the deposited films were characterised and compared for their structural and morphological properties by XRD, SEM and AFM, compositional analysis by XPS and optical properties by FTIR and waveguide prism coupling. The deposited films were fabricated into rib waveguides on oxidised silicon substrates using photolithography and ion-beam etching. Propagation losses in MIR region between 2.5 μm and 3.7 μm were calculated using measurement of scattered light along the waveguide length.

In chapter 4, $GeTe_4$ waveguides on bulk ZnSe were fabricated and waveguiding was demonstrated in the MIR. As explained in that chapter, the polycrystalline bulk ZnSe substrates used is difficult to surface polish or end-face polish. Surface polishing of ZnSe substrate left many scratches on the surface and when end-face polish was attempted, it led to chipping off the edges. ZnSe substrate cleaning was another issue as chalcogenides are attacked by strong acids and bases. Cleaning of ZnSe with inappropriate solvents causes its decomposition and releases toxic gases such as hydrogen selenide. Standard acetone and isopropanol cleaning did not show significant improvement in terms of its surface cleaning. In order to avoid these problems and to utilise mature Si microfabrication technology giving potential for integration of optoelectronic components on the same chip in the future, Si was used as a convenient and cheap flat substrate to deposit chalcogenides and fabricate waveguides. Its smooth surface finish and well

known cleaving planes offer an appropriate solution to overcome problems with the chalcogenides substrate polishing.

5.1 Deposition by RF sputtering and thermal evaporation

Substrate preparation: Si (100) was used as the substrate for the fabrication of the waveguides but the following substrates were also used to deposit ZnSe for film characterisation: Si 100 (2 cm x 2cm, 4cm x 4 cm), Si with a 2.5 μm thermally grown silica layer (oxidised Si) (4 inch diameter circular wafer cut in half), Germanium (Ge) (1 inch diameter circular wafer) and microscope glass slides. Si, oxidised Si and glass slides were cleaned in Piranha (H_2O_2: H_2SO_4) solution, washed with plenty of de-ionised water and then rinsed with acetone and isopropanol (IPA) to remove any leftover acid. Ge substrates were rinsed with IPA alone. All samples were dried with dry nitrogen gas and then finally cleaned in a plasma asher (Tepla 300) in an oxygen atmosphere (O_2 600 ml/min) at 1000 W of microwave power for 15 min. This process heated the samples to ~160° C, removing residual moisture from the sample surface.

RF sputtering: Half of the cleaned substrates were used for AJA RF sputtering trials. The substrates were mounted on a platen facing down towards the target. A three inch diameter ZnSe target made by CVD was used. Substrates were heated in the sputtering chamber at 250°C in an argon atmosphere for 2 hours before starting the deposition. A sputtering pressure of 5mTorr and an RF power of 50W were used to deposit the films in an argon flow of 15sccm, resulting in deposition at a rate between 0.18 and 0.21 μm/h, during which the samples were rotated and maintained at 250 °C. After the deposition, the samples were annealed in an argon atmosphere within the chamber at 250°C for 2 hours, and the chamber was then allowed to cool down to room temperature before the samples were removed. The final ZnSe film thickness for sputtered ZnSe waveguides on oxidised silicon was 1.9 ± 0.1 μm.

Thermal evaporation: The other half of the cleaned substrates were used for thermal evaporation trials. ZnSe pieces made by CVD were placed in a tantalum (Ta) boat and the substrates were mounted on the platen, facing down towards this evaporation source. The substrates were rotated and heated to 250°C for two hours inside the chamber by a halogen lamp in vacuum before starting the deposition. After reaching a base pressure of

7 x 10^{-6} mbar the deposition was started, at a rate of 1.8-2.5 μm/h, with the substrates maintained at 250°C. In order to find a relation between the applied source current and the temperature rose for the Ta boat containing ZnSe, a thermocouple was used close to the Ta boat and the temperature was recorded at different values of current until the desired deposition rate was obtained. A calibration curve of temperature of the Ta boat raised against the applied source current is shown in Fig 5.1. It was found that for a ZnSe deposition rate of 0.5 nm/s, the Ta boat containing ZnSe was heated above ~ 550 °C which is in line with the sublimation temperature of ZnSe which is 500°C [171].

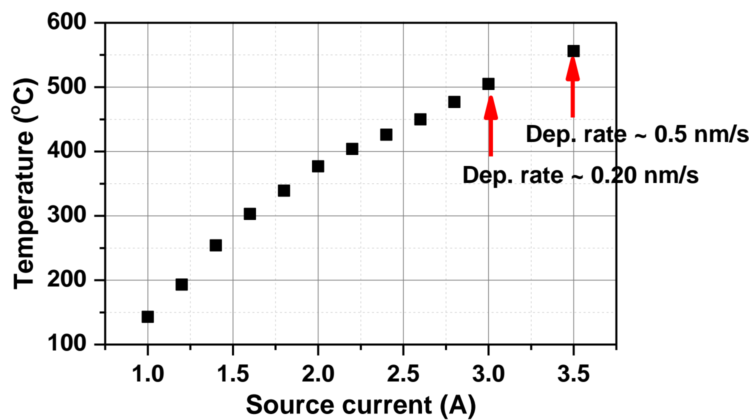

Fig. 5.1 Calibration of source current applied to Ta boat with temperature

In order to keep the chamber pressure below 5x10^{-5} mbar, the deposition was performed in steps, depositing 1 μm thick film at a time and then leaving the samples inside the chamber at 250°C for approximately one hour to allow the pressure to fall again, before starting the next deposition step. This is equivalent to vacuum annealing of the samples to release thermal stresses built during the formation of the film. Once the required thickness was achieved, the samples were annealed in the chamber at 250°C for a further additional two hours and then allowed to cool to room temperature before the chamber was opened. The samples were heated or cooled slowly in steps of 30-50 °C, to avoid peeling of the films. The final ZnSe film thickness for evaporated ZnSe waveguides on oxidised silicon was ~1.9 ± 0.2 μm.

In preliminary attempts to deposit ZnSe, room temperature deposition was performed for both sputtered and evaporated films. However, in both cases, films flaked off during subsequent processing steps. Therefore, in this work, substrate heating was used during deposition to promote adhesion of the films to substrates. The evaporated films also needed additional annealing in an external tube furnace to remove stresses for further processing of the films into waveguides. The evaporated samples were annealed in an annealing furnace at 280°C for 2 hours in argon atmosphere with a ramp up rate of 1°C/min and ramp down rate of 0.3°C/min. The sputtered films survived all the processing steps without peeling off which suggests that they had lower stresses than evaporated films probably because they were deposited 10 times more slowly than the evaporated films. Furthermore, sputtered ZnSe film samples cracked after annealing under the similar annealing conditions as the evaporated sample (shown in Fig. 5.6), and so annealing was omitted for sputtered films. Sputtered ZnSe films without further annealing and evaporated films annealed for two hours after deposition were used for final waveguide device fabrication. Fig 5.2 (a) and (b) show photographic images of ZnSe films deposited on glass substrates by sputtering and evaporation, respectively. Fig. 5.2 (c) shows an image of a bulk ZnSe plate for comparison. The deposited films resemble the bulk substrate suggests that the films have same stoichiometry.

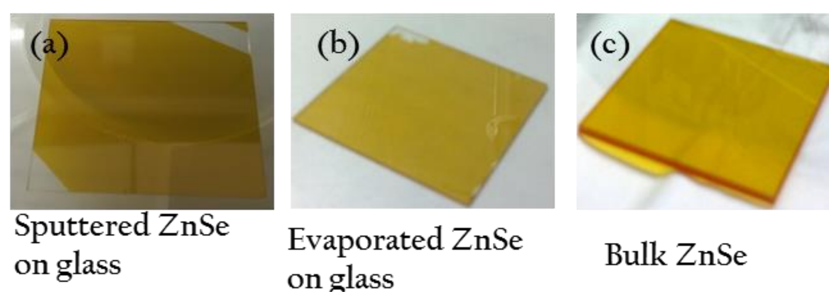

Fig. 5.2 Photographic images of bulk ZnSe substrate and ZnSe films deposited on glass substrates

Deposition of ZnSe films in thermal evaporation was extremely challenging and time consuming as the films were extremely fragile and would delaminate randomly, sometimes inside the chamber and at other times as soon as the chamber was opened and the films were exposed to ambient atmosphere. Apart from heating the substrates, different seed layers on Si, such as 50 nm thick sputtered Ta_2O_5, sputtered ZnSe,

evaporated Cr were tried and tested to promote adhesion but were not successful. On the other hand a 50 nm seed layer of evaporated CaF_2 or BaF_2 helped to promote adhesion and even when these films were stored without annealing for weeks in the cleanroom, they were intact. So in the subsequent deposition of ZnSe, a seed layer of BaF_2 is used.

5.2 Characterisation of ZnSe films

5.2.1 Crystallinity

The crystallinity of the deposited ZnSe films and commercially sourced bulk ZnSe substrates were determined by grazing incidence X-ray diffraction (GIXRD) as described in chapter 3, section 3.2.3. Fig 5.3 (a) and (c) shows the XRD patterns for annealed and unannealed sputtered and evaporated films and Fig. 5.3 (d) for bulk ZnSe substrate. Fig. 5.3 (b) and (e) shows the International Center for Diffraction Data (ICDD) XRD data for hexagonal and cubic ZnSe respectively. All the measured ZnSe samples are polycrystalline but they differ in crystal structure.

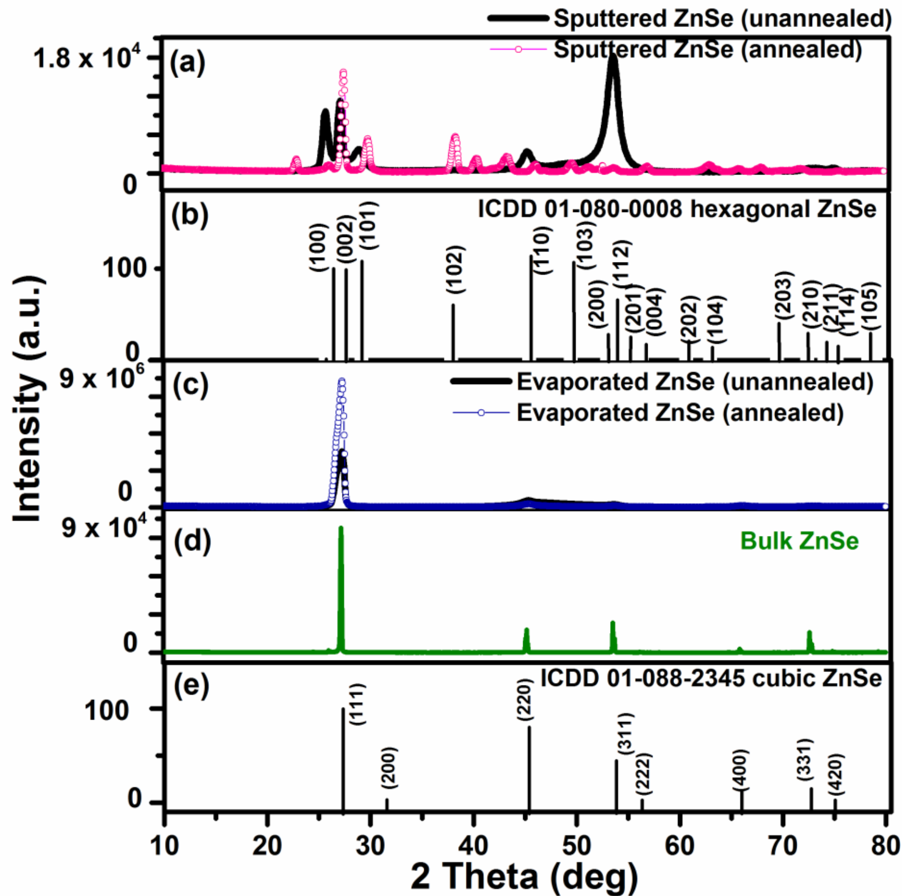

Fig. 5.3 XRD patterns of (a) sputtered, (c) evaporated and (d) bulk ZnSe along with the ICDD crystal plane data for (b) hexagonal and (e) cubic ZnSe

The sputtered ZnSe film before annealing shows mixed phases of wurtzite hexagonal and zinc blende cubic crystal structures as observed in [172], in which ZnSe was also deposited on Si by RF magnetron sputtering and the films were found to be in tensile, compressive or a mixture of both residual stresses depending on deposition pressure and power. As described above, on annealing the sputtered film, it cracked and the XRD pattern for the annealed sputtered film showed that the crystal planes of the film were randomly oriented. On the other hand the evaporated ZnSe film (before and after annealing) and the bulk ZnSe substrate show only cubic zinc blende crystal structure where the grains are mainly oriented towards the [111] axis perpendicular to the coating surface. On annealing, the crystallinity of the evaporated film was increased in the [111] plane indicating that the grains of the film aligned themselves in this plane while releasing the thermal stresses. Thermal evaporation of ZnSe is generally reported to yield cubic polycrystalline films [173, 174] in line with the results obtained.

5.2.2 Contact angle

For MIR devices, water or atmospheric moisture is highly undesirable as water has strong absorption in MIR and can lead to high losses in the material. Therefore it is important to understand the behaviour of water at the material surface. Surface wettability was measured by static contact angle measurement with deionised (DI) water on the deposited ZnSe films and on bulk ZnSe, with the angle between the water drop and the film surface being measured to define the hydrophilic or hydrophobic nature of the surface. It is governed by surface chemistry and roughness of the solid film. A hydrophilic surface has strong affinity to water therefore wets a large area of surface by maximizing the contact and has a contact angle less than 90°. A hydrophobic surface repels water and has a contact angle greater than 90°. A large contact angle or hydrophobicity is required for repelling water from the surface and to prevent contamination. Fig 5.4 shows a water drop on each of the three ZnSe surfaces. The sputtered ZnSe was found to be hydrophilic with a contact angle of 30.5° whereas bulk ZnSe is hydrophobic in nature with a contact angle of 112°. The evaporated ZnSe was found to be closer to hydrophobic in nature with a contact angle of 88°. A contact angle of 65° was reported earlier for a 280 nm thick spray pyrolysis deposited ZnSe film [175]. The results indicate that the surface of sputtered ZnSe film can form hydrogen bonds with water and is likely to pick up water/moisture from the atmosphere on its surface. Evaporated films on the other hand are less prone to moisture adsorption because of its hydrophobic like surface.

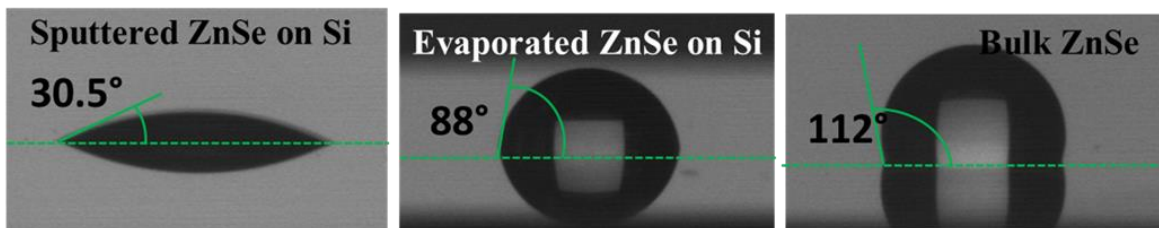

Fig. 5.4 Water contact angle for sputtered, evaporated and bulk ZnSe

5.2.3 Structure, morphology and roughness

To examine the microstructure of the films, FESEM was used. Fig. 5.5 (a) and (b) show FESEM images of the surface, and (c) of the cross-section, of a sputtered ZnSe film on Si before annealing. The grains of the sputtered film can be seen clearly and the film cross-section reveals the columnar-void structure which can be explained by Thornton's zone model [154]; a similar structure for sputtered chalcogenide films is reported in [47]. These columnar structures may also be the reason for the hydrophilic nature of the surface thereby attracting and trapping water vapor from the atmosphere. Fig. 5.5 (d), (e) and (f) show FESEM images of the surface and the cross-section of the annealed evaporated ZnSe film on Si.

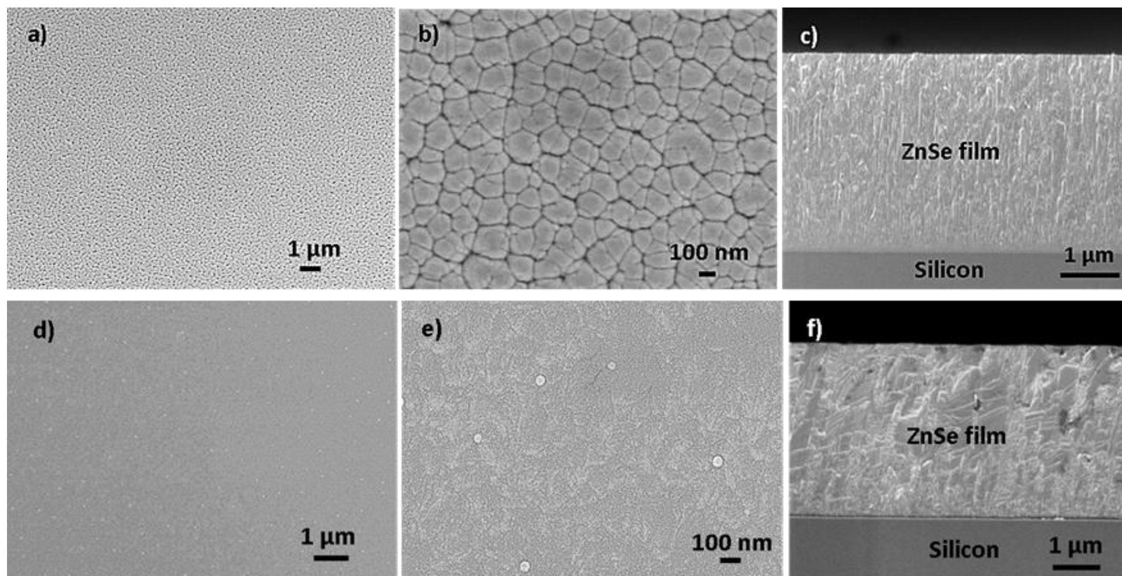

Fig. 5.5 FESEM images of (a), (b) surface and (c) cross-section of sputtered ZnSe film on Si and (d), (e) surface and (f) cross-section of the annealed evaporated film on Si

The evaporated film shows more densely packed structures than the sputtered film, but contains some random circular spots which were also observed in [176,177]. These may be caused due to 'spitting', where a sudden release of impurities such as carbon or oxygen trapped in the source material leads to ejection of larger pieces of source material towards the samples. FESEM results confirm that the evaporated films are denser than the sputtered films (Fig. 5.5 (b) and (e)). Fig. 5.5 (a) and (b) show a sputtered film after annealing, the cracks and larger separation between the grains as compared to unannealed films (Fig. 5.5 (b)) are clearly visible, so annealing was omitted for sputtered films and waveguides were fabricated with as-deposited sputtered ZnSe films.

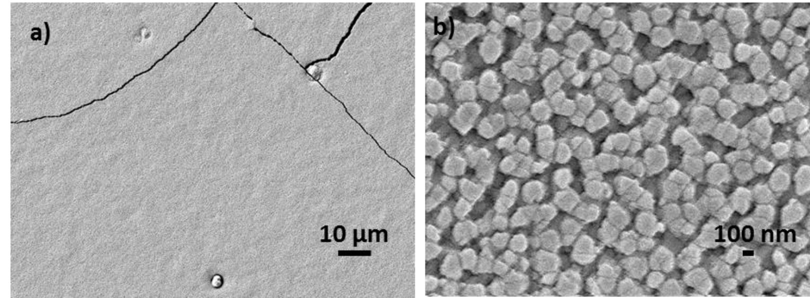

Fig. 5.6(a) and (b) FESEM images of sputtered ZnSe films after annealing

For optical applications, it is desired to have smooth surfaces to avoid scattering of light. FESEM images also indicate that the sputtered films are rougher than the evaporated films, but in order to quantify the roughness of films, an AFM in tapping mode was used. The average roughness of the sputtered and evaporated films was determined over a 2 µm x 2 µm area as shown in Fig. 5.7 (a) and (b) respectively. The average roughness of the sputtered film is ~18.5 nm and that of evaporated film was found to be ~4 nm. The high roughness of sputtered film could be due to large grains oriented in different directions that leaving grain boundaries and voids in the film as shown in FESEM results.

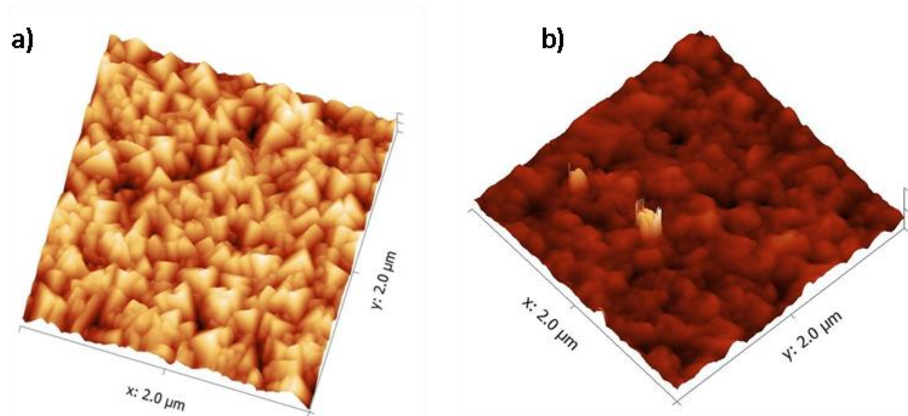

Fig. 5.7AFM images of a 2x2 µm2 scan area of (a) sputtered and (b) evaporated ZnSe on Si

5.2.4 <u>Composition</u>

Preliminary compositional analysis of both sputtered and evaporated films was performed by EDX and revealed the presence of approximately 4.5% oxygen in the sputtered film, with the atomic concentrations of Zn and Se being 44.5 at% and 51.0 at%

respectively. The presence of oxygen in the sputtered films may be due to moisture absorption from the atmosphere in the columnar structures shown in the FESEM images in Fig. 5.5. For the evaporated films, EDX gave the concentrations of Zn and Se to be 51.5 at% and 48.5 at% respectively, with no detectable oxygen.

XPS depth profiling was used to perform surface analysis on both sputtered and evaporated films. The purpose of using XPS was mainly to determine the percentage of oxygen in first few nanometers of the surface of the film. Ar ion etching was performed every one minute up to 4 depth levels. The sample surface before etching corresponds to level 0 and each minute of etching corresponds to ~ 4 nm etch depth. Fig. 5.8 shows the high resolution XPS surface spectra of core levels zinc (Zn 2p), selenium (Se 3d) and oxygen (O 1s) for both the as-deposited sputtered and the annealed evaporated films on Si. Each graph shows a dotted line corresponding to the collected data and the envelope over it (green color) shows the best fit of the peaks. An inbuilt 'Smart' background was used for fitting the peaks as shown by a line (magenta) at the bottom of the envelope curve. The smart background is an approximate method for determining the background under an XPS peak with a constraint that the background is not of greater intensity than the actual data at any point in the region [178].

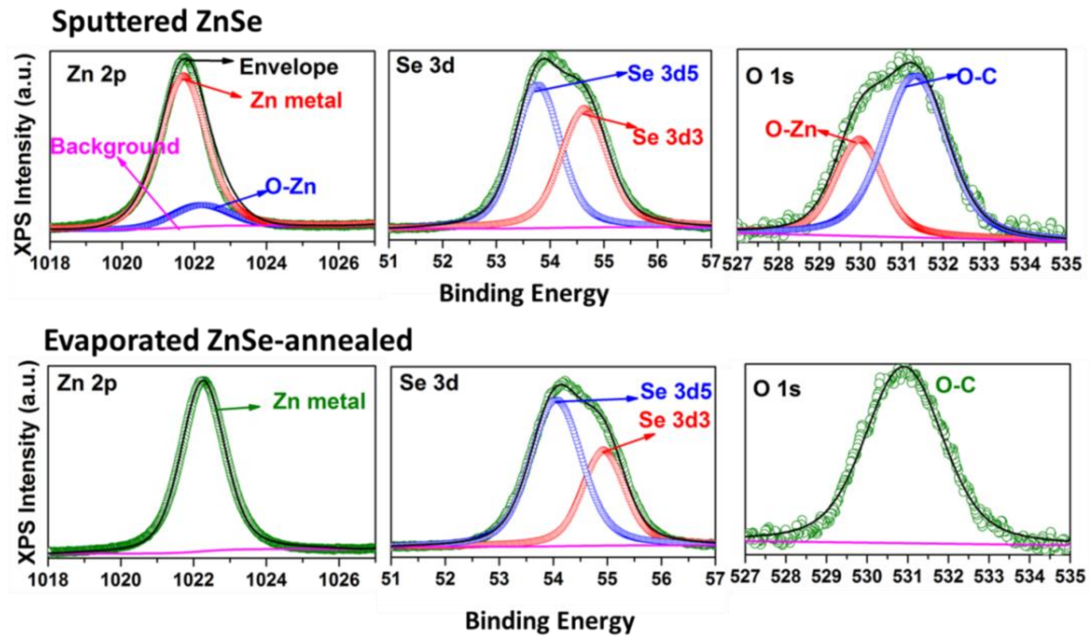

Fig. 5.8 XPS Spectra of sputtered and evaporated ZnSe films showing fitted peaks for the elements Zn, Se and O

The peaks for the individual elements were fitted for calculating the composition. The composition was determined by integrating the area under the individual peaks and normalizing these by the sensitivity factor of each element. The XPS scan of the sputtered film shows the presence of two Zn2p peaks; the high binding energy peak corresponds to zinc oxide (ZnO) whereas the low binding energy peak corresponds to metallic Zn [179].

Table 5.1 Composition analysis using XPS depth profiling of sputtered and evaporated ZnSe films

Element	**Peak B.E (eV)**	**No etch Atomic %**	**1 min etch Atomic %**	**2 min etch Atomic %**	**3 min etch Atomic %**	**4 min etch Atomic %**
Sputtered ZnSe						
Zn 2p	1022.1	30.67	36.08	44.73	45.82	46.63
Se 3d5 Se 3d3	54.8 53.95	41.82	53.67	52.0	51.34	50.80
O 1s (ZnO)	529.8	9.12	7.81	3.27	2.85	2.57
Evaporated ZnSe						
Zn 2p	1022.26	40.47	42.82	44.85	45.14	44.94
Se 3d5 Se 3d3	54.93 54.04	27.89	55.70	55.15	54.86	55.06
O 1s (O-C, metal carbonates)	531.3	18.38	2.45	-	-	-

The O1s scan shows two oxide peaks each corresponding to a bonded ZnO peak and a non-bonded oxygen peak attached to organic carbon (O-C) as shown in Fig 5.8. The evaporated ZnSe shows a single oxide peak corresponding to non-bonded oxygen along with Zn and Se. The results of depth profiling for both sputtered and evaporated films are reported in Table 5.1. The XPS analysis shows that the top layer of the sputtered ZnSe film is comprised of bonded and non-bonded oxygen as explained above. An oxide peak in the Zn 2p scan was also observed, but no evidence of the presence of SeO_2 which has absorption peaks at 2.92 μm and 3.52 μm of the MIR region [168]. After 4 min of etching, ~ 2.5% oxygen in the form of ZnO was still present in the sputtered film. On the other hand, only non-bonded oxygen was present in the first two layers of the evaporated film, so the film is free from metal bonded oxides. The results clearly indicate the evaporated film is

purer as compared to the sputtered films. The non-bonded oxygen present on the surface is due to carbon contamination while handling the samples which can be removed by cleaning the samples. The bonded oxygen which is present in the sputtered films is hard to remove as it is bonded to Zn. After confirming the oxide impurity in the films, it was important to measure the MIR transmission of the films before fabricating the waveguides.

5.2.5 Optical Transmission

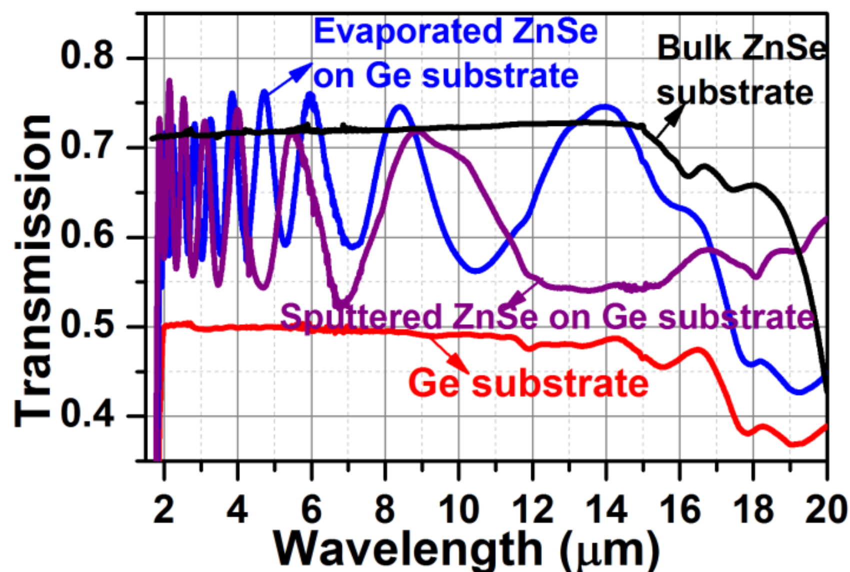

Fig. 5.9 Infrared transmission spectra of bulk ZnSe substrate, Ge substrate, sputtered and evaporated ZnSe films on Ge substrates

The optical transmission of the sputtered and evaporated ZnSe films deposited on Ge substrates and of the bulk ZnSe and Ge substrates, polished on both sides, was measured using normal incidence FTIR. A resolution of 4 cm^{-1} averaged over 64 scans over the wavelength range from 1.6 μm to 20 μm was taken. Ge was chosen as the substrate for the film transmission measurements due to its wide transparency in the mid-infrared region compared with Si. First, the transmission spectrum of a bare Ge substrate was taken with air as background, which is shown in the red curve in Figure 5.9. Then the transmission spectrum for the ZnSe film deposited on an identical Ge substrate was recorded, and the two spectra were ratioed to get the transmission spectrum of the ZnSe film alone, which is shown in the blue (evaporated) and purple (sputtered) curve in Fig. 5.10 The transmission

spectrum of bulk ZnSe substrate (black curve) with air as background is also shown in Fig. 5.9. The films are transparent up to 15-16 μm in agreement with the bulk ZnSe.

5.2.6 Optical constants

The refractive indices of the deposited films, the respective effective indices of the propagating modes and the propagation loss, at 1550nm wavelength, were determined using a Metricon™ automatic prism-coupler with a prism (code 6024.3), which can measure effective refractive index between 2.1-2.65 for the TE polarisation and between 1.85-2.42 for the TM polarisation.

For propagation loss measurement using the Metrion prism coupler, ZnSe deposited on oxidised silicon samples were used. The propagation loss was measured by exciting the guided fundamental mode and scanning a fibre along the scattered streak of light in the direction of propagation to determine the rate of decay of scattered power with respect to the distance along the waveguide. The values of refractive indices along with the error calculated as standard deviation are reported in Table 5.2 and are consistent with the values reported in the literature [180]. Propagation loss calculated from the streak of light suggests that the evaporated ZnSe films have lower loss as compared to sputtered film, which is as expected because the evaporated film has greater density and has lower surface roughness as shown by FESEM and AFM results in Fig. 5.5 and 5.7 respectively. In the literature, the losses in chalcogenide slab waveguides on oxidised silicon substrates have been demonstrated by the prism coupling method at λ = 1.064 μm to be 2, 10 and 20dB/cm for As_2S_3, $Ge_{28}Sb_{12}Se_{60}$ and $Ge_{33}As_{12}Se_{55}$ respectively [181]. The propagation losses for fully etched channel waveguides of $Ge_{23}Sb_7S_{70}$ on oxidised Si have been measured to be 2.3 dB/cm at λ = 1.55 μm [182].

Table 5.2 Prism coupling measurements for ZnSe films in TE polarisation at 1550 nm

	n	**N_{eff} of TE_{00}**	**t (nm)**	**Loss (dB/cm)**
Sputtered	2.4240 ±0.0001	2.395	1897.0 ±0.0026	1.44
Evaporated	2.4239 ±0.0001	2.418	1893.0 ±0.0797	1.16

5.3 Fabrication and characterisation of ZnSe waveguides

The sputtered and evaporated samples with 1.9 μm thick ZnSe on oxidised silicon were converted into rib waveguides by photolithography and Ar ion beam etching. S1813 photoresist was used to pattern the sample with a mask with straight channels with varying widths. A ~1.3 μm thick film of S1813 photoresist film was spun on the samples. After soft baking, the samples were exposed to UV light for 9.0 s using a 350 W Hg light source of intensity 16 mW/cm^2 and then developed using MF 319 for 45 sec. Finally, the samples were hard baked at 110°C for 1 min on a hotplate before etching. The etch rate of ZnSe was ~ 50 nm/min with a beam current of 100 mA. The waveguide characterisation was done for a rib height of 1.6 μm, slab height of 0.3 μm and a rib width ~20 μm. An SEM image of the sample cross-section is shown in Fig. 5.10 (a). Light from a tunable OPO (λ = 2.5 - 3.7 μm) was coupled into the waveguide using a ZrF_4 fiber butt-coupled to the waveguide and the guided light was recorded using a MIR camera. Fig. 5.10 (b) and (c) show the top view of infrared camera images showing the guided light emerging from the waveguide fabricated on sputtered and evaporated ZnSe film, respectively. Note that the color of the images is false and is used to represent the hot and cold regions in the frame. Once the guided mode was excited, an IR image of the scattered light along the waveguide was recorded at a position about 1-2 mm to avoid direct scattering from the end-facet. Another image of the same frame was captured with the laser off, and was used for background correction.

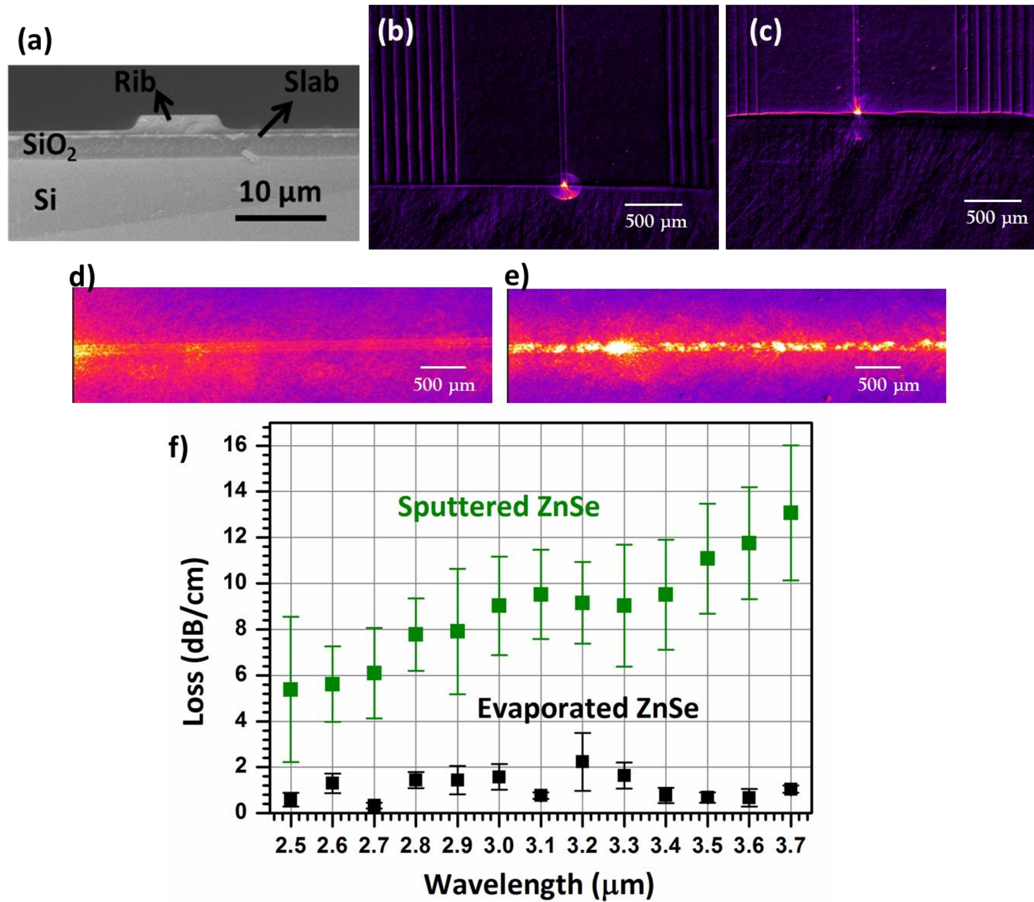

Fig. 5.10 FESEM image of cross-section of ZnSe rib waveguide on oxidised Si, (b) and (c) IR image of the guided spot emerging from the waveguide for sputtered and evaporated ZnSe waveguides, (d) and (e) IR images of the scattered light measured along the propagation length for waveguide with sputtered and evaporated ZnSe respectively at λ = 3.7 µm and (f) propagation losses in sputtered and evaporated ZnSe waveguides for 2.5 µm < λ < 3.7 µm respectively

Fig. 5.10 (d) and (e) shows the background corrected infrared images showing the streak of light of the guided mode along the propagation direction for waveguides with sputtered and evaporated ZnSe respectively. Fig. 5.10 (f) shows the propagation loss calculated by fitting an exponential to the streak of light captured between λ = 2.5 µm and 3.7 µm. The error bars represents the standard deviation between three data points at each wavelength collected from three different but nominally identical waveguides. The minimum loss calculated for the evaporated ZnSe waveguides is ~ 0.6 dB/cm at λ = 2.5 µm and 3.5-3.6 µm. The losses in the sputtered ZnSe waveguides are between 5.3 – 11.75 dB/cm. These high losses in the sputtered ZnSe waveguide could be due to inadequate film quality, higher surface roughness and large grain size as well as columnar structures that may trap oxygen from the atmosphere and hence create oxide impurities, as seen from the XPS analysis discussed above.

5.4 Conclusion

Optical quality ZnSe films were deposited using both RF magnetron sputtering and thermal evaporation. Substrate heating was used to promote adhesion of the films. Thermally evaporated ZnSe films were found to be denser and smoother than RF magnetron sputtered films. Nominally identical rib waveguides were fabricated using sputtered and evaporated ZnSe thin films on oxidized Si, and evaporated ZnSe showed lower waveguide losses at MIR wavelengths than sputtered ZnSe waveguides. Since sputtered ZnSe showed poor optical quality and higher losses as compared to evaporated ZnSe, for the subsequent waveguide device fabrication, thermal evaporation is used to produce ZnSe thin films. Evaporated ZnSe is a promising material for waveguide cores (when used with suitable cladding materials with lower RI such as CaF_2 (n~1.45) or Ta_2O_5 (n~2.1) transparent in the long wavelength region), as well as for isolation layers when used with a higher RI core material (example $GeTe_4$, n~3.3), for MIR waveguide applications. Thicker films of ZnSe as an isolation layer were deposited on Si for waveguides with $GeTe_4$ cores as discussed in chapter 6.

CHAPTER 6 $GeTe_4$ waveguides on Si

This chapter describes the $GeTe_4$ straight and bent (splitter) waveguides fabricated on Si substrates with a ZnSe isolation layer and were characterised in the MWIR (2.5-3.7 μm) wavelength region for waveguiding and propagation losses.

In chapter 5, deposition of ZnSe films was explained in detail. The motivation to deposit ZnSe films on Si was to replace the bulk ZnSe substrates with a ZnSe coated Si substrates. As explained in chapter 5, the polycrystalline bulk ZnSe used as a substrate was not only difficult to end-facet polish but also had a scratch-prone surface. Using an alternative approach of depositing both a lower cladding (isolation layer) and the core material of the waveguides on Si substrate will not only avoid polishing of the samples by utilizing the well-known cleaving planes of Si but also reduce the overall device cost as Si is a plentiful, low-cost and convenient substrate. Since chalcogenide materials do not need high temperature for processing ($GeTe_4$ was deposited at room temperature and ZnSe was deposited at 250 °C with annealing at 280°C), the preparation of chalcogenide waveguides on Si is potentially CMOS fabrication process compatible and can be easily mass-producible.

6.1 Fabrication of $GeTe_4$/ZnSe/Si waveguides

The numerical modelling in chapter 2 section 2.3 showed that a ~4 μm thick ZnSe isolation layer (n ~ 2.4) is needed in between $GeTe_4$ core (n ~ 3.3) and Si substrate (n ~ 3.5) and ~ 2.5 μm thick ZnSe film on oxidised Si, for wavelengths up to 8 μm to achieve propagation loss < 0.1 dB/cm due to light penetration into the high refractive index Si substrate.

After establishing the deposition of ZnSe films by thermal evaporation and RF sputtering (discussed in chapter 5), ~ 4.1 μm and 4.5 μm thick ZnSe films were deposited on Si substrates using evaporation and RF sputtering respectively. Nominally identical $GeTe_4$ channel waveguides were then fabricated on top of ZnSe/Si samples (on both the evaporated and sputtered ZnSe samples) by lift-off technique using a single layer recipe with an AZ2070 photoresist (chapter 3, section 3.3.2B). A ~ 6 μm thick film of AZ2070 negative photoresist was spun onto the ZnSe/Si samples. After soft baking, the samples were exposed through a photolithography mask using an i-line Hg lamp source with an exposure dose of 56 mJ/cm^2 and then post exposure baked to crosslink the exposed resist. The samples were then developed in AZ726 MF developer for 2 min to create an undercut profile. Fig. 6.1(a) shows an SEM image of photoresist undercut profile after developing. $GeTe_4$ was then deposited on these patterned samples as shown in Fig. 6.1 (b), by RF sputtering at 40W sputtering power and 15 mTorr sputtering pressure. The photoresist was then lifted off by soaking the samples in acetone overnight, leaving $GeTe_4$ channels on the ZnSe film surface. Fig. 6.1 (c) and (d) show SEM images of the top and cross-section of a $GeTe_4$ channel on a ZnSe film on Si after removing the photoresist. The trapezium like shape of the channels is due to non-directionality of the sputtering process.

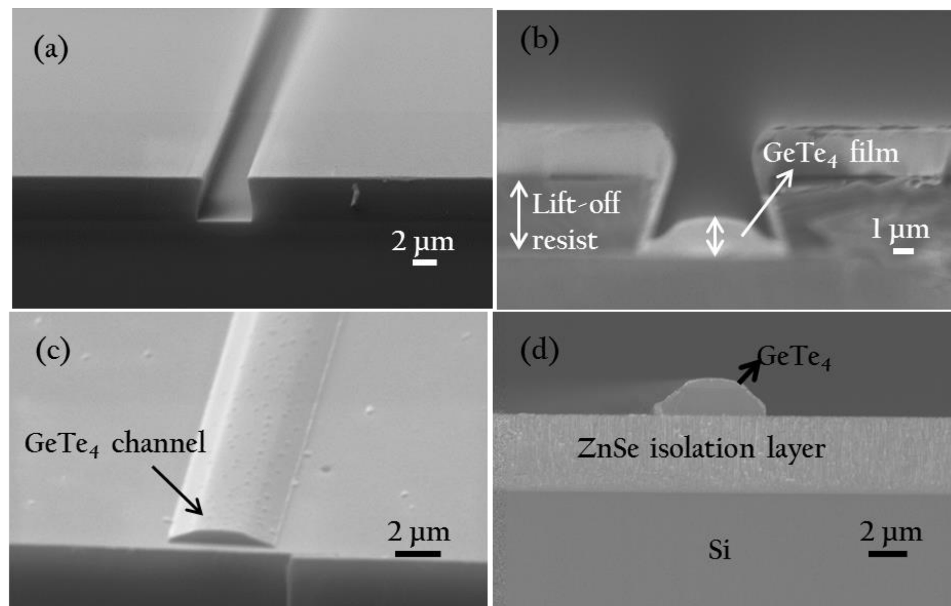

Fig. 6.1 SEM images of (a) undercut profile created by photoresist on developing, (b) $GeTe_4$ film deposited on the pattered sample, (c) and (d) top and cross-section of $GeTe_4$ channel after lifting off the photoresist

The end-facet of the sample was cleaved for coupling the light into the waveguides and to collect the light from the output end of the waveguide using a multi-mode optical fiber.

6.1.1 Design of curved structures

To characterise $GeTe_4$ waveguides on Si, for waveguiding and propagation losses, a photolithography mask was designed with various features such as, straight lines of width varying from 3 to 30 μm, splitters (1:4) of width 10 and 20 μm with a bend radius ≥ 1mm, bent L-shaped 90 ° structures with different lengths with and without gratings at the output end for collection. The idea of using splitter is to couple the light into its single input and collect the output simultaneously from four arms of different lengths either from gratings using an MIR camera or by collecting the output using an optical fiber by cleaving the sample end facets. The propagation loss can be calculated from the values of power obtained at the four outputs similar to a cut-back method. Fig. 6.2 shows a section from the mask showing a 1:4 splitter and L-shaped 90 ° bends of different lengths. The minimum bend radius used in the mask everywhere is 1 mm for every 90° bend as found by simulations performed in chapter 2 (section 2.2.2).

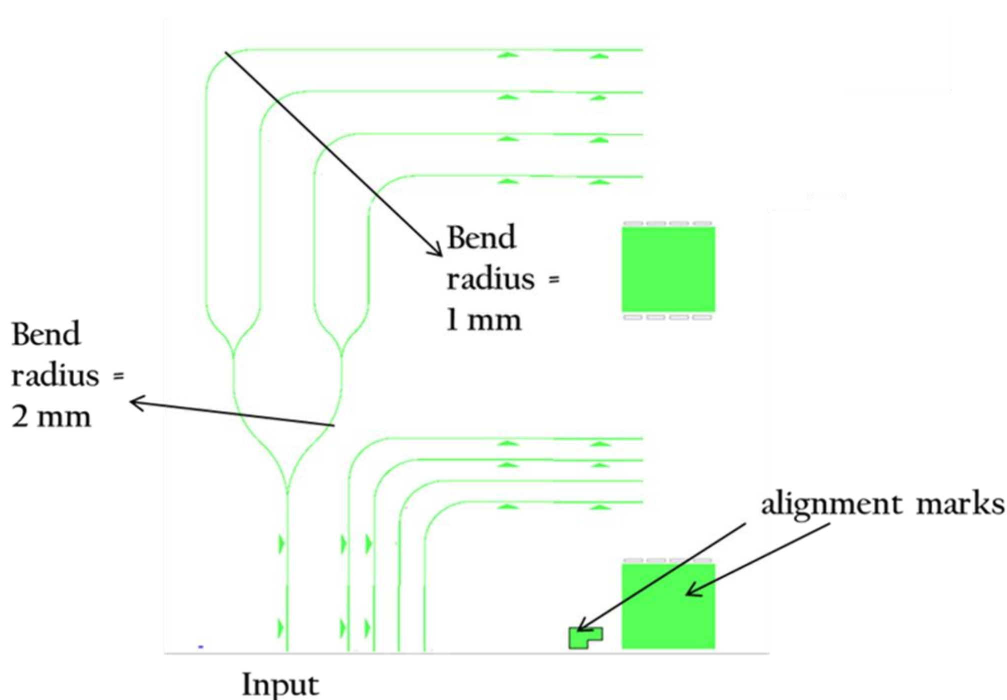

Fig. 6.2 A portion of the designed mask from L-Edit software showing the curved structures

The design in Fig. 6.2 with the $GeTe_4$ channels widths of 10 µm and 20 µm wide and 3.5 µm thick were fabricated on a 4.0 µm thick ZnSe on an oxidised Si. Microscope images of the fabricated samples are shown in Fig. 6.3 where (a) is a section of four L-shaped 90 ° bends arms and (b) is a section of a splitter arm showing the smooth lift-off process.

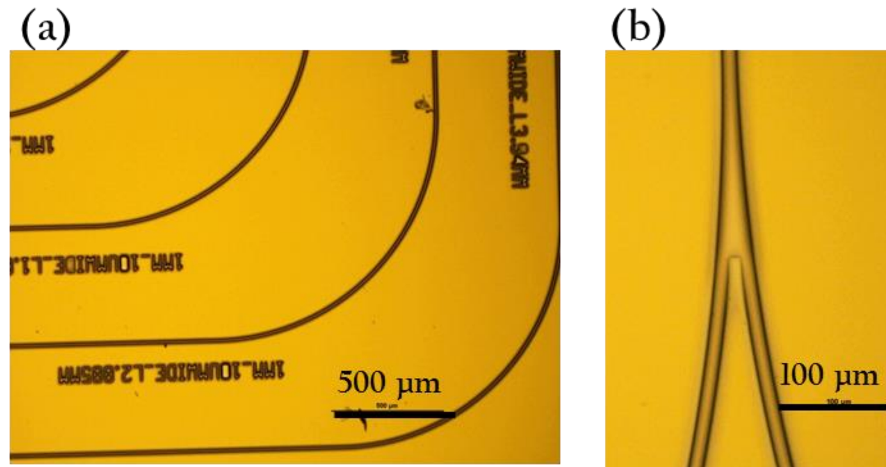

Fig. 6.3 Microscope images of (a) L-shaped bent structures, (b) a section of a splitter, (c) four output arms of a splitter with gratings at the output ends and (d) magnified image of gratings after lifting-off the photoresist

6.2 Characterisation of $GeTe_4$/ZnSe/Si waveguides

Light from a tunable OPO (λ = 2.5 - 3.7 µm) was coupled into the waveguide using a single mode ZrF_4 fiber butt-coupled with the waveguide and the guided light at the end of the waveguide and the streak of light scattered along the length of the sample was recorded using an MIR camera from above. The images were then processed to obtain the light intensity for calculation of propagation losses. For characterisation of L-shaped 90 ° bends, a multimode InF_3 fiber was used to collect the light coming out of the waveguide, the other end of the fiber was directed on to an MCT detector to record the signal using an oscilloscope. A schematic of the experimental apparatus is shown in Fig. 6.4.

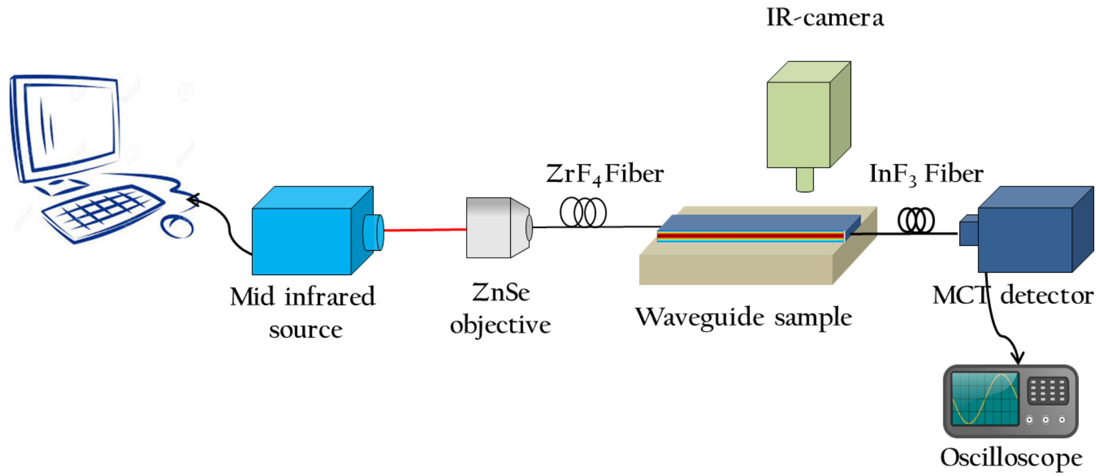

Fig. 6.4 Experimental apparatus used for waveguide characterisation in the MIR region

6.2.1 Straight waveguides

Nominally identical 20 µm wide, straight $GeTe_4$ channel waveguides of thickness 2.1 µm fabricated by lift-off technique, on both 4.1 µm thick evaporated and 4.5 µm thick sputtered ZnSe films on silicon were characterized for propagation loss using scattered light images as described above in chapter 5 (section 5.3). Both the samples were found to be guiding within wavelength regions between 2.5 - 2.7 µm and 3.4 - 3.7 µm. The streak of light scattered along the length of the sample for each of the samples was used to calculate propagation losses. Each measurement was repeated three times on an identical waveguide on the same sample.

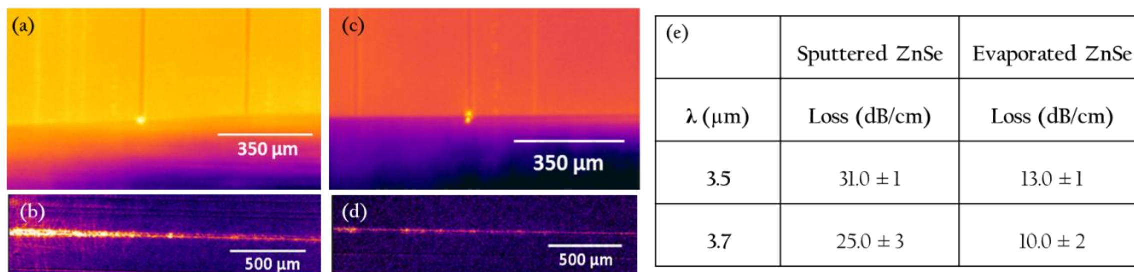

(e)	Sputtered ZnSe	Evaporated ZnSe
λ (µm)	Loss (dB/cm)	Loss (dB/cm)
3.5	31.0 ± 1	13.0 ± 1
3.7	25.0 ± 3	10.0 ± 2

Fig. 6.5 Top view of the infrared images of the output facet of a channel waveguide and scattered light measured along the propagation length of the guided mode with (a), (b) Sputtered and (c), (d) Evaporated ZnSe isolation layer on Si, at a wavelength of 3.7 µm, and (e) Propagation loss of $GeTe_4$ waveguide for sputtered and evaporated ZnSe isolation layer

The propagation loss was found to be 31±1 dB/cm and 25±3 dB/cm at λ = 3.5 and λ = 3.7 µm respectively with the sputtered ZnSe isolation layer and 13±1 dB/cm and 10±2 dB/cm

with the evaporated ZnSe isolation layer. The results are tabulated in Fig. 6.5 (e). The results obtained from propagation loss measurement confirms that the evaporated ZnSe films have lower losses as compared to the sputtered ZnSe films when used as isolation layer, in agreement with the results on ZnSe films used as waveguide core on oxidised Si described in chapter 5 section 5.3. For this reason, only evaporated ZnSe films were used as isolation layers in subsequent waveguide fabrication. The subsequent samples were prepared with evaporated ZnSe (at ~ 250°C) deposited on oxidised Si substrates with a seed layer of 50 nm BaF_2 and then annealed at 280°C. $GeTe_4$ channel waveguides were prepared by lift-off as explained in section 6.1.

6.2.2 Splitter

A 20 μm wide waveguide splitter with one input arm split into four output arms as shown in Fig. 6.2 was tested for waveguiding at λ = 3.7 μm. Fig. 6.6 shows an IR image of the guiding splitter output (only three arms are visible in the image), marked with 1, 2, 3 according to their lengths in ascending order with 1 being the shortest. The image is corrected for background. Here one can see visually that the light emerging from the shortest waveguide (1) is the brightest and the intensity of the spot decreases as the length of the splitter arm is increases as expected. The output power emerging from the arms could not be recorded as it was below the noise level of the detector. Hence propagation losses could not be calculated using the splitter.

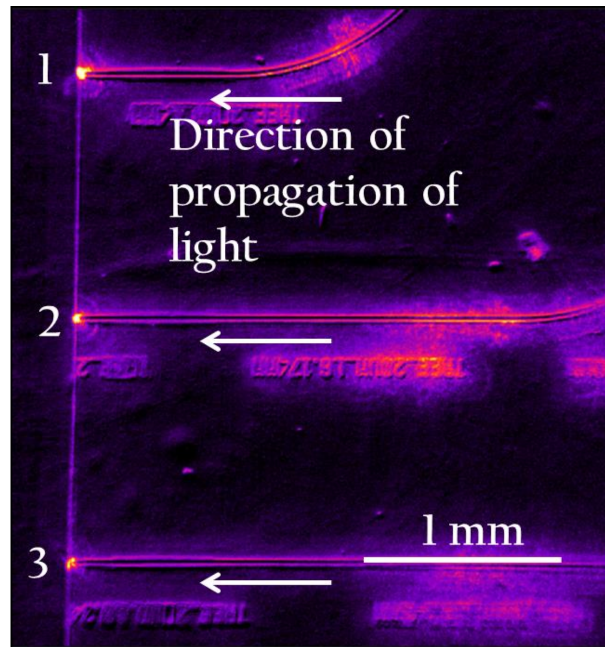

Fig. 6.6 IR image of the guiding splitter arms at λ = 3.7 μm, with the numbers marked according to ascending order of their lengths with 1 being the shortest

6.2.3 L-shaped 90 ° bent waveguides

L-shaped 90 ° bends 10 μm wide and 3.5 μm thick $GeTe_4$ structures with single input and single output and four different lengths were used to calculate propagation loss by the cut-back method over the wavelength region of 3.5-3.7 μm. These L-shaped 90 ° bends have a single 1 mm diameter bend. The sample's end facets were cleaved using a diamond scriber to allow coupling of light from a SM ZrF_4 fiber into the waveguide input facet and for collecting the light from the waveguide output facet into a MM InF_3 fiber. First, waveguiding was established in the channels by using the MIR camera from above. The output power emerging from the guided waveguide was optimised for maximum intensity at a single wavelength (λ = 3.7 μm), and the measurements were performed at three wavelengths (3.7 μm, 3.6 μm and 3.5 μm) without re-aligning the waveguide coupling at each wavelength. The output power obtained from the shortest length was used to normalise the output powers obtained for longer channel lengths. The data is plotted in Fig. 6.7 (a) and the propagation loss calculated in dB/cm is tabulated in Fig. 6.7 (b). The propagation losses are tabulated in Fig. 6.7 (b), the values are consistent with the results obtained for a 20 μm wide and 2.1 μm thick straight $GeTe_4$ channel waveguide fabricated on ZnSe/Si where the losses were calculated using streak of light measurement. Losses in a 10 μm wide waveguide are expected to be higher than that in a 20 μm wide

waveguide; however, the lower losses in 10 μm wide sample are expected to be compensated by their higher thickness as compared to the 20 μm wide waveguide. A waveguide sample with 20 μm wide $GeTe_4$ with bends was also prepared but the sample was damaged while cleaving the end-facet, so could not be tested for comparison.

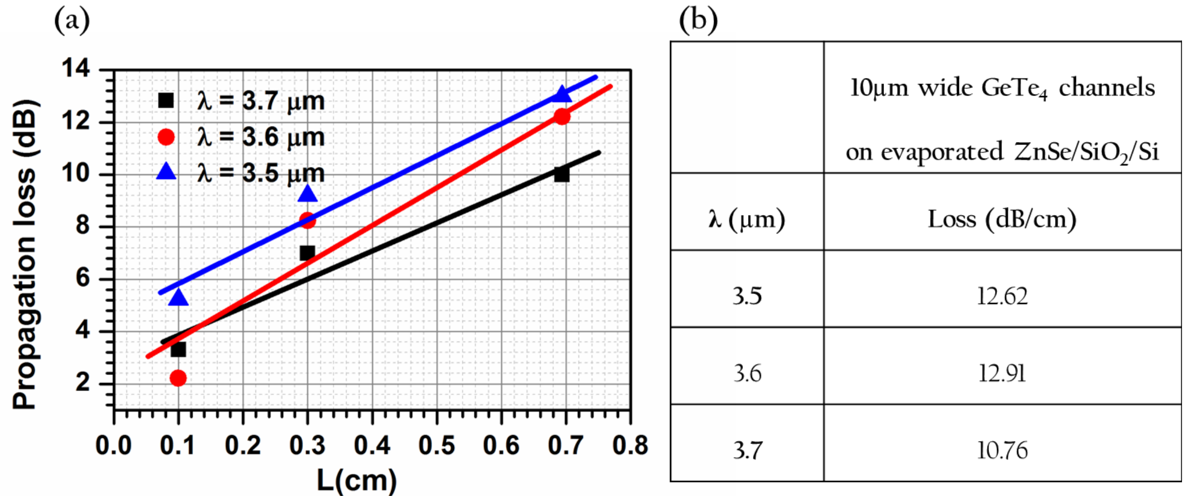

	10μm wide $GeTe_4$ channels on evaporated $ZnSe/SiO_2/Si$
λ (μm)	Loss (dB/cm)
3.5	12.62
3.6	12.91
3.7	10.76

Fig. 6.7(a) Graph and (b) table showing propagation loss calculated for $GeTe_4$ channel waveguide using cut-back method

6.3 Conclusion

$GeTe_4$ channel waveguides were fabricated on ZnSe coated Si substrates and waveguiding was demonstrated in the MWIR region of λ = 2.5-3.7 μm. A broadband absorption was observed in the wavelength region between 2.8-3.3 μm which is most likely due to OH absorption as this wavelength region is dominated by OH absorption commonly found in water and alcohols [142, 143]. Chalcogenide materials are known to be attacked by atmospheric oxygen and water, and usually need a capping layer to protect from the atmospheric moisture. Different waveguide structures with straight and curved waveguides with splitters and L-shaped 90 ° bends were fabricated and characterised for propagation losses. Propagation losses were measured using two methods, from the scattered light along the length of the sample and the equivalent cut back method. Both methods gave the similar results. Propagation losses of 10-13 dB/cm was found in the wavelength region of 3.5 – 3.7 μm. The high losses in the samples are believed to be due to oxide contamination of the $GeTe_4$ target or the films.

The samples were also tested at LWIR region, but waveguiding could not be established. This may be because, due to the low resolution of the MIR camera at longer wavelengths it was difficult to confirm if the light is emerging from the guiding channel or the substrate.

CHAPTER 7 MIR waveguide spectroscopy

In this chapter, absorption spectroscopy of water and IPA on ZnSe rib waveguides fabricated on oxidised Si are demonstrated at wavelengths between 2.5 to 3.7 μm. The theoretical model on waveguides sensing of bulk aqueous analytes discussed in chapter 2 section 2.4, is employed for these ZnSe waveguides and is compared with the experimental results.

Biological samples mostly occur in aqueous media for example proteins, lipids, nucleic acids found in blood, urine etc. Attenuated total reflection (ATR) is routinely used in combination with Fourier transform infrared spectroscopy (FTIR) to determine the analytical information of the bio-chemical species having strong absorption in MIR. However, the typical thickness of the ATR element is larger than the wavelength of propagating light and hence allows fewer reflections or bounces of the IR light along the long axis of the waveguide which limits the effective path length [115, 116]. As a result the sensitivity of the device is limited. On the other hand an integrated waveguide thickness is less than the dimension of the wavelength of light used, which helps in maximizing the evanescent field for better surface sensitivity. It is challenging to detect small amount of analyte mixed in water as water has strong absorption in the MIR region. As a model analyte, IPA mixed in water at different concentrations is tested on the ZnSe waveguide to demonstrate MIR absorption spectroscopy for the purpose of comparison of theory with experiment and to confirm the device operation.

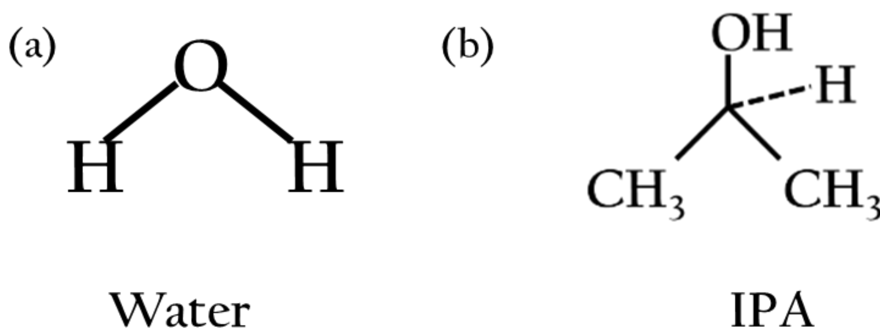

Fig. 7.1 Molecular structure of (a) Water and (b) IPA

IPA and water both have prominent IR active vibrational bands in the MIR region and are miscible in each other. The structural formulas of water and IPA are shown in Fig. 7.1. Water has absorption in the MIR region due to OH stretching and IPA shows absorption in the MIR region due to OH and CH stretching. Table 7.1 gives the different vibrational bands corresponding to symmetric and asymmetric stretching of bonds for water and IPA at specific wavelengths or frequencies [183].

Table 7.1 IR vibrational bands of water and IPA in the MIR region

Wavelength (μm)	Frequency (cm^{-1})	Vibration bands
2.63 – 3.33	3800-3000	O-H stretching of hydroxyl
3.33-3.44	3000-2900	C-H stretching (asymmetric) of CH_2 and CH_3
3.44-3.57	2900-2800	C-H stretching (symmetric) of CH_2 and CH_3

7.1 Spectroscopy in MWIR with water and IPA

To demonstrate spectroscopy of aqueous analytes (water and IPA), ZnSe rib waveguides fabricated on oxidized Si (discussed in chapter 5) were utilised. A rib waveguide with an etch depth of 1.23 μm and an after etch slab height of 2.17 μm with a rib width of 20 μm was used. An SEM image of the cleaved cross-section of the waveguide is shown in Fig. 7.2. ZnSe films were deposited by thermal evaporation and the ribs were fabricated using

photolithography and Ar^+ ion-beam etching. The sample's end facets were cleaved for fiber butt-coupling.

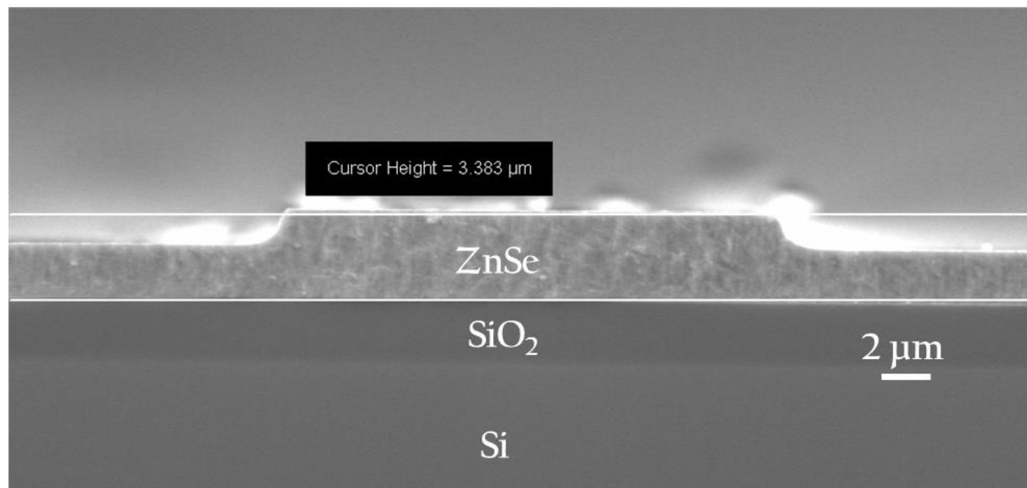

Fig. 7.2 An SEM image of the cleaved cross-section of a ZnSe rib waveguide on oxidised Si

The experimental apparatus for characterisation of waveguides is shown in Fig. 7.3. The measurements are taken as following:

1. Light from a tunable OPO operating at wavelengths between 2.5 and 3.7 µm was directed on a ZnSe objective, coupled into a single mode ZrF_4 fiber (core diameter ~ 9 µm) butt-coupled into the waveguide and the waveguide output was collected using a multimode InF_3 fiber (core diameter ~100 µm), directed onto a TE cooled MCT detector and recorded on a computer. Neutral density (ND) filters were used between the OPO and the detector or IR camera. An IR camera from above was used to first establish the guiding spot in the waveguide by using appropriate ND filters.
2. The camera was then removed and the output power was collected using the MCT detectors with appropriate ND filters.
3. A CaF_2 beam-splitter (BS) was used as a reference arm and another identical TE cooled MCT detector was used to collect the power from the BS. The beam splitter was used to correct for any wavelength or time dependence of the OPO output. Both the MCT detectors were calibrated before taking the measurements.

4. An oscilloscope was used to maximise the output power coming out of the waveguide and the BS at a fixed wavelength by adjusting the output fiber and the detector positions.

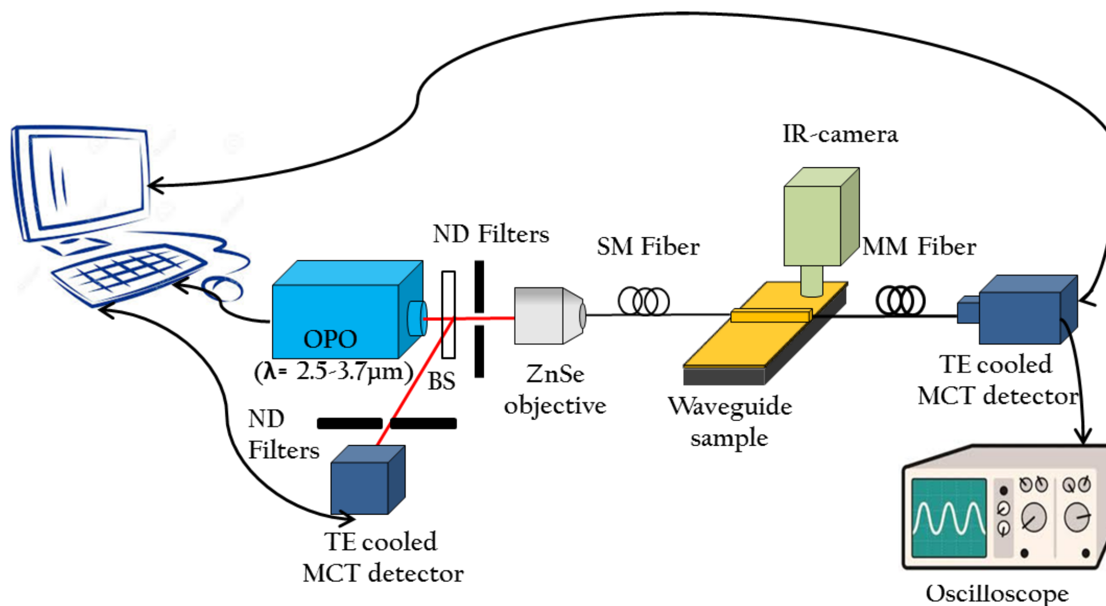

Fig. 7.3 Experimental setup for MIR waveguide spectroscopy

5. After optimising coupling into the waveguide, the wavelength was scanned from 2.5 μm to 3.7 μm with a 20 nm step size and waveguide output power was collected.
6. Then a filter paper (Fisherbrand) and a glass cover slip were carefully placed on the waveguide and an identical scan was recorded, this time with the filter paper and cover slip on the waveguide.

The waveguide and fluidic assembly is shown in Fig. 7.4 (a). The transmission of the waveguide was measured with a water superstrate and with and without the filter paper as shown in Fig. 7.4 (b) to determine whether the filter paper is interfering with the waveguide measurements. It can be concluded that the filter paper did not interfere significantly with the spectroscopic measurement and the variation in the two graphs shown in Fig. 7.4 (b) is due to the difference in path length of the water on top of the waveguide with the filter paper in and out. The advantage of using an filter paper is that it not only helps in accurately defining the path length for aqueous analyte but also

enables the measurements without the cover slip being removed for the next measurement of the same analyte concentration (when the analyte is volatile such as IPA). The aqueous analyte is dropped on the tail of filter paper coming outside the waveguide sample, so that it travels to the rib to be measured along the path exactly defined by the filter paper. The length of the filter paper was kept at ~0.3 cm. A fresh filter paper was used for each concentration.

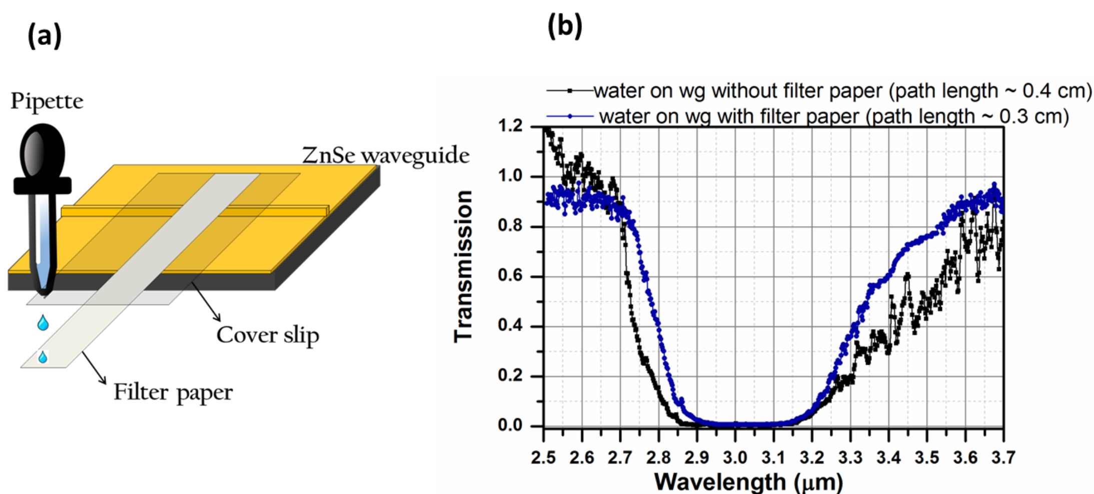

Fig. 7.4(a) Illustration of the waveguide assembly used for aqueous analyte measurement and (b) Transmission spectra of water on the surface of the waveguide with and without filter paper (FP)

Solutions of various concentrations of IPA (Fisher Scientific, > 99.8% purity) in DI water were prepared in Eppendorf tubes by mixing measured quantities of water and IPA. The solutions were introduced manually to the filter paper on the waveguide by using a pipette. All the measurements were carried out at room temperature. Six solutions of different concentration of IPA in water (100% IPA, 80%, 60%, 40%, 20% IPA in water and 100% water) were prepared for the measurement. For each concentration, two spectral scans were recorded, one of the output power from the waveguide with filter paper and cover slip on (S_0) and the other with a known IPA/water concentration on the waveguide surface (S_1). Each scan was recorded 10 times. It was found that the detector has an offset, which was subtracted from each of the 10 averaged scans of S_0 and S_1. The corresponding BS outputs without and with the analyte on (BS_0 and BS_1) were also recorded. There was no difference in the output signal measured for BS_0 and BS_1, so none of this data was used

in calculations. In order to obtain reduction in transmission (T) due to the water/IPA mixture, equation 7.1 was used.

$$T = \frac{S_1 - offset}{S_0 - offset} \qquad 7.1$$

7.2 Comparison of experimental and theoretical transmission

The transmission averaged over 10 scans representing the waveguide transmission spectrum of 100% IPA and 100% water is plotted along with their theoretical transmission obtained from the COMSOL waveguide model (discussed in chapter 2, section 2.4) using published complex refractive index for water and IPA in Fig. 7.5. The theoretical model includes the actual design of the ZnSe rib waveguide used for experiments, with real parts of ZnSe taken from the ellipsometry data from chapter 4, section 4.2.3. The real part of silica was taken from literature [139].

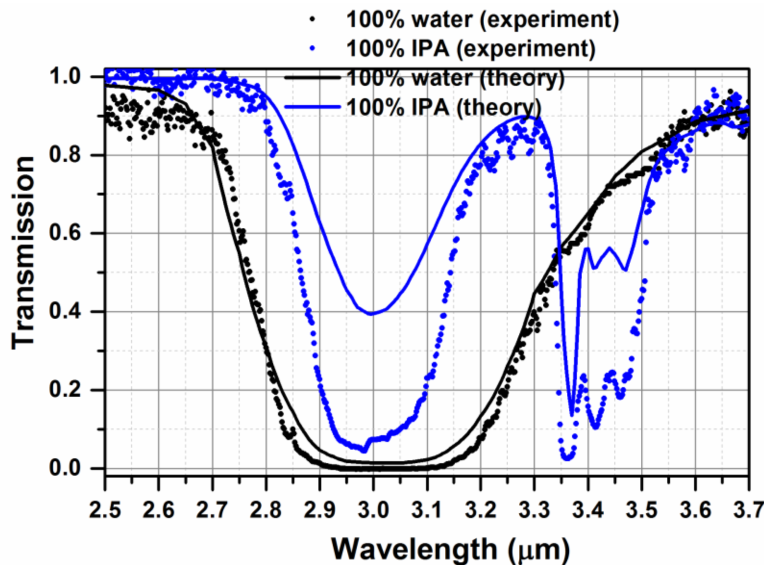

Fig. 7.5 Experimental and theoretical MIR spectra of 100% water and 100% IPA on the surface of a ZnSe waveguide

The graph in Fig. 7.5 shows good agreement for water theoretical and experimental spectra, whereas the theory and experiment for IPA deviate from each other in terms of height of the absorption peaks. This difference is believed to be due to a larger path length of IPA in experimental measurements than the theory (~ 0.3 cm) as the CS and FP used on the surface of the waveguide were of different lengths, (length of cover slip was ~

double that of the filter paper). It is possible that due to a large amount of IPA between cover slip and the filter paper, some IPA spilled out of the FP to extend to the cover slip. This is because IPA evaporates very fast and needed to be refreshed quickly during the measurements as compared to water that does not need evaporates as fast. However, the shape and positions of the IPA peaks are in agreement with each other in theory and experiment.

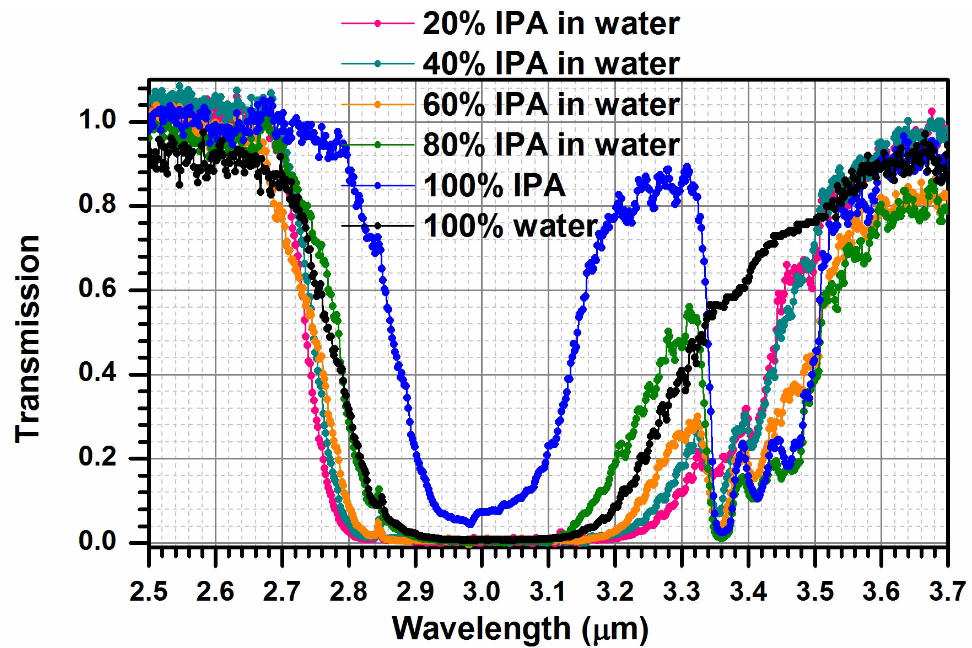

Fig. 7.6MIR transmission spectra of six different concentrations of water and IPA measured on the surface of a ZnSe waveguide (the data for 100% IPA is processed differently than other concentrations due to the nature of experiment)*

For six different concentrations of water and IPA, the transmission averaged over 10 scans representing the waveguide transmission spectrum obtained experimentally by using a waveguide setup shown in Fig. 7.4 (a), is shown in Fig. 7.6. It is to be noted that the data obtained for transmission except 100 % IPA, have been post processed by forcing the transmission to zero for the wavelengths between 2.9-3.1 μm to compensate for the experimental errors, as the absorption due to water is very high at these wavelengths and the resultant transmission is zero within the experimental error.

<u>Discussion:</u> In Fig. 7.6, MIR transmission of different concentrations of mixtures of water and IPA is shown. A broadband absorption in the wavelength between 2.8 μm and 3.3 μm

is due to the OH vibration bands present in both water and IPA. The wavelengths 3.36 µm and 3.46 µm shows absorption peaks corresponding to CH vibrations present in IPA. It can be observed from the graph that the OH absorption for 100% IPA is less wide than that of all other concentrations of IPA containing water. The CH absorption peaks of IPA also vary in their peak heights with a variation in concentration. The transmission between the wavelengths 2.5-2.6 µm in Fig. 7.6 shows deviation from unity due to the change in transmission when the waveguide was realigned for each concentration measurement.

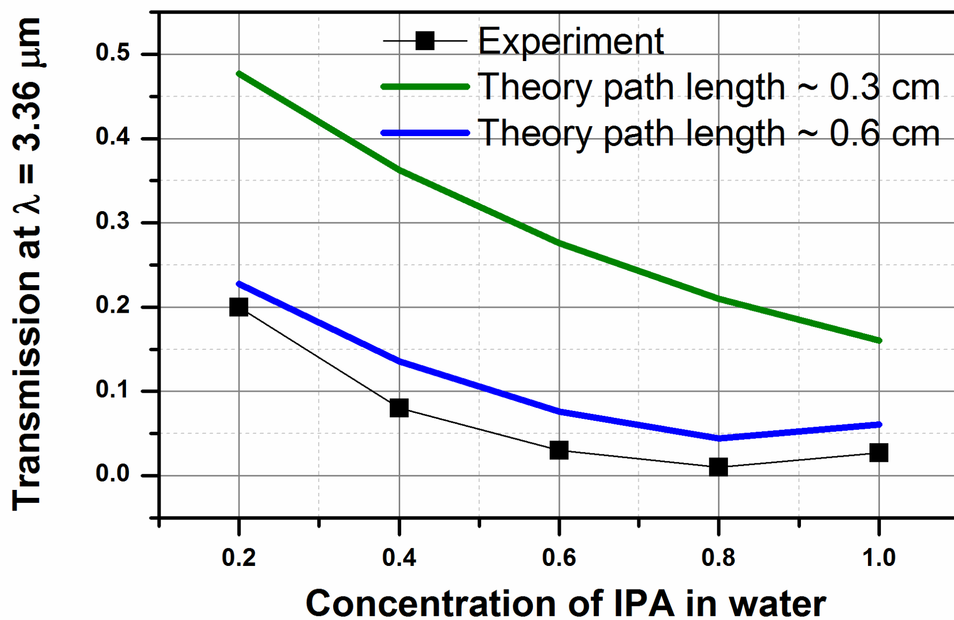

Fig. 7.7 Comparison between theory and experiment for the transmission of ZnSe rib waveguide at a wavelength of 3.36 µm vs. concentration of IPA in water

There is a prominent absorption for IPA at a wavelength of 3.36 µm. The transmission of ZnSe rib waveguide at λ = 3.36 µm for different concentrations of IPA in water as waveguide cover was simulated from the theoretical model for two different path lengths of 0.3 cm and 0.6 cm. The theoretical results were compared with the results obtained from experiment (refer Fig. 7.5). dT/dc which is defined as the sensitivity of the waveguide (Refer chapter 2, section 2.4) was calculated from Fig. 7.7 and gives a value of ~ 0.6 for the experiment and ~ 0.57 and ~ 0.46 for theoretical model calculated for a path length of 0.3 cm and 0.6 cm respectively. The results are in agreement with each other. The small discrepancy in the graph is may be due to the experimental errors.

From Fig. 7.6, it can be seen that the transmission of different concentrations of IPA measured experimentally is close to the noise level of the system. On decreasing the noise level, limit of detection of an analyte can be determined.

7.3 Conclusion

In this chapter, spectroscopy of water and IPA with six different concentrations was performed on a ZnSe rib waveguide fabricated on oxidized Si for a wavelength region of 2.5-3.7 μm. A filter paper was used to define the path length of the analyte and it was found that it does not interfere with the absorption of the analyte. This is encouraging as paper-based fluidics which is well researched can be utilized in the evanescent field sensing of the waveguides. The experimental waveguide transmission spectra of different concentrations of water and IPA were shown. The sensitivity (dT/dc) of different concentrations of IPA mixed in water as waveguide cover, for ZnSe rib waveguide was calculated from the experimental transmission spectra and is compared with the theoretical model. Theory and experimental results for sensitivity are in good agreement with each other. Theoretical and experimental waveguide transmission for water and IPA was also compared. Theory and experiment for water absorption was found to be in agreement with each other. However, some discrepancies in IPA theoretical and experimental spectra were observed mainly in the depth of the absorption peaks, which was believed to be due to experimental errors such as difference in the path length.

The overall sensitivity of the device is low because of the strong absorption of water due to OH absorption in the MIR region and is causing the optimum length of the device to be short. This is a universal problem in direct sensing of aqueous biological samples. However, there are a number of ways to remove water from the background of a measurement; 1) by drying the aqueous samples, or 2) combining MIR waveguides with microfluidics and simultaneously extracting the water out and inserting the MIR transparent solvent that has higher affinity towards the analyte into the sample chamber. For example, lipids are hydrophobic, so can be easily extracted from water and mixed in a desired solvent that does not interfere with the MIR light for the absorption spectroscopy.

CHAPTER 8 Conclusions and future directions

8.1 Overview

The aim of the research carried out in this thesis was to design, fabricate and characterise integrated optical waveguides using chalcogenide materials for application to potential evanescent field based biosensors working in the mid-infrared (MIR) region.

Initially, high refractive index (RI) contrast core and cladding materials for waveguides were selected, and two dimensional waveguides were designed using numerical modelling for single mode operation at MIR wavelengths. $GeTe_4$ film deposition by RF sputtering process was first optimised and the film structural, compositional and optical properties were evaluated before fabricating waveguides. Small cross-sections of $GeTe_4$ waveguides (thickness ~ 2.5 μm) were fabricated on bulk ZnSe substrates and were characterised for waveguiding. Due to small cross-section of the waveguides, a significant amount of input power was lost due to low input coupling efficiency and waveguiding could not be established. In order first establish the waveguiding, $GeTe_4$ channel waveguides with large cross-sections (thickness ~ 4.5 μm) were fabricated on bulk ZnSe substrates by the lift-off process, and waveguiding was established at wavelengths between 2.5 -3.7 μm and 6.4 – 9.4 μm.

An alternative approach for CMOS compatible fabrication process of chalcogenide waveguides was demonstrated where both $GeTe_4$ core and ZnSe lower cladding were deposited on silicon (Si) substrates. ZnSe film deposition on Si was optimised and ZnSe films were characterised for their structural and optical properties before utilizing them for the fabrication of waveguides. $GeTe_4$ channel waveguides with straight and bent

structures on ZnSe coated Si were fabricated and waveguiding was established in the wavelength region between 2.5 and 3.7 µm. Propagation losses at these wavelengths were measured to be between 10-13 dB/cm. In order to exploit ZnSe optical properties, ZnSe waveguides were realised on oxidised Si and waveguiding was established in the entire wavelength region from 2.5 to 3.7 µm. The propagation losses were found to be between 0.67-2.24 dB/cm.

Since the vision of this project is to utilise the chalcogenide waveguides for bio-sensing, a theoretical numerical model to design a $GeTe_4$ waveguide for maximum sensitivity of a waveguide at any wavelength of choice in the MIR region was prepared. An investigation of the effect of aqueous media on the waveguide surface, on limiting the maximum sensitivity and optimum length of a waveguide, was performed. A representative analyte was characterised on waveguide surfaces in the MIR region through its absorption spectrum, paving the path for future measurements using real biological species.

8.2 Conclusions

8.2.1 <u>$GeTe_4$ films and waveguides on bulk ZnSe substrates</u>

The waveguide core material $GeTe_4$ was deposited at room temperature by RF sputtering in an argon atmosphere. $GeTe_4$ film deposition was optimised by varying sputtering power and pressure. The deposited films were amorphous, as required to minimize scattering losses. The average surface roughness of the films was found to be 5 nm or less, sufficiently low for low-loss waveguides at MIR wavelengths. The top surface and cross-section of the deposited films was found to be smooth and dense. The $GeTe_4$ films were found to be transparent over a wavelength range of 2 − 20 µm in the MIR. The compositional analysis showed the presence of oxygen contamination in the film, which is believed to be primarily due to the Ge-O absorption, at wavelength region between 12-15 µm. A 26 µm wide and 4.6 µm thick $GeTe_4$ channel waveguide on bulk ZnSe were fabricated by lift-off method. Waveguiding was demonstrated in the 2.5−3.7 µm and 6.4−9.4 µm wavelength ranges. The mode intensity profile was extracted at a wavelength of 3.5 µm and preliminary estimates of propagation losses were reported.

8.2.2 ZnSe films and waveguides on oxidised Si

To utilise the mature Si microfabrication technology and also to provide a solution for the difficulty in end-facet preparation of $GeTe_4$ waveguides on bulk substrates, by utilising well-known cleaving planes of Si, fabrication of chalcogenide waveguides on Si was performed. In order to realise $GeTe_4$ waveguides on Si, ZnSe films were required to avoid tunnelling of light into silicon because of the high RI of Si w.r.t $GeTe_4$. Numerical modelling was used to calculate the necessary ZnSe isolation layer thickness between $GeTe_4$ and Si substrate. ZnSe films were deposited by RF sputtering and thermal evaporation in order to determine the best deposition process. It was found that a 50 nm thick seed layer of BaF2/CaF2 on Si along with substrate heating helps to promote adhesion of the ZnSe films on Si. The sputtered and evaporated films deposited at 250°C, were compared for their crystallinity, structural, compositional and optical properties. Thermally evaporated ZnSe films were found to be denser and smoother than RF magnetron sputtered films. Nominally identical rib waveguides (20 µm wide and 2.1 µm thick) were fabricated using sputtered and evaporated ZnSe thin films on oxidized Si, and evaporated ZnSe showed lower waveguide losses at MIR wavelengths than sputtered ZnSe waveguides. The propagation losses for evaporated ZnSe waveguide were found to be between 0.67-2.24 dB/cm at wavelengths between 2.5 to 3.7 µm.

8.2.3 $GeTe_4$ waveguides on Si with ZnSe isolation layer

Evaporated ZnSe films were used as isolation layers between $GeTe_4$ and Si. $GeTe_4$ channel waveguides were fabricated on ZnSe coated Si substrates by using a lift-off method and waveguiding was demonstrated in a wavelength region of 2.5-3.7 µm. A broadband absorption was observed in the wavelength region between 2.8-3.3 µm which is found to be due to OH stretching vibration caused by oxide contamination. Different structures with straight waveguides, splitters and L-shaped structures were fabricated and characterised for propagation losses. Propagation loss was measured using two methods, from the scattered light along the length of the sample and the cut back method. Both methods gave the similar results. Propagation losses of 10-13 dB/cm was found in the wavelength region of 3.5 – 3.7 µm. The high losses in the samples are believed to be due to oxide contamination of the $GeTe_4$ target or the films. Waveguiding could not be established at longer wavelengths.

8.2.4 Waveguide sensitivity model

The slab waveguide model using a bulk media as the waveguide cover was prepared to design a $GeTe_4$ waveguide for maximum sensitivity and optimum path length. The model was designed such that waveguide design can be chosen according to any wavelength of choice depending on the analyte absorption. The effect of aqueous analyte on the surface of the waveguide was evaluated to determine the limit of maximum sensitivity. The model was used to compare the experimental results obtained for the waveguide absorption spectra for mixtures of water and IPA at different concentrations.

8.2.5 Waveguide spectroscopy of IPA and water

Spectroscopy of water and IPA with six different concentrations was performed on a ZnSe rib waveguide fabricated on oxidized Si for a wavelength region between 2.5-3.7 μm. A filter paper was used to define the path length of the analyte and it was found not to be interfering with the analyte absorption in the MIR region which is encouraging for integrated waveguides with paper-based fluidics. The experimental waveguide transmission spectra of different concentrations of water and IPA were shown. The OH absorption of water and IPA at wavelengths between 2.8 μm to 3.3 μm was seen. The difference in the transmission of the IPA absorption peak for different concentrations of IPA mixed in water was clearly seen at λ = 3.36 μm and 3.46 μm. The sensitivity (dT/dc) for the IPA absorption peak at λ = 3.36 for its different concentration in water was calculated experimentally and compared with the theoretical model using the actual dimensions of the waveguide. The values of sensitivities were in good agreement with each other. Theoretical and experimental waveguide transmission for water and IPA was also compared. Theory and experiment for water and IPA absorption was found to be in agreement with each other within the limits of experimental errors.

8.3 Future directions

8.3.1 Materials

Fundamental vibrations of molecules take place in the MIR region, which has its advantages and disadvantages. On one hand it is useful for sensing clinically relevant species using their fundamental vibrations, on the other hand unwanted absorption such

as OH stretching and bending vibrations of water that cause regions of broadband absorption in the entire MIR is problematic [184]. There is a history of impurity absorption bands in chalcogenide glasses due to vibration bonds between chalcogenide elements and oxygen or hydrogen [168]. All these vibrational absorptions take place in the MIR region. Therefore, it is very important to use purified chalcogenide materials when working in the MIR region.

While selecting the materials for waveguide, their physical and chemical properties such as their thermal expansion coefficient, hardness, melting point, adhesion etc. should be kept in mind along with their optical properties. For example, while depositing ZnSe film on Si, the difference in thermal expansion coefficient between the two materials caused stresses to build up in the film as its thickness was increased. Seed layers of different materials on the substrate before depositing the films can be tried for compensation of compressive stresses, as well as annealing the films at various temperatures and ambient conditions (Ar, H_2, N_2), can be tried to study their effect on the deposited film's physical and chemical properties. It is important to ensure the mechanical strength of the waveguides before converting them into waveguides.

8.3.2 Investigation of $GeTe_4$ target and fabricated films

In this work, it was found that the as deposited $GeTe_4$ film has a Ge-O absorption which corresponds to the 12-15 μm wavelength regions which was confirmed by X-ray photoelectron spectroscopy as well as ellipsometry. MIR characterisation of the $GeTe_4$ waveguides confirmed a consistent OH absorption in the 2.8-3.3 μm wavelength regions, which was not observed in the as-deposited films. XPS results also confirmed the presence of GeO and TeO_2 in the films. XPS was performed on the pristine films, however, the fabricated waveguides may have contaminated from the various processing steps. XPS analysis could not be performed on the fabricated waveguides as the spot size of X-ray beam is few hundreds of microns, whereas waveguide width is few tens of microns. XPS can be performed on the waveguides by designing wider waveguides.

In order to investigate all the possible absorption bands in $GeTe_4$ film due to contamination and their possible origin, a compositional analysis using X-ray absorption fine structure (XAFS) and ellipsometry on the initial target material as well as a fabricated

waveguide should be performed. As structure of materials play an important role in determining their properties, a detailed study on the structure of both the $GeTe_4$ target and films can be performed for example using transmission electron microscopy (TEM).

8.3.3 Capping layer

Chalcogenide materials degrade on contact with atmosphere, water and certain chemicals. The deposited films and waveguides of chalcogenide materials need to be protected from atmosphere. While it is possible to store the fabricated samples in a desiccator under vacuum, while using the samples it is not practical. A way to protect the waveguides from atmosphere is by coating their surface with the suitable capping layers. The capping layer material should be stable in ambient and should not be affected by water or atmospheric oxygen. The sensing of analyte on the waveguide surface requires a surface exposed to air to utilise the waveguide evanescent field, but working in the MIR region is advantageous a few-tens of nanometer thick capping layer will not affect the penetration depth of evanescent field significantly.

8.3.4 ZnSe waveguides in LWIR

ZnSe waveguides on oxidised Si have been established in the whole wavelength region from 2.5-3.7 μm. Due to the silica absorption above 3.7 μm, these samples could not be utilised for long wavelength infrared (LWIR) region. The ZnSe waveguides did not show OH absorption. Since ZnSe has a high RI of ~ 2.4 and is transparent from visible to 16 μm wavelength region in the MIR, there is a potential for it to be used in LWIR with suitable under claddings. Fluoride materials such as calcium fluoride, barium fluoride have an RI ~ 1.45 and are transparent upto ~ 10 μm, which could be used as substrates or lower claddings between ZnSe and Si.

8.3.5 Gratings

Input and output gratings for coupling can be designed and used to avoid polishing problems of bulk chalcogenide or fluoride substrates, although they are not very broadband.

8.3.6 Reliable spectroscopic measurements

For waveguide spectroscopy measurement a 1: 2 splitter can be used in place of straight waveguides, to include an internal reference and improve stability.

8.3.7 Integration of waveguides with microfluidics

The waveguides can be integrated with microfluidics such as an on-chip flow-cell for the ease of introduction and regeneration of aqueous analytes on the waveguide surface. This would allow more accurate measurements as compared with dropping the liquid analyte manually using a pipette. A microfluidic system can be designed to extract water from the aqueous analyte before the analyte reaches the waveguide for measurement as in the MIR region, presence of water reduces the device sensitivity.

8.3.8 Spectroscopy of clinically relevant species

Preliminary work on aqueous analyte waveguide sensing in the MIR region has been shown in this thesis by using model analytes to establish the sensing set-up and reflect upon the practical errors and improvement in the existing set-up. Clinically relevant bio-molecules having prominent absorption in the MIR region should be tested on the waveguides and compared with a parallel sensing technique to evaluate the advantages and disadvantages of using different techniques and hence providing improvements for further action plans.

Appendix A

Dry etching of $GeTe_4$

Dry etching of $GeTe_4$ was performed to fabricate waveguides with gratings at the output arms of curved structures (splitter and L-shaped 90° bends, discussed in chapter 6) such that all the outputs can be imaged simultaneously to establish waveguiding and propagation losses at the long wavelength region (λ = 6- 12 μm). The gratings with a period of 1.4 μm and 50% duty cycle were designed for a wavelength of 7.5 μm. A feature size of 0.7 μm which is close to the limit of photolithography process is difficult to realise with a lift-off process. So etching was needed to obtain the small feature size and vertical side wall profile. 30 gratings (grating length ~ 40 μm) on each arm of the waveguides were used. A positive S18 series photoresist spin coated on the $GeTe_4$ films was used for etching procedures. Reactive ion etching (RIE) was initially used to etch $GeTe_4$ films using a combination of trifluoromethane (CHF_3) and oxygen (O_2) gases. The RF power of 200 W and a pressure of 90 mTorr was kept fixed and the concentration of the two gases was varied from (CHF_3: O_2) 90:10 to 60:40. A selectivity (photoresist etch rate/ film etch rate) of 1 and the film etch rate from 40-90 nm/ min was obtained. The process was found to be suitable for etch depth ~ 1 μm. With the increase in etching time to obtain deeply etched waveguides, the samples turned rough and the colour of the sample also changed from shiny metallic to dark brown/black. An SEM image of an etched sample using CHF_3 and O_2 is shown in Fig. A.1(a). Since chalcogenides are soft materials, the high roughness was believed to be caused by the high RF power used for etching (~ 200 W), but it was found that using a lower power of 50 W of RF power produced similar rough samples. A combination of sulphur hexafluoride (SF_6) and O_2 was also tried, which yielded high etch

rates of 750 nm/min at a power of 200 W with a selectivity of 5. This also produced rough film surfaces on etching as shown in a microscope image in Fig. A.1(b). The O_2 may have been reacting with the $GeTe_4$ material leaving it porous and rough.

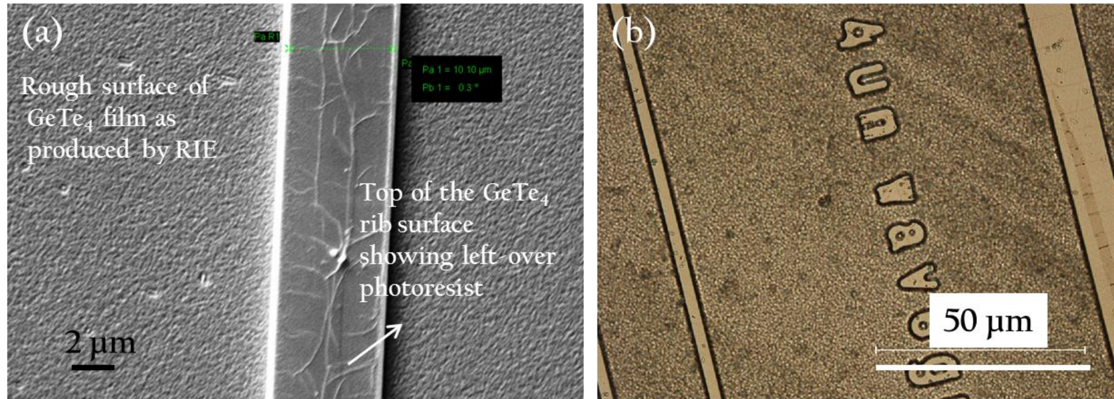

Fig. A.1 (a) CHF_3 and O_2 etched and (b) SF_6 and O_2 etched $GeTe_4$ waveguides showing the rough etched surfaces

Table A.1 ICP etch recipes for $GeTe_4$ films

Sample	**Gases (sccm)**	**Pressure (mTorr)**	**RF/ICP power (W)**	**Film etch depth (nm/min)**	**Selectivity**
(a)	Ar (20), HBr (40)	5	100/500	400	-
(b)	Ar (20), CHF_3 (40), SF_6 (20)	5	100/500	500	-
(c)	Ar (20), CHF_3 (40), SF_6 (20)	5	25/500	180	3

Since RIE on $GeTe_4$ films was troublesome and not conclusive, ICP etching was used for optimised the etching process. Here, O_2 was avoided to prevent the waveguides from unnecessary oxide contamination as it was already experienced that chalcogenide materials are not oxygen friendly. The mixture of gases and power and pressures tried in ICP etching are tabulated in table A.1. All the samples of $GeTe_4$ films were deposited on Si, to optimise the etching process, so none of the samples could be characterised for

waveguiding. The corresponding SEM images of the ICP etched samples marked (a), (b) and (c) in the Table A.1, are shown in Fig. A.2. The photoresist is not removed from the etched waveguides in the images. It can be seen that an RF power of 100W is high for the samples by looking at the damaged photoresist and rough sidewalls in Fig. A.2 (a) and (b). On reducing the RF power from 100 W to 25 W for the same gas chemistry for samples (b) and (c), a smooth and vertical side wall was obtained.

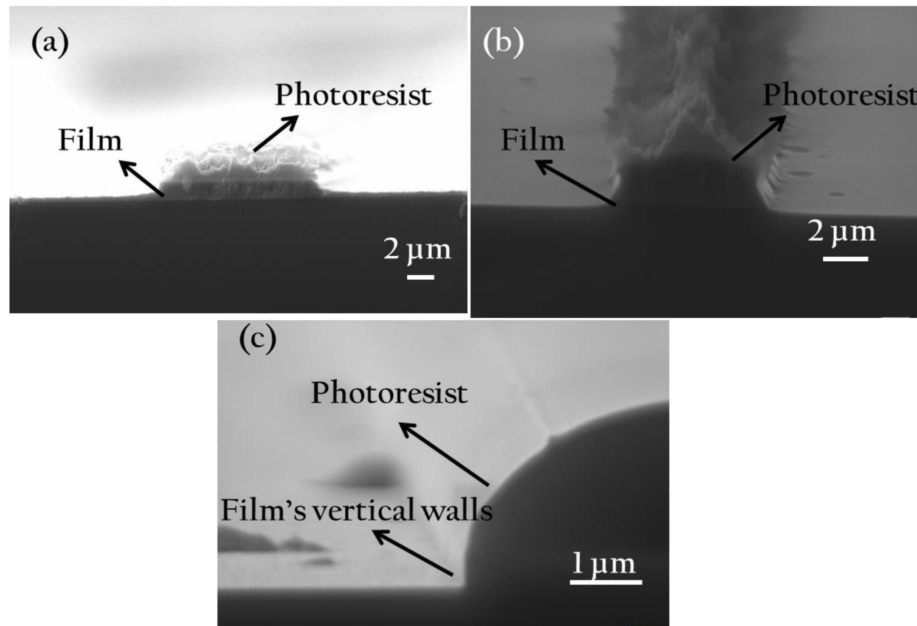

Fig. A.2 ICP etched $GeTe_4$ ribs with (a) Ar/HBr at 100W RF power, (b) and (c) $Ar/CHF_3/SF_6$ at 100W and 25W RF power respectively.

The vertical sidewalls obtained from ICP etching for the sample (c) from Fig. A.2 (c) was compared with the ion-beam etching of $GeTe_4$ with Ar ions. It can be clearly seen from Fig. A.3 (a) and (b) which shows an ICP etched and an Ar ion-beam etched $GeTe_4$ rib, that the ICP etched sample has vertical walls as required.

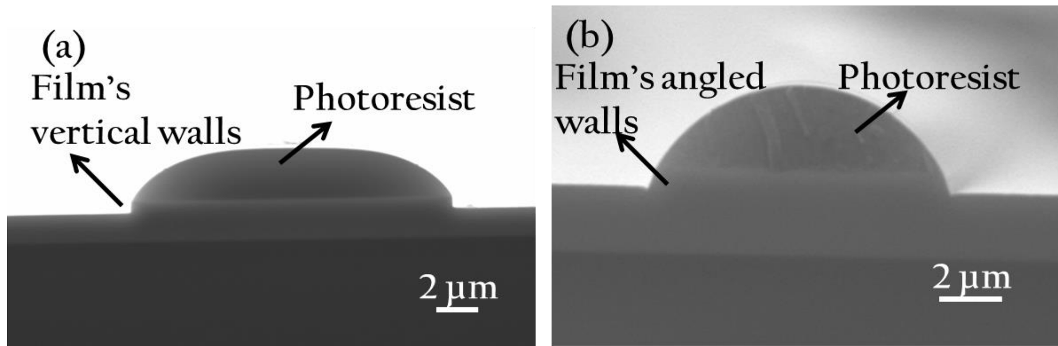

Fig. A.3 (a) An ICP etched and (b) an Ar ion-beam etched $GeTe_4$ rib waveguide

Finally, using the same ICP etching as used in sample (c) of Fig. A.2, gratings were fabricated on a $GeTe_4$ film on Si substrates. A ~ 0.5 μm thick photoresist of was used to obtain the grating features using photolithography. Fig. A.4 shows an SEM image of the fabricated gratings after etching.

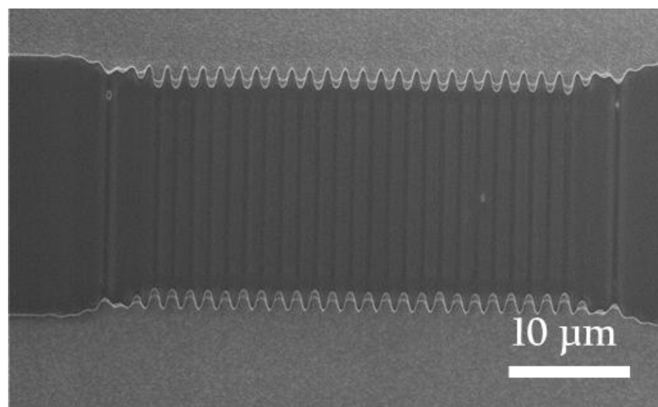

Fig. A.4 ICP etched $GeTe_4$ gratings on Si substrate

The etching process of gratings needs further optimisation as it can be seen from Fig. A.4, the grating features are not well defined. Moreover, to obtain fully etched thick $GeTe_4$ channels (thickness of > 3.0 μm) by ICP etching, a higher selectively between the photoresist and the film is required. Currently, for a photoresist of 500 nm, an etch depth obtained is 1.5 μm is obtained. An optimised waveguide with gratings can be fabricated and characterised in the MIR region in future.

Appendix B

Waveguide higher mode stripping

In this thesis waveguides with high refractive index (RI) contrast were fabricated and characterised for the mid-infrared (MIR) wavelengths. High RI contrast between the core and the substrate helps in enhancing the waveguide sensitivity by increasing the intensity of light at its surface. It allows realisation of compact devices with smaller waveguide dimensions. However, the smaller waveguide sizes impose practical difficulties in coupling of light at MIR wavelengths due to the diffraction limit at longer wavelengths. The MIR fibers generally have large core diameters (4-5 times bigger than the high RI contrast single mode (SM) waveguide core). If the waveguide core thickness is increased to enhance the coupling efficiency, the waveguide becomes multimoded which is not preferred for sensing and many other applications. There is a trade-off between better coupling efficiency and sensitivity. Depending on the application, an optimum between the two can be chosen. SM waveguides are simple to use as they support only fundamental mode, whereas multimode mode (MM) waveguides becomes complex with increasing higher order modes with phenomena such as mode beating, coupling criterion for a specific order of waveguide mode excitation. A clever way to design a MM waveguide, which supports only fundamental mode, where all the other higher order modes are absorbed by the substrate and yet provides a large dimension for better coupling efficiency is proposed. The idea is to deposit both the core and the lower cladding of a high RI contrast MM waveguide, on a substrate which has a greater RI than both the waveguide core and the lower cladding. To explain the concept, as an example, waveguide materials used in this thesis are taken, but this concept can be extended to other material systems as well. In this work, $GeTe_4$ waveguides were fabricated on ZnSe lower cladding, which has a high RI contrast ~ 0.9 (n_{GeTe4} ~ 3.3, n_{ZnSe} ~2.4). Si which has an

RI ~ 3.45 which is higher than that of both $GeTe_4$ and ZnSe is used as a substrate. The concept behind this multilayer deposition approach is that a MM $GeTe_4$ waveguide core, if deposited on Si substrate with a ZnSe isolation layer, the higher order modes of the $GeTe_4$ waveguides will get quenched or stripped by a high RI Si because the losses in the higher order modes are very high as compared to the fundamental mode.

To prove this concept, comsol numerical modelling for a slab waveguide was performed in TE polarisation with air as cover, $GeTe_4$ core, ZnSe lower cladding/isolation layer and Si substrate. The thickness of $GeTe_4$ film to support only fundamental mode is taken as 2.0 μm and the thickness of $GeTe_4$ waveguide that supports two modes is taken as 3.5 μm for calculations at a wavelength of 7.5 μm. The thickness of ZnSe isolation layer was varied to get a propagation loss in dB/cm due to higher RI Si substrate. The model includes the published real and imaginary parts of RI for Si [142], whereas only the real parts of RI, which were calculated experimentally by ellipsometry for both $GeTe_4$ and ZnSe (refer chapter 4, section 4.2.3) were taken into account. Fig. B.1 shows the propagation loss vs. ZnSe isolation layer thickness for $GeTe_4$ waveguides on Si.

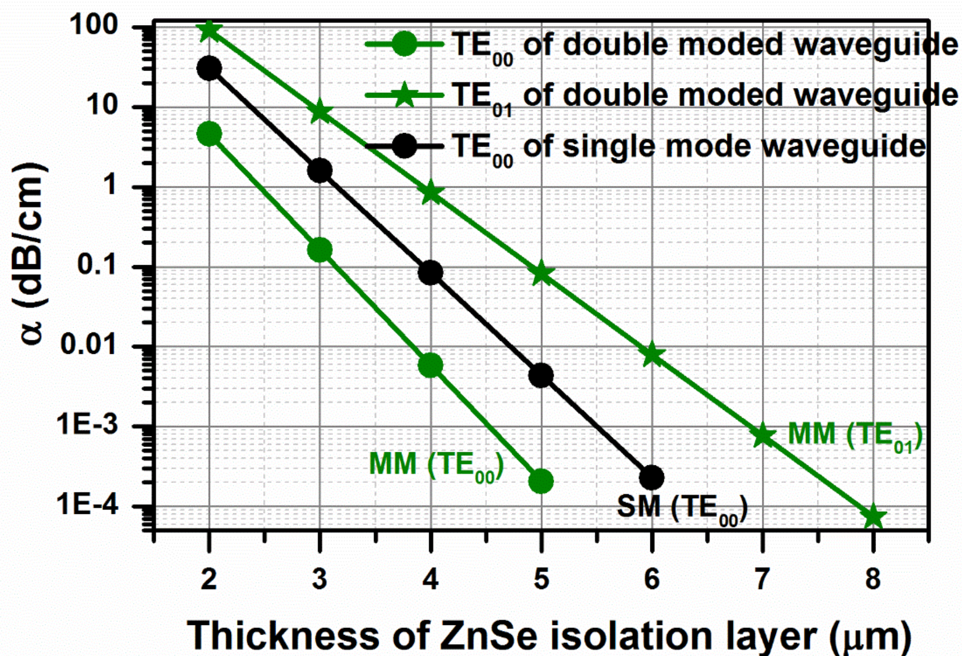

Fig. B.1 propagation loss due to Si, in $GeTe_4$ single mode (SM) and multimode (MM) waveguides vs. the thickness of ZnSe isolation layer

It can be seen from Fig. B.1 that for a SM (2.0 μm thick) $GeTe_4$ waveguide, the thickness of ZnSe layer needed is ~ 4 μm (denoted by black dots) for a loss of 0.1 dB/cm. On the other hand, the thickness of ZnSe layer needed for the fundamental mode of a 3.5 μm thick $GeTe_4$ waveguide (that supports two modes) is ~ 3.0 μm (denoted by green dots). With a 3 μm thick ZnSe layer, the losses for the higher order mode (TE_{01}) (denoted by green stars) of a double moded $GeTe_4$ waveguide increases to 10 dB/cm. Due to two orders of difference in the losses between the fundamental and the first order mode of a MM waveguide, only the fundamental mode will survive.

The concept of mode stripping not only helps in improving the coupling efficiency of the waveguide, but also reduces the thickness of isolation layer needed. In the above example, for the SM $GeTe_4$ waveguide, the thickness of ZnSe layer needed was ~ 4 μm for the losses of 0.1 dB/cm, whereas for the same value of losses, the ZnSe thickness needed was ~ 3.0 μm for a multimode waveguide. This is particularly desired when ZnSe isolation layer is used, as thicker layer of ZnSe deposited on Si flakes off due to in built thermal stresses. So if lower ZnSe thickness is needed, probably annealing of ZnSe can be avoided, which will reduce the time and cost of the device.

List of references and weblinks

[1] Shruthi, G. S., C. V. Amitha, and Blessy Baby Mathew. "Biosensors: a modern day achievement." Journal of Instrumentation Technology 2, no. 1 (2014): 26-39.

[2] Sin, Mandy LY, Kathleen E. Mach, Pak Kin Wong, and Joseph C. Liao. "Advances and challenges in biosensor-based diagnosis of infectious diseases." Expert review of molecular diagnostics 14, no. 2 (2014): 225-244.

[3] Fan, Xudong, Ian M. White, Siyka I. Shopova, Hongying Zhu, Jonathan D. Suter, and Yuze Sun. "Sensitive optical biosensors for unlabeled targets: A review." analytica chimica acta 620, no. 1 (2008): 8-26.

[4] Türker-Kaya, Sevgi, and Christian W. Huck. "A Review of Mid-Infrared and Near-Infrared Imaging: Principles, Concepts and Applications in Plant Tissue Analysis." Molecules 22, no. 1 (2017): 168.

[5] Seddon, Angela B. "A Prospective for New Mid-Infrared Medical Endoscopy Using Chalcogenide Glasses." International Journal of Applied Glass Science 2, no. 3 (2011): 177-191.

[6]http://mmrc.caltech.edu/FTIR/Nicolet/Nicolet%20Tech%20Notes/MCT%20detector%20Thermo.pdf

[7] Wang, Xiaofeng, Jarek Antoszewski, Gino Putrino, Wen Lei, Lorenzo Faraone, and Boris Mizaikoff. "Mercury–cadmium–telluride waveguides–a novel strategy for on-chip mid-infrared sensors." Analytical chemistry 85, no. 22 (2013): 10648-10652.

[8] Schwarz, Benedikt, Peter Reininger, Hermann Detz, Tobias Zederbauer, Aaron Maxwell Andrews, Werner Schrenk, and Gottfried Strasser. "Monolithically integrated mid-infrared quantum cascade laser and detector." Sensors 13, no. 2 (2013): 2196-2205.

[9] Faist, Jerome, Federico Capasso, Deborah L. Sivco, Carlo Sirtori, Albert L. Hutchinson, and Alfred Y. Cho. "Quantum cascade laser." Science 264, no. 5158 (1994): 553-556.

[10] Yao, Yu, Anthony J. Hoffman, and Claire F. Gmachl. "Mid-infrared quantum cascade lasers." Nature Photonics 6, no. 7 (2012): 432-439.

[11] Vasilyev, Sergey, Igor Moskalev, Mike Mirov, Viktor Smolsky, Sergey Mirov, and Valentin Gapontsev. "Recent Breakthroughs in Solid-State Mid-IR Laser Technology." Laser Technik Journal 13, no. 4 (2016): 24-27.

[12]https://www.crystran.co.uk/optical-materials/zinc-selenide-znse?ppc_keyword=znse&gclid=CIf1sPLYz9QCFUO-7QodwMMOzg

[13] Rogalski, A., J. Antoszewski, and L. Faraone. "Third-generation infrared photodetector arrays." Journal of applied physics 105, no. 9 (2009): 4.

[14] https://www.crystran.co.uk/optical-materials/silica-glass-sio2

[15] Vizgaitis, Jay. "Selecting Infrared Optical Materials." University of Arizona, Optics 521 (2006).

[16] J.S. Wilkinson, ’’Integrated photonics in CMOS-compatible dielectric platforms,’’ Sixth International Conference on Optical, Optoelectronic and Photonic Materials and Applications, Leeds, GB, 27 Jul - 1 Aug 2014.

[17] Z. Shaoqiang and X. Rongfu, ’’Yttrium oxide films prepared by pulsed laser deposition,’’ Journal of applied physics, 83, (2009):3842-3848.

[18] C. Charlton, A. Katzir, and B. Mizaikoff, “Infrared evanescent field sensing with quantum cascade lasers and planar silver halide waveguides,” Anal. Chem., 77, no. 14, (2005): 4398–403.

[19] Dekel, Benzion, and Abraham Katzir. "Mid-infrared diffused planar waveguides made of silver halide chloro-bromide." Applied optics 41, no. 18 (2002): 3622-3627.

[20] Dekel, B., and A. Katzir. "Graded-index mid-infrared planar optical waveguides made from silver halides." Optics letters 26, no. 20 (2001): 1553-1555.

[21] Lewi, Tomer, and Abraham Katzir. "Silver halide single-mode strip waveguides for the mid-infrared." Optics letters 37, no. 13 (2012): 2733-2735.

[22] Mashanovich, Goran Z., Milan M. Milošević, Milos Nedeljkovic, Nathan Owens, Boqian Xiong, Ee Jin Teo, and Youfang Hu. "Low loss silicon waveguides for the mid-infrared." Optics Express 19, no. 8 (2011): 7112-7119.

[23] Nedeljkovic, M., A. Z. Khokhar, Y. Hu, X. Chen, J. Soler Penades, S. Stankovic, H. M. H. Chong et al. "Silicon photonic devices and platforms for the mid-infrared." Optical Materials Express 3, no. 9 (2013): 1205-1214.

[24] Penadés, Jordi Soler, Ali Z. Khokhar, Milos Nedeljkovic, and Goran Z. Mashanovich. "Low-Loss Mid-Infrared SOI Slot Waveguides." IEEE Photonics Technology Letters 27, no. 11 (2015): 1197-1199.

[25] M. Muneeb, X. Chen, P. Verheyen, G. Lepage, S. Pathak, E. Ryckeboer, a Malik, B. Kuyken, M. Nedeljkovic, J. Van Campenhout, G. Z. Mashanovich, and G. Roelkens, “Demonstration of Silicon-on-insulator mid-infrared spectrometers operating at 3.8 μm.,” Opt. Express, 21, no. 10, (2013): 11659–69.

[26] Troia, Benedetto, Ali Z. Khokhar, Milos Nedeljkovic, Jordi Soler Penades, Vittorio MN Passaro, and Goran Z. Mashanovich. "Cascade-coupled racetrack resonators based on the Vernier effect in the mid-infrared." Optics express 22, no. 20 (2014): 23990-24003.

[27] Nedeljkovic, Milos, Stevan Stankovic, Colin J. Mitchell, Ali Z. Khokhar, Scott A. Reynolds, David J. Thomson, Frederic Y. Gardes, Callum G. Littlejohns, Graham T. Reed, and Goran Z. Mashanovich. "Mid-infrared thermo-optic modulators in SoI." IEEE Photon. Technol. Lett. 26, no. 13 (2014): 1352-1355.

[28] T. Baehr-Jones, A. Spott, R. Ilic, A. Spott, B. Penkov, W. Asher, and M. Hochberg, “Silicon-on-sapphire integrated waveguides for the mid-infrared,” Opt. Express, 18, no. 12, (2010): 12127–35.

[29] Li, Fangxin, Stuart D. Jackson, Christian Grillet, Eric Magi, Darren Hudson, Steven J. Madden, Yashodhan Moghe et al. "Low propagation loss silicon-on-sapphire waveguides for the mid-infrared." Optics express 19, no. 16 (2011): 15212-15220.

[30] Nedeljkovic, M., Khokhar, A.Z., Hu, Y., Chen, X., Penades, J.S., Stankovic, S., Chong, H.M.H., Thomson, D.J., Gardes, F.Y., Reed, G.T. and Mashanovich, G.Z., 2013. Silicon photonic devices and platforms for the mid-infrared. Optical Materials Express, 3(9), (2013): 1205-1214.

[31] Lin, Pao Tai, Vivek Singh, Yan Cai, Lionel C. Kimerling, and Anu Agarwal. "Air-clad silicon pedestal structures for broadband mid-infrared microphotonics." Optics letters 38, no. 7 (2013): 1031-1033.

[32] Yu, Fei, William J. Wadsworth, and Jonathan C. Knight. "Low loss silica hollow core fibers for 3–4 μm spectral region." Optics express 20, no. 10 (2012): 11153-11158.

[33] Tai Lin, Pao, Vivek Singh, Lionel Kimerling, and Anuradha Murthy Agarwal. "Planar silicon nitride mid-infrared devices." Applied Physics Letters 102, no. 25 (2013): 251121.

[34] Nedeljkovic, Milos, J. Soler Penadés, Colin J. Mitchell, Ali Z. Khokhar, Stevan Stankovic, T. Dominguez Bucio, Callum G. Littlejohns, Frederic Y. Gardes, and Goran Z. Mashanovich. "Surface-grating-coupled low-loss Ge-on-Si rib waveguides and multimode interferometers." IEEE Photon. Technol. Lett. 27, no. 10 (2015): 1040-1043.

[35] Y-C. Chang, V. Paeder, L. Hvozdara, J-M. Hartmann, and H. P. Herzig, “Low-loss germanium strip waveguides on silicon for the mid-infrared,” Opt. Lett., 37, no. 14, (2012): 2883–5.

[36] G. Mashanovich; C. Mitchell; J. Soler Penades; A. Khokhar; C. Littlejohns; W. Cao; Z. Qu; S. Stankovic; F. Gardes; T. B. Masaud; H. Chong; V. Mittal; S. Ganapathi; J. S. Wilkinson; A. Peacock; M. Nedeljkovic, "Germanium Mid-Infrared Photonic Devices," in Journal of Lightwave Technology , 35, no.99, (2017): 1-1.

[37] Malik, Aditya, Muhammad Muneeb, Yosuke Shimura, Joris Van Campenhout, Roger Loo, and Gunther Roelkens. "Germanium-on-silicon mid-infrared waveguides and Mach-Zehnder interferometers." In Photonics Conference (IPC), 2013 IEEE, pp. 104-105. IEEE, 2013.

[38] Brun, Mickael, Pierre Labeye, Gilles Grand, Jean-Michel Hartmann, Fahem Boulila, Mathieu Carras, and Sergio Nicoletti. "Low loss SiGe graded index waveguides for mid-IR applications." Optics express 22, no. 1 (2014): 508-518.

[39] Wang, Xiaofeng, Mikael Karlsson, Pontus Forsberg, Markus Sieger, Fredrik Nikolajeff, Lars Österlund, and Boris Mizaikoff. "." Analytical chemistry 86, no. 16 (2014): 8136-8141.

[40] Sieger, Markus, and Boris Mizaikoff. "Toward On-Chip Mid-Infrared Sensors." (2016): 5562-5573.

[41] Wang, X., M. Sieger, and B. Mizaikoff. "Toward on-chip mid-infrared chem/bio sensors using quantum cascade lasers and substrate-integrated semiconductor waveguides." Proc. SPIE, Quantum Sens. Nanophotonic Devices X 8631 (2013): 86312M.

[42] X. Wang, S-S. Kim, R. Roßbach, M. Jetter, P. Michlerb and B. Mizaikoff,“Ultra-sensitive mid-infrared evanescent field sensors combining thin-film strip waveguides with quantum cascade lasers,” Analyst, 137, no. 10, (2012): 2269–2522.

[43] Sieger, Markus, Franz Balluff, Xiaofeng Wang, Seong-Soo Kim, Lothar Leidner, Guenter Gauglitz, and Boris Mizaikoff. "On-chip integrated mid-infrared GaAs/AlGaAs Mach–Zehnder interferometer." Analytical chemistry 85, no. 6 (2012): 3050-3052.

[44] Gilles, Clément, Luis Jorge Orbe, Guillermo Carpintero, Grégory Maisons, and Mathieu Carras. "Mid-infrared wavelength multiplexer in InGaAs/InP waveguides using a Rowland circle grating." Optics express 23, no. 16 (2015): 20288-20296.

[45] V. G. Ta, N. J. Baker, L. Fu, K. Finsterbusch, M. R. E. Lamont, D. J. Moss, H. C. Nguyen, B. J. Eggleton, D. Y. Choi, S. Madden, and B. Luther-davies, "Ultrafast all-optical chalcogenide glass photonic circuits," Optics Express, 15, (2007): 9205.

[46] R. J. Gannon, "Materials for mid -infrared waveguides," Opt. Eng., 23, no. 2, (1984): 216–219.

[47] V. Balan, C. Vigreux, and A. Pradel, "Chalcogenide thin films deposited by radio-frequency sputtering," Journal of Optoelectronics and Advanced Materials, 6, no. 3, (2004): 875–882.

[48] V. Mittal, J. S. Wilkinson, and G. S. Murugan, "High-contrast $GeTe_4$ waveguides for mid-infrared biomedical sensing applications," Proc. of SPIE, Vol. 8988 89881A, Mar. 2014

[49] J.A. Frantz, J.S. Sanghera, L.B. Shaw, G. Villalobos, I. D. Aggarwal, D. W. Hewak, ''Sputtered films of Er3+ doped gallium sulphide glass,'' Materials Letters, 60, (11), (2006): 1350-1353.

[50] L. Labadie, J. E. Broquin, P. Kern, A. Pradel, and O. De Grenoble, "Selenide and telluride thick films for mid and thermal infrared applications," Journal of Optoelectronics and Advanced Materials, vol. 7, no. 5, (2005): 2625–2634.

[51] A. P. Eléonore Barthélémy, Stéphanie Albert, Caroline Vigreux ◎, "Effect of composition on the properties of Te–Ge thick films deposited by co-thermal evaporation," J. Non. Cryst. Solids, 356, (2010): 2175–2180.

[52] E. Barthélémy, C. Vigreux, G. Parent, M. Barillot, and A. Pradel, "Telluride films and waveguides for IR integrated optics," Phys. Status Solidi, 8, (2011): 2890–2894.

[53] J. Hu, V. Tarasov, N. Carlie, N.-N. Feng, L. Petit, A. Agarwal, K. Richardson, and L. Kimerling, "Si-CMOS compatible lift-off fabrication of low-loss planar chalcogenide waveguides.," Opt. Express, 15, no. 19, (2007): 11798–807.

[54] P. Němec, V. Nazabal, M. Dussauze, H.-L. Ma, Y. Bouyrie, and X.-H. Zhang, "Ga–Ge–Te amorphous thin films fabricated by pulsed laser deposition," Thin Solid Films, 531, (2013): 454–459.

[55] Y. Ruan, W. Li, R. Jarvis, N. Madsen, A. Rode, and B. L. Davies, "Fabrication and characterization of low loss rib chalcogenide waveguides made by dry etching.," Opt. Express, 12, (2004): 5140–5.

[56] O. Hashimoto, K. Uchida, S. Tokumaru, D. M. Kingsland, R. Lee, S. Helhel, O. H. Colak, R. G. Harley, G. K. Venayagamoorthy, P. Eng, S. Winter, C. G. Carrier, M. H. Weatherspoon, S. Y. Foo, H. A. Martinez, N. Photonic, G. Group, and U. Kingdom, "One-step hot embossing of optical rib waveguides in chalcogenide glasses," Microwave and optical technology letters, 50, no. 7, (2008): 1961–1963.

[57] N. S. Abdel-Moneim, C. J. Mellor, T. M. Benson, D. Furniss, and A. B. Seddon, "Fabrication of stable, low optical loss rib-waveguides via embossing of sputtered chalcogenide glass-film on glass-chip," Opt. Quantum Electron., 2014.

[58] S. Madden, T. Han, D. Bulla and B. L. Davies, "Low Loss Chalcogenide Glass Waveguides Fabricated By Thermal Nanoimprint Lithography," in Optical Society of America, OSA/OFC/NFOEC, pp. 5–7, 2010.

[59] C. Tsay, Y. Zha, and C. B. Arnold, "Solution-processed chalcogenide glass for integrated single-mode mid-infrared waveguides.," Opt. Express, 18, no. 25, (2010): 26744–53.

[60] Y. Ohmachi, "Acoustooptical Light Diffraction in Thin-Films," J. Appl. Phys., 44(9), (1973): 3928–3933.

[61] X. Gai, T. Han, A. Prasad, S. Madden, D.-Y. Choi, R. Wang, D. Bulla, and B. Luther-Davies, "Progress in optical waveguides fabricated from chalcogenide glasses," Opt. Express, 18, no. 25, (2010): 26635–46.

[62] V. V. Zigel, A. A. Litvinenko, G. K. Ulyanov, and G. A. Chalabyan, "Ultrasonic dispersive waveguide with a layer of chalcogenide glass on lithium-niobate," Soviet Phys. Acoustics-USSR, 21(1), (1975): 77.

[63] J. Fick, B. Nicolas, C. Rivero, K. Elshot, R. Irwin, K. A. Richardson, M. Fischer, and R. Vallee, "Thermally activated silver diffusion in chalcogenide thin films," Thin Solid Films, 418(2), (2002): 215–221.

[64] C. C. Huang, and D. W. Hewak, "Silver-doped germanium sulphide glass channel waveguides fabricated by chemical vapour deposition and photo-dissolution process," Thin Solid Films 500(1–2), (2006): 247–251

[65] Ramachandran, S., and S. G. Bishop. "Low loss photoinduced waveguides in rapid thermally annealed films of chalcogenide glasses." Applied physics letters 74, no. 1 (1999): 13-15.

[66] Hughes, M., W. Yang, and D. Hewak. "Fabrication and characterization of femtosecond laser written waveguides in chalcogenide glass." Applied Physics Letters 90, no. 13 (2007): 131113.

[67] Mairaj, Arshad K., Ping Hua, Harvey N. Rutt, and Daniel W. Hewak. "Fabrication and characterization of continuous wave direct UV (λ= 244~ nm) written channel waveguides in chalcogenide (Ga: La: S) glass." Journal of lightwave technology 20, no. 8 (2002): 1578.

[68] R. K. Watts, M. de Wit and W. C. Holton, "Nonoxide chalcogenide glass films for integrated optics,'' Appl. Opt. 13(10), (1974): 2329-2332.

[69] Madden, S. J., Duk-Yong Choi, D. A. Bulla, Andrei V. Rode, Barry Luther-Davies, Vahid G. Ta'eed, M. D. Pelusi, and Benjamin J. Eggleton. "Long, low loss etched As 2 S 3 chalcogenide waveguides for all-optical signal regeneration." Optics express 15, no. 22 (2007): 14414-14421.

[70] Asobe, M., H. Itoh, T. Miyazawa, and T. Kanamori. "Efficient and ultrafast all-optical switching using high Delta n, small core chalcogenide glass fibre."Electronics Letters 29, no. 22 (1993): 1966-1968.

[71] Chung, Woon Jin, Hong Seok Seo, Bong Je Park, Joon Tae Ahn, and Yong Gyu Choi. "Selenide Glass Optical Fiber Doped with Pr 3+ for U-Band Optical Amplifier." ETRI journal 27, no. 4 (2005): 411-417.

[72] Slusher, Richart E., Gadi Lenz, Juan Hodelin, Jasbinder Sanghera, L. Brandon Shaw, and Ishwar D. Aggarwal. "Large Raman gain and nonlinear phase shifts in high-purity As 2 Se 3 chalcogenide fibers." JOSA B 21, no. 6 (2004): 1146-1155.

[73] Abedin, Kazi S. "Single-frequency Brillouin lasing using single-mode As2Se3 chalcogenide fiber." Optics express 14, no. 9 (2006): 4037-4042.

[74] Ta'eed, Vahid G., Michael RE Lamont, David J. Moss, Benjamin J. Eggleton, Duk-Yong Choi, Steve Madden, and Barry Luther-Davies. "All optical wavelength conversion via cross phase modulation in chalcogenide glass rib waveguides." Optics express 14, no. 23 (2006): 11242-11247.

[75] Fu, Libin, Alexander Fuerbach, Ian CM Littler, and Benjamin J. Eggleton. "Efficient optical pulse compression using chalcogenide single-mode fibers."Applied physics letters 88, no. 8 (2006): 081116.

[76] Hô, Nicolas, Mark C. Phillips, Hong Qiao, Paul J. Allen, Kannan Krishnaswami, Brian J. Riley, Tanya L. Myers, and Norman C. Anheier. "Single-mode low-loss chalcogenide glass waveguides for the mid-infrared."Optics letters 31, no. 12 (2006): 1860-1862.

[77] Tsay, Candice, Elvis Mujagić, Christi K. Madsen, Claire F. Gmachl, and Craig B. Arnold. "Mid-infrared characterization of solution-processed As 2 S 3 chalcogenide glass waveguides." Optics express 18, no. 15 (2010): 15523-15530.

[78] Xia, Xin, Qi Chen, Candice Tsay, Craig B. Arnold, and Christi K. Madsen. "Low-loss chalcogenide waveguides on lithium niobate for the mid-infrared."Optics letters 35, no. 19 (2010): 3228-3230.

[79] Ma, Pan, Duk-Yong Choi, Yi Yu, Xin Gai, Zhiyong Yang, Sukanta Debbarma, Steve Madden, and Barry Luther-Davies. "Low-loss chalcogenide waveguides for chemical sensing in the mid-infrared." Optics express 21, no. 24 (2013): 29927-29937.

[80] Vigreux-Bercovici, C., Elodie Bonhomme, Annie Pradel, J-E. Broquin, Lucas Labadie, and Pierre Kern. "Transmission measurement at 10.6 μ m of Te 2 As 3 Se 5 rib waveguides on As 2 S 3 substrate." Applied physics letters 90, no. 1 (2007): 011110.

[81] V. Singh, P. T. Lin, N. Patel, H. Lin, L. Li, Y. Zou, F. Deng, C. Ni, J. Hu, J. Giammarco, A. P. Soliani, B. Zdyrko, I. Luzinov, S. Novak, J. Novak, P. Wachtel, S. Danto, J. D. Musgraves, K. Richardson, L. C. Kimerling, and A. M. Agarwal, "Mid-infrared materials and devices on a Si platform for optical sensing," Sci. Technol. Adv. Mater., 15, (2014): 014603.

[82] A. Gutierrez-Arroyo, E. Baudet, L. Bodiou, J. Lemaitre, I. Hardy, F. Faijan, B. Bureau, V. Nazabal and J. Charrier, "Optical characterization at 7.7 μm of an integrated platform based on chalcogenide waveguides for sensing applications in the mid-infrared,'' Opt. Express. 24, (2016): 23109-23117.

[83] C. Vigreux , E. Bonhomme, A. Pradel, "Te-rich Ge–As–Se–Te bulk glasses and films for future IR-integrated optics," J. Non. Cryst. Solids, 353, (2007): 1388–1391.

[84] C. Vigreux, E. Barthélémy, L. Bastard, J. Broquin, M. Barillot, S. Ménard, G. Parent, and A. Pradel, "Realization of single-mode telluride rib waveguides for mid-IR applications between 10 and 20 μm," 36, no. 15, (2011): 2922–2924.

[85] C. Vigreux, A. Pradel, L. Bastard, J. E. Broquin, G. Parent, X. Zhang, and M. Barillot, "All-telluride waveguides for nulling interferometry in the 6–20 μm spectral range: Fabrication and testing," 2011 13th Int. Conf. Transparent Opt. Networks, pp. 1–4, Jun. 2011.

[86] C. Vigreux, R. Escalier, A. Pradel, L. Bastard, J.-E. Broquin, X. Zhang, T. Billeton, G. Parent, M. Barillot, V. Kirschner, 'Telluride buried channel waveguides operating from 6 to 20 μm for photonic applications,' Optical Materials 49, (2015): 218–223.

[87] Katayama, K.; Matsubara, H.; Nakanishi, F.; Nakamura, T.; Doi, H.; Saegusa, A.; Mitsui; T Matsuoka, T.; Irikura, M.; Takebe, T.; Nishine, S.; Shirakawa, T. ZnSe-based white LEDs. J. Cryst. Growth, 214-215, (2000): 1064-1070.

[88] Jeon, H.; Ding,J.; Nurmikko, A. V.; Xie, W.; Grillo, D. C.; Kobayashi,M.; Gunshor, R. L.; Hua, G. C.; and Otsuka, N. Blue and green diode lasers in ZnSe-based quantum wells. Applied Physics Letters, 60, (1992): 2045-2047.

[89] Parent, D.W., Rodriguez, A., Ayers, J.E. and Jain, F.C. Photoassisted MOVPE grown (n) ZnSe/(p+) GaAs heterojunction solar cells.Solid-State Electronics, 47(4), (2003): 595-599.

[90] Lancaster, A., Cook, G., McDaniel, S.A., Evans, J., Berry, P.A., Shephard, J.D. and Kar, A.K. Mid-infrared laser emission from Fe: ZnSe cladding waveguides. Applied Physics Letters, 107(3), (2015): 031108.

[91] Gashin, P., Focsha, A., Potlog, T., Simashkevich, A.V. and Leondar, V., 1997. n-ZnSe/p-ZnTe/n-CdSe tandem solar cells. Solar energy materials and solar cells, 46(4), (1997): 323-331.

[92] Cheng, Y., Lv, J. and Chen, F. Mid-infrared ZnSe ridge waveguides fabricated by swift Kr 8+ ion irradiation combined with precise diamond blade dicing. Optical Materials Express, 5(10), (2015): 2292-2299.

[93] Macdonald, J.R., Thomson, R.R., Beecher, S.J., Psaila, N.D., Bookey, H.T. and Kar, A.K. Ultrafast laser inscription of near-infrared waveguides in polycrystalline ZnSe. Optics letters, 35(23), (2010): 4036-4038.

[94] Jia, Y. and Chen, F. Optical channel waveguides in ZnSe single crystal produced by proton implantation. Optical Materials Express, 2(4), (2012): 455-460.

[95] Riccardi, C.S., Hess, D.W. and Mizaikoff, B. Surface-modified ZnSe waveguides for label-free infrared attenuated total reflection detection of DNA hybridization. Analyst, 136(23), (2011): 4906-4911.

[96] Kühnelt, M., Leichtner, T., Kaiser, S., Hahn, B., Wagner, H.P., Eisert, D., Bacher, G. and Forchel, A. Quasiphase matched second harmonic generation in ZnSe waveguide structures modulated by focused ion beam implantation. Applied physics letters, 73, (1998): 584-586.

[97] Kim, B.G., Garmire, E., Shibata, N. and Zembutsu, S. Optical bistability and nonlinear switching due to increasing absorption in single-crystal ZnSe waveguides. Applied physics letters., 51(7), (1987): 475-477.

[98] Venkatachalam, S., Mangalaraj, D. and Narayandass, S.K. Influence of substrate temperature on the structural, optical and electrical properties of zinc selenide (ZnSe) thin films. Journal of Physics D: Applied Physics, 39(22), (2006): 4777.

[99] Kaban, I., P. Jóvári, W. Hoyer, R. G. Delaplane, and A. Wannberg. "Structural studies on Te-rich Ge–Te melts." Journal of Physics: Condensed Matter 18, no. 10 (2006): 2749.

[100] Andrikopoulos, K. S., S. N. Yannopoulos, G. A. Voyiatzis, A. V. Kolobov, Michel Ribes, and J. Tominaga. "Raman scattering study of the a-GeTe structure and possible mechanism for the amorphous to crystal transition." Journal of Physics: Condensed Matter 18, no. 3 (2006): 965.

[101] Paul Klocek (Ed.), Handbook of infrared optical materials, Marcel Dekker, Inc. 1991.

[102] https://www.el-cat.com/silicon-properties.htm

[103] https://www.crystran.co.uk/optical-materials/silica-glass-sio2

[104] A. B. Seddon, "A Prospective for New Mid-Infrared Medical Endoscopy Using Chalcogenide Glasses," Int. J. Appl. Glas. Sci., 2, no. 3, (2011): 177–191.

[105] Simona-Carmen Litescu, Eugenia D. Teodor, Georgiana-Ileana Truica, Andreia Tache and Gabriel-Lucian Radu, Fourier Transform Infrared Spectroscopy - Useful Analytical Tool for Non-Destructive Analysis, Infrared Spectroscopy - Materials Science, Engineering and Technology, Prof. Theophanides Theophile (Ed.), InTech, (2012).

[106] Schiegl, Solveig, and Nicholas J. Conard. "The Middle Stone Age sediments at Sibudu: results from FTIR spectroscopy and microscopic analyses." Southern African Humanities 18, no. 1 (2006): 149-172.

[107] Schmitt, Jürgen, and Hans-Curt Flemming. "FTIR-spectroscopy in microbial and material analysis." International Biodeterioration & Biodegradation 41, no. 1 (1998): 1-11.

[108] Pejcic, Bobby, Matthew Myers, and Andrew Ross. "Mid-infrared sensing of organic pollutants in aqueous environments." Sensors 9, no. 8 (2009): 6232-6253.

[109] W.F. Herget and J.D. Brasher, 'Remote Fourier transform infrared air pollution studies', Opt. Eng. 19, (1980): 508-514.

[110] K. Schäfer, R.Haus, J.Heland, A. Haak, 'Measurements of atmospheric trace gases by emission and absorption spectroscopy with FTIR', Ber. Bunsenges. Phys. Chem. 99, (1995): 405-411.

[111] Gilany, K., Pouracil, R. S. M., & Sadeghi, M. R., Fourier Transform Infrared Spectroscopy: A Potential Technique for Noninvasive Detection of Spermatogenesis. Avicenna Journal of Medical Biotechnology, 6(1), (2014): 47–52.

[112] Li, Qing-Bo, Xue-Jun Sun, Yi-Zhuang Xu, Li-Min Yang, Yuan-Fu Zhang, Shi-Fu Weng, Jing-Sen Shi, and Jin-Guang Wu. "Diagnosis of gastric inflammation and malignancy in endoscopic biopsies based on Fourier transform infrared spectroscopy." Clinical Chemistry 51, no. 2 (2005): 346-350.

[113] Huleihel, Mahmoud, Vitaly Erukhimovitch, Marina Talyshinsky, and Mark Karpasas. "Spectroscopic characterization of normal primary and malignant cells transformed by retroviruses." Applied spectroscopy 56, no. 5 (2002): 640-645.

[114] Kim, Yoen-Joo, Sangjoon Hahn, and Gilwon Yoon. "Determination of glucose in whole blood samples by mid-infrared spectroscopy." Applied optics 42, no. 4 (2003): 745-749.

[115] Karlowatz, M.; Kraft, M.; Mizalkoff, B., ''Simultaneous quantitative determination of benzene, toluene, and xylenes in water using mid-infrared evanescent field spectroscopy'', Anal. Chem., 76, (2014): 2643-2648.

[116] Kraft, M.; Mizaikoff, B., ''A mid-infrared sensor for monitoring of chlorinated hydrocarbons in the marine environment'', Int. J. Environ. Anal. Chem., 78, (2000): 367-383.

[117] Heinrich, P.; Wyzgol, R.; Schrader, B.; Hatzilazaru, A.; Lubbers, D.W., ''Determination of organic compounds by IR/ATR spectroscopy with polymer-coated internal reflection elements'', Appl. Spectrosc., 44, (1990): 1641-1646.

[118] Gobel, R.; Krska, R.; Kellner, R.; Seitz, R.W.; Tomellini, S.A., ''Investigation of different polymers as coating materials for IR/ATR spectroscopic trace analysis of chlorinated hydrocarbons in water'', Appl. Spectrosc., 48, (1994): 678-683.

[119] Krska, R., R. Kellner, U. Schiessl, M. Tacke, and A. Katzir. "Fiber optic sensor for chlorinated hydrocarbons in water based on infrared fibers and tunable diode lasers." Applied physics letters 63, no. 14 (1993): 1868-1870.

[120] Jakusch, M., B. Mizaikoff, R. Kellner, and A. Katzir. "Towards a remote IR fiber-optic sensor system for the determination of chlorinated hydrocarbons in water." Sensors and Actuators B: Chemical 38, no. 1-3 (1997): 83-87.

[121] Anne, Marie-Laure, Julie Keirsse, Virginie Nazabal, Koji Hyodo, Satoru Inoue, Catherine Boussard-Pledel, Hervé Lhermite et al. "Chalcogenide glass optical waveguides for infrared biosensing." Sensors 9, no. 9 (2009): 7398-7411.

[122] Hassan, Moinuddin, Xin Tan, Elissa Welle, and Ilko Ilev. "Fiber-optic Fourier transform infrared spectroscopy for remote label-free sensing of medical device surface contamination." Review of Scientific Instruments 84, no. 5 (2013): 053101.

[123] Cui, Shuo, Radwan Chahal, Yaroslav Shpotyuk, Catherine Boussard, Jacques Lucas, Frederic Charpentier, Hugues Tariel et al. "Selenide and telluride glasses for mid-infrared bio-sensing." In SPIE BiOS, pp. 893805-893805. International Society for Optics and Photonics, 2014.

[124] Kottmann, Jonas, Urs Grob, Julien M. Rey, and Markus W. Sigrist. "Mid-infrared fiber-coupled photoacoustic sensor for biomedical applications."Sensors 13, no. 1 (2013): 535-549.

[125] Singh, Vivek, Pao Tai Lin, Neil Patel, Hongtao Lin, Lan Li, Yi Zou, Fei Deng et al. "Mid-infrared materials and devices on a Si platform for optical sensing." Science and Technology of Advanced Materials 15, no. 1 (2014): 014603.

[126] Chen, Yu, Hongtao Lin, Juejun Hu, and Mo Li. "Heterogeneously integrated silicon photonics for the mid-infrared and spectroscopic sensing." ACS nano8, no. 7 (2014): 6955-6961.

[127] Schädle, Thomas, Alexander Eifert, Christine Kranz, Yosef Raichlin, Abraham Katzir, and Boris Mizaikoff. "Mid-infrared planar silver halide waveguides with integrated grating couplers." Applied spectroscopy 67, no. 9 (2013): 1057-1063.

[128] Wägli, P., Chang, Y.C., Homsy, A., Hvozdara, L., Herzig, H.P. and de Rooij, N.F., ‘’Microfluidic droplet-based liquid–liquid extraction and on-chip IR spectroscopy detection of cocaine in human saliva’’, Analytical chemistry, 85(15), (2013): 7558-7565.

[129] Gutierrez-Arroyo, Aldo, Emeline Baudet, Loïc Bodiou, Jonathan Lemaitre, Isabelle Hardy, François Faijan, Bruno Bureau, Virginie Nazabal, and Joël Charrier. "Optical characterization at 7.7 μm of an integrated platform based on chalcogenide waveguides for sensing applications in the mid-infrared."Optics express 24, no. 20 (2016): 23109-23117.

[130] Lifante, Ginés. Integrated photonics: fundamentals. J. Wiley, 2003.

[131] Ghatak, Ajoy. Inhomogeneous optical waveguides. Springer Science & Business Media, 2013.

[132] Liu, Jia-Ming. Photonic devices. Cambridge University Press, 2009.

[133] Germer, Susette. "Design and analysis of integrated waveguide structures and their coupling to silicon-based light emitters." PhD Thesis, 2014.

[134] https://courses.cit.cornell.edu/ece303/Lectures/lecture26.pdf

[135] Syms, Richard RA, and John Ritchie Cozens. Optical guided waves and devices. McGraw-Hill, 1992. (chapter 6)

[136] http://www.computational-photonics.eu/eims.html

[137] Kiyat, Isa, Atilla Aydinli, and Nadir Dagli. "High-Q silicon-on-insulator optical rib waveguide racetrack resonators." Optics express 13, no. 6 (2005): 1900-1905.

[138] Vivien, L., F. Grillot, E. Cassan, D. Pascal, S. Lardenois, A. Lupu, S. Laval, M. Heitzmann, and J-M. Fédéli. "Comparison between strip and rib SOI microwaveguides for intra-chip light distribution." Optical materials 27, no. 5 (2005): 756-762

[139] D. Chandler-Horowitz and P. M. Amirtharaj, “High-accuracy, midinfrared (450 cm−1 ≤ ω ≤ 4000 cm−1) refractive index values of silicon,’’ J. Appl. Phys. 97, (2005): 123526.

[140] Densmore, Adam, D-X. Xu, Siegfried Janz, Philip Waldron, J. Lapointe, Trevor Mischki, Gregory Lopinski, André Delâge, J. H. Schmid, and Pavel Cheben. "Sensitive label-free biomolecular detection using thin silicon waveguides." Advances in optical technologies (2008)

[141] J.S. Wilkinson, Handbook of Spectroscopy (Wiley-VCH, Germany, 2014) Günter Gauglitz and David S. Moore (Eds), Ch. 48. pp. 1620-23

[142] Hale, George M., and Marvin R. Querry. "Optical constants of water in the 200-nm to 200-μm wavelength region." Applied optics 12, no. 3 (1973): 555-563.

[143] E. Sani and A. Dell'Oro. Spectral optical constants of ethanol and isopropanol from ultraviolet to far infrared, Optical Materials 60, (2016): 137-141.

[144] Rowe, D. J., Smith, D. & Wilkinson, J. S. Complex refractive index spectra of whole blood and aqueous solutions of anticoagulants, analgesics and buffers in the mid-infrared. Sci. Rep., under review (2017).

[145] El-Agez, Taher, and Sofyan Taya. "Theoretical spectroscopic scan of the sensitivity of asymmetric slab waveguide sensors." Optica Applicata 41, no. 1 (2011): 89-95.

[146] Verma, Alka, Y. Prajapati, S. Ayub, J. P. Saini, and V. Singh. "Analytical analysis of sensitivity of optical waveguide sensor." International Journal of Engineering, Science and Technology 3, no. 3 (2011).

[147] Wang, Zilong, Stuart J. Pearce, Yung-Chun Lin, Michalis N. Zervas, Philip N. Bartlett, and James S. Wilkinson. "Power budget analysis for waveguide-enhanced Raman spectroscopy." Applied spectroscopy 70, no. 8 (2016): 1384-1391.

[148]https://www.oxford-instruments.com/products/etching-deposition-andgrowth/tools/plasmapro-100/physical-vapour-deposition-system-plasmapro-400

[149] http://www.ajaint.com/atc-orion-series-sputtering-systems.html

[150] XPS and Auger Handbook, Document Number HA600001, Issue 2 (04/03), Thermo scientific

[151] J. C. Vickerman, Surface analysis- the principal techniques, John Wiley & Sons (1997)

[152] http://www.lasurface.com

[153] Budai, Judit, István Hanyecz, Edit Szilágyi, and Zsolt Tóth. "Ellipsometric study of Si x C films: analysis of Tauc–Lorentz and Gaussian oscillator models." Thin Solid Films 519, no. 9 (2011): 2985-2988.

[154] M. Ohring, Physicsl vapour deposition, The material science of thin films, (Academic, 1991).

[155] https://www.oxford-instruments.com/products/etching-deposition-and-growth/plasma-etch-deposition/icp-etch

[156] V. Patrick. "Plasma etching." Oficina de Microfabrição: Projeto e Construção de CI's MOS (2006).

[157] J. Golden, H. Miller, D. Nawrocki, and J. Ross, "Optimization of Bi-layer Lift-Off Resist Process'' CS Mantech Technical Digest (2009).

[158] V. Mittal, L. G. Carpenter, J. C. Gates, J. S. Wilkinson and G. S. Murugan, 12th International Conference on Fiber Optics and Photonics, OSA Technical Digest (online) (Optical Society of America), T4B.4 (2014).

[159] Carpenter, Lewis G., Helen L. Rogers, Peter A. Cooper, Christopher Holmes, James C. Gates, and Peter GR Smith. "Low optical-loss facet preparation for silica-on-silicon photonics using the ductile dicing regime." Journal of Physics D: Applied Physics 46, no. 47 (2013): 475103.

[160] http://www.m2lasers.com/lasers/all-lasers/firefly-ir.aspx

[161] http://www.innpho.com/images/InnPho-Mid-IR(rev2).pdf

[162] https://www.thorlabs.com/newgrouppage9.cfm?objectgroup_id=7062

[163] http://www.vigo.com.pl/products/infrared-detectors/Photovoltaic-Detectors/pvmi-2te-series

[164] C. S. X. B.L. Zhu, J. Wang, S.J. Zhu, J. Wu, D.W. Zeng, "Optimization of sputtering parameters for deposition of Al-doped ZnO films by rf magnetron sputtering in Ar+H2 ambient at room temperature," Thin Solid Films, 520, (2012): 6963–6969.

[165] Vigreux-Bercovici, C., L. Labadie, J. E. Broquin, P. Kern, and A. Pradel. "Selenide and telluride thick films for mid and thermal infrared applications." J. Optoelectron. Adv. Mater 7, no. 5 (2005): 2625-2634.

[166] C. Vigreux , E. Bonhomme, A. Pradel, "Te-rich Ge–As–Se–Te bulk glasses and films for future IR-integrated optics," J. Non. Cryst. Solids, 353, (2007): 1388–1391.

[167] Heavens, Oliver S. Optical properties of thin solid films. Courier Corporation, 1991.

[168] J.S. Sanghera and I.D. Aggarwal, 'Infrared Fibre Optics', Textbook, chapter 4, Chalcogenide glass-based fibers.

[169] J. Golden, H. Miller, D. Nawrocki and J. Ross, CS Mantech Technical Digest (2009).

[170] Yu, Jae Su, Jeong Yi Moon, Seok Mun Choi, and Yong Tak Lee. "Fabrication of 1× 8 multimode-interference optical power splitter based on InP using CH4/H2 reactive ion etching." Japanese Journal of Applied Physics 40, no. 2R (2001): 634.

[1710] www.dow.com/assets/attachments/.../gt/.../cvd_zinc_selenide/.../cvd_zinc_selenide.pdf

[172] A. Rizzo, M. A. Tagliente, L. Caneve and S. Scaglione, "The influence of the momentum transfer on the structural and optical properties of ZnSe thin films prepared by RF magnetron sputtering,'' Thin Solid Films. 368(1),(2000): 8-14.

[173] S. Venkatachalam, D. Mangalaraj and S. K. Narayandass, “Influence of substrate temperature on the structural, optical and electrical properties of zinc selenide (ZnSe) thin films,’’ J. Phys. D: Appl. Phys. 39(22), (2006) 4777.

[174] S. Venkatachalam, D. Mangalaraj, S. K. Narayandass, S. Velumani, P. Schabes-Retchkiman and J. A. Ascencio, “Structural studies on vacuum evaporated ZnSe/p-Si Schottky diodes,’’ Mater. Chem. Phys. 103(2), (2007): 305-311.

[175] G. M. Lohar, S. K. Shinde and V. J. Fulari, “Structural, morphological, optical and photoluminescent properties of spray-deposited ZnSe thin film,’’ J. Semicond. 35(11), (2014): 113001.

[176] S. Antohe, L. Ion, M. Girtan and O. Toma, “Optical and morphological studies of thermally vacuum evaporated ZnSe thin films,’’ Rom. Rep. Phys. 65(3), (2013): 805-811.

[177] M. Özkan, N. Ekem, M. Z. Balbag and S. Pat, “ZnSe nanocrystalline thin films deposition on Si substrate by thermionic vacuum arc.,’’ in Proceedings of the Institution of Mechanical Engineers, Part L: J. Materials: Design and Applications, (Sage, 2012), pp.103-109.

[178] http://www.thermo.com.cn/Resources/201411/2412740468.pdf

[179] M.W. Cho, K. W. Koh, K. Morikawa, K. Arai, H. D. Jung, Z. Zhu, T. Yao and Y. Okada, “Surface treatment of ZnSe substrate and homoepitaxy of ZnSe,’’ J. Electron. Mater. 26(5), (1997): 423.

[180] D.T.F. Marple, “Refractive index of ZnSe, ZnTe, and CdTe,’’J. Appl. Phys. 35(3), (1964): 539-542.

[181] R. K. Watts, M. de Wit and W. C. Holton, “Nonoxide chalcogenide glass films for integrated optics,’’ Appl. Opt. 13(10), (1974): 2329-2332.

[182] J. Hu, V. Tarasov, A. Agarwal, and L. Kimerling, “Fabrication and testing of planar chalcogenide waveguide integrated microfluidic sensor,’’ Opt. Express 15(5) (2007): 2307-2314.

[183]http://www.ifsc.usp.br/~lavfis2/BancoApostilasImagens/ApLuminescencia/Infrared%20Spectr Spect1.pdf

[184] Mizaikoff, Boris. "Waveguide-enhanced mid-infrared chem/bio sensors." Chemical Society Reviews 42, no. 22 (2013): 8683-8699